University of California, Merced

Ph.D. Dissertation

Generalized Kubelka-Munk Theory - A Derivation And Extension From Radiative Transfer

Christopher Sandoval

A dissertation submitted
in partial fulfillment of the requirements for the degree

Doctor of Philosophy in Applied Mathematics

August, 2016

University of California, Merced
Graduate Division

This is to certify that I have examined a copy of a dissertation by

Christopher Sandoval

and found it satisfactory in all respects, and that any and all revisions required by the examining committee have been made.

Faculty Advisor:

Dr. Arnold Kim

Committee Members:

Dr. Arnold Kim

Dr. Boaz Ilan

Dr. Roummel Marcia

Applied Mathematics Graduate Studies Chair:

Dr. Harish Bhat

Date

ABSTRACT OF THE DISSERTATION

Generalized Kubelka-Munk Theory -
A Derivation And Extension From Radiative Transfer

by

Christopher Sandoval

University of California, Merced, 2016

Dr. Harish Bhat, Chair

Abstract

Kubelka-Munk (KM) theory is a broadly used simplification to the radiative transfer equation (RTE) that is solvable analytically for a restricted set of very simple problems. Despite this simplicity and popularity, KM theory has never had its theoretical basis formally established. In this work, we derive KM theory systematically from the radiative transfer equation (RTE) by application of the spectrally convergent double spherical harmonics method, of order one, and analysis of the resulting, transformed, system of equations in the positive- and negative-going fluxes. We call these the generalized Kubelka-Munk (gKM) equations, and they are able to account for general boundary sources and nonhomogeneous terms. Having established theoretical footing for KM theory, we extend gKM's four-flux method to higher dimensions, applying it to a Gaussian boundary source and demonstrating the method's range of validity. Finally, we examine the application of the gKM method to the vector radiative transport equation (vRTE), allowing for the modeling of sources with polarized light. These methods offer a low cost approximation to the solutions of the scalar and vector RTE's, which we validate through comparison with benchmark solutions of the transport equation.

Chapter 1

Introduction

The theory of radiative transfer describes light propagation in a multiple scattering medium [1, 2]. This theory takes into account absorption and scattering due to inhomogeneities in the propagating medium. Radiative transfer has important applications in atmospheric and ocean optics [3] and biomedical optics [4] among others. However, applying radiative transfer is challenging for practical problems because exact solutions of the radiative transport equation (RTE) are known only for simple problems. Even numerical solutions are challenging due to the large number of variables involved.

Kubelka-Munk theory [5, 6] is an approximation of the one dimensional radiative transfer equation. Rather than computing the full specific intensity, Kubelka-Munk (KM) theory describes the flow of power in "forward" and "backward" directions, defined with respect to the direction in which light is incident on the turbid medium. The Kubelka-Munk equations form a 2×2 system that is much easier to solve than the radiative transfer equation. However, a systematic derivation of the KM equations from the RTE was still needed to determine all coefficients and its range of validity.

It is well known that the Kubelka-Munk equations are limited to plane-parallel problems in one spatial dimension with isotropic or weakly anisotropic scattering and diffuse illumination. Additionally, it is well known that there exist more sophisticated approximations that are more accurate over a broader range of settings. Nonetheless, KM theory is widely used for a variety of applications. Presumably, KM theory is used for all of these applications because of its simplicity and its ability to model the qualitative behavior of light in complex media. Consequently, extending and generalizing Kubelka-Munk to other settings would be desirable to the application areas that already make extensive use of it.

We present in this thesis a systematic derivation of the KM equations from the RTE. By doing so, we are able to address the outstanding issues in KM theory and overcome its restrictions. A key step in this derivation is the application of the double spherical harmonics method [7, 8, 9, 10] of order one to solve the general boundary value problem for the one dimensional RTE. This theoretical framework also provides a means to generalize KM theory to a larger class of problems including general boundary conditions, nonhomogeneous terms, higher dimensions, and polarized light.

1.1 Kubelka-Munk theory

If we denote the flux in the positive- and negative-going directions as $F^{\pm}(z)$, respectively, through a plane parallel slab of scattering medium, then the Kubelka-Munk equations are

$$\frac{dF^+}{dz} + (K+S)F^+ = SF^-, \tag{1.1.1a}$$

$$-\frac{dF^-}{dz} + (K+S)F^- = SF^+. \tag{1.1.1b}$$

The constants, K and S are related to absorption and scattering, respectively.

This so-called two-flux theory is intuitive and much simpler than the RTE. However, despite several studies [11]-[20], the theoretical basis of KM theory was not entirely established [2], including the exact values of K and S or their direct connection to the absorption and scattering constants of radiative transfer theory. Other limitations plague KM theory as well. The first of which is that it is limited to plane parallel geometry with very little or no absorption ($\varpi_0 \sim 1$). Secondly, scattering within the slab must be isotropic or near isotropic, and third, there can be diffuse illumination only. In spite of these limitations, KM theory has found a home in a variety of applications.

In the context of the paints, inks/dyes, and papers industries, applications of KM theory include the prediction of the visual appearance of stratified layers of medium [21, 22, 23]. It has also been employed in the field of target recognition and remote sensing, where predicted properties of brands of paints have been used in friend-or-foe identification of vehicles [24]. Recently, KM theory has been used to measure the optical degradation in classic artwork [25].

KM theory has also been combined with the diffusion approximation to model light interaction with layered biological tissue systems [26]. Scattering is typically dominant in these regimes, which is a domain KM theory works well. Furthermore, light trapping by plant tissues [27, 28], which is crucial for photosynthesis, has also been modeled using KM theory.

It is clear that, despite the limitations of scope and a lack of solid theoretical foundation, Kubelka-Munk theory has enjoyed much success. This very breadth of application and simplicity in its ability to model a complex media is motivation for its generalization and extension.

1.2 The scalar radiative transfer equation

A more complete description of the scattering of light comes in the form of radiative transfer theory. Here, we prescribe the specific intensity, $I(\hat{\mathbf{\Omega}}, \mathbf{r})$, which gives the power flowing in direction $\hat{\mathbf{\Omega}} = (\theta, \varphi)$, a vector on the unit sphere, S^2, with θ and φ the zenith and azimuthal angles, respectively, shown in Diagram (i), at position $\mathbf{r}$. It is governed by the scalar radiative transfer equation

$$\hat{\mathbf{\Omega}} \cdot \nabla I + I = \frac{\varpi_0}{4\pi} \int_{S^2} \mathbb{P}(\hat{\mathbf{\Omega}} \cdot \hat{\mathbf{\Omega}}') I(\hat{\mathbf{\Omega}}', \mathbf{r}) \mathrm{d}\hat{\mathbf{\Omega}}' + Q(\hat{\mathbf{\Omega}}, \mathbf{r}). \tag{1.2.1}$$

Here, $\varpi_0 = \mu_s/(\mu_s + \mu_a)$ is the single scattering albedo with μ_a and μ_s denoting the absorption and scattering coefficients, respectively, $\mathbb{P}(\hat{\mathbf{\Omega}} \cdot \hat{\mathbf{\Omega}}')$ is the scattering phase function, and $Q(\hat{\mathbf{\Omega}}, \mathbf{r})$ is a source. In (1.2.1), the position vector is nondimensionalized according to

$\mathbf{r} = (\mu_s + \mu_a)\mathbf{r}'$.

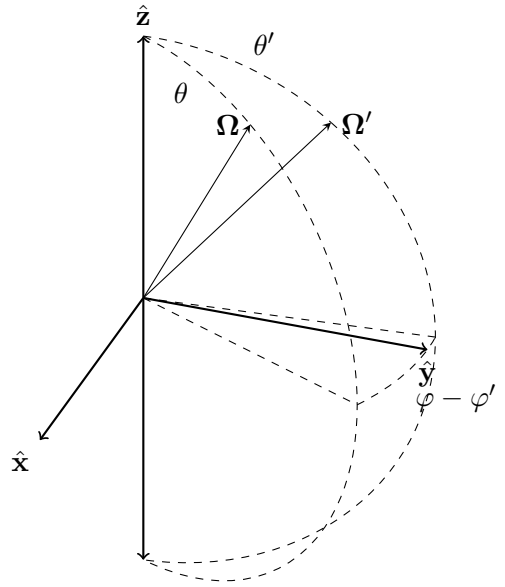

Diagram (i) (*Courtesy of Julia Clark*[1])

The scattering phase function, $\mathbb{P}$, gives the fraction of light scattered in direction $\hat{\mathbf{\Omega}}$ due to light incident in direction $\hat{\mathbf{\Omega}}'$. It is normalized according to

$$\frac{1}{4\pi}\int_{S^2} \mathbb{P}(\hat{\mathbf{\Omega}}\cdot\hat{\mathbf{\Omega}}')\, d\hat{\mathbf{\Omega}}' = 1. \tag{1.2.2}$$

Consequently, $I =$ constant is a solution of (1.2.1) when $\varpi_0 = 1$. In addition,

$$\frac{1}{4\pi}\int_{S^2} \mathbb{P}(\hat{\mathbf{\Omega}}\cdot\hat{\mathbf{\Omega}}')\hat{\mathbf{\Omega}}'\, d\hat{\mathbf{\Omega}}' = g\hat{\mathbf{\Omega}} \tag{1.2.3}$$

Here we define the domain as $D(\mathbf{r})$ with boundary $\partial D(\mathbf{r})$, and boundary conditions defined over the inward portion, i.e. $\hat{\mathbf{\Omega}}\cdot\hat{\mathbf{n}} < 0$, where $\hat{\mathbf{n}}$ is the outward unit normal of ∂D. Hence, for well posedness, we prescribe boundary conditions as $I = I_0(\mu,\varphi)$ on $\{(\hat{\mathbf{\Omega}},\mathbf{r}) \in \mathbb{S}^2 \times \partial D : \hat{\mathbf{\Omega}}\cdot\hat{\mathbf{n}}(\mathbf{r}) < 0\}$. In this work, we seek to solve (1.2.1) in the plane-parallel slab, $D = \{\mathbf{r} \in \mathbb{R}^3 | -\infty < x, y < \infty, 0 < z < z_1\}$.

Defining $\mu = \cos\theta$ allows us to rewrite (1.2.1) in terms of μ and the azimuthal angle, φ, as

$$\begin{aligned}\mu\partial_z I + &\sqrt{1-\mu^2}(\cos\varphi\partial_x I + \sin\varphi\partial_y I) + I \\ &= \frac{\varpi_0}{4\pi}\int_0^{2\pi}\int_{-1}^{1} \mathbb{P}(\mu,\mu',\varphi-\varphi')I(\mu',\varphi',\mathbf{r})\, d\mu' d\varphi' + Q(\mu,\varphi,\mathbf{r}),\end{aligned} \tag{1.2.4}$$

subject to boundary conditions $I(\mu,\varphi,x,y,0) = f^+(\mu,\varphi,x,y)$, on $0 < \mu \le 1$, and $I(\mu,\varphi,x,y,z_1) = f^-(\mu,\varphi,x,y)$, on $-1 \le \mu < 0$. Consider a one-dimensional slab, $0 \le z \le z_1$, with $-\infty < x, y < \infty$. Suppose that any sources of light do not depend on x and y. For

[1] Julia Clark is currently affiliated with the University of California, Merced, Ph.D. program

that case, we find that (1.2.4) reduces to

$$\mu\partial_z I + I = \frac{\varpi_0}{4\pi}\int_0^{2\pi}\int_{-1}^{1}\mathbb{P}(\mu,\mu',\varphi-\varphi')I(\mu',\varphi',z)\;d\mu' d\varphi' + Q(\mu,\varphi,z), \tag{1.2.5}$$

with boundary conditions $I(\mu,\varphi,0) = f^+(\mu,\varphi)$ on $(0,1]\times[0,2\pi]$ and $I(\mu,\varphi,z_1) = f^-(\mu,\varphi)$ on $[-1,0)\times[0,2\pi]$. When f^+, f^-, and Q are independent of φ, we may reduce (1.2.5) even further to obtain

$$\mu\partial_z I + I = \frac{\varpi_0}{2}\int_{-1}^{1}\mathbb{P}(\mu,\mu')I(\mu',z)\;d\mu' + Q(\mu,z), \tag{1.2.6}$$

subject to $I(\mu,0) = f^+(\mu)$ on $(0,1]$ and $I(\mu,z_1) = f^-(\mu)$ on $[-1,0)$. This can be viewed as one dimensional, axi-symmetric, scattering in a slab.

1.3 Singular structure of the radiance

It is clear that the RTE is discontinuous for $\mu = 0$. To explore this, we consider the following boundary value problem for the following one dimensional RTE in a slab $[0, z_1]$

$$\mu\frac{\partial I}{\partial z} + \mu_a I = G, \tag{1.3.1a}$$

$$I(\mu,0) = f_1(\mu) \quad \text{on } (0,1], \tag{1.3.1b}$$

$$I(\mu,z_1) = f_2(\mu) \quad \text{on } [-1,0). \tag{1.3.1c}$$

Here, G is a source term. In what follows, we show that I has a finite discontinuity at $\mu = 0$. Since the boundary value problem (1.3.1) is well posed, this discontinuity must result solely from discontinuities in the boundary conditions and/or any sources.

We will first set $\mu_a = 0$ and $G = 0$. For that case, (1.3.1a) becomes

$$\mu\frac{\partial I}{\partial z} = 0. \tag{1.3.2}$$

The solution is easily found as

$$I(\mu,z) = \begin{cases} f_1(\mu), & 0 < \mu \le 1 \\ f_2(\mu), & -1 \le \mu < 0 \end{cases}. \tag{1.3.3}$$

Here, unless $f_1(0^+) = f_2(0^-)$, I has a jump discontinuity. The jump is finite so long as $f_1(0^+)$ and $f_2(0^-)$ are bounded.

Next, let us take into account absorption, so $\mu_a \neq 0$ but $G = 0$. For that case, (1.3.1a) becomes

$$\mu\frac{\partial I}{\partial z} + \mu_a I = 0. \tag{1.3.4}$$

This is solved readily, yielding

$$I(\mu,z) = \begin{cases} f_1(\mu)e^{-\mu_a z/\mu}, & 0 < \mu \le 1 \\ f_2(\mu)e^{-\mu_a (z-z_1)/\mu}, & -1 \le \mu < 0 \end{cases} \tag{1.3.5}$$

Note that here $I(0^+,z) = I(0^-,z) = 0$ for $z \in (0,z_1)$; however, if we examine the solution

at the boundary, we find

$$I(\mu,0)=\begin{cases} f_1(\mu), & 0<\mu\le 1 \\ f_2(\mu)e^{\mu_a z_1/\mu}, & -1\le\mu<0 \end{cases} \tag{1.3.6a}$$

$$I(\mu,z_1)=\begin{cases} f_1(\mu)e^{-\mu_a z_1/\mu}, & 0<\mu\le 1 \\ f_2(\mu), & -1\le\mu<0 \end{cases}. \tag{1.3.6b}$$

Hence, unless $f_1(0^+)=0$ and $f_2(0^-)=0$, I is discontinuous at $z=0$ and $z=z_1$.

To solve (1.3.1), we represent I by its forward and backward components, i.e. $I^+ = I(+\mu,z)$ and $I^- = I(-\mu,z)$ for $\mu\in(0,1]$. Now, (1.3.1) can be written as

$$\mu\frac{\partial I^+}{\partial z}+\mu_a I^+ = G^+, \tag{1.3.7a}$$

$$-\mu\frac{\partial I^-}{\partial z}+\mu_a I^- = G^-, \tag{1.3.7b}$$

$$\text{subject to}\quad I^+(\mu,0)=f_1(\mu), \tag{1.3.7c}$$

$$I^-(\mu,z_1)=f_2(-\mu), \tag{1.3.7d}$$

where $G^+=G(\mu,z)$ and $G^-=G(-\mu,z)$. We may readily solve (1.3.7) to get

$$I^+(\mu,z)=f_1(\mu)e^{-\mu_a z/\mu}+\frac{1}{\mu}\int_0^z G^+(\mu,z')e^{-\mu_a(z-z')/\mu}\,dz', \tag{1.3.8a}$$

$$I^-(\mu,z)=f_2(-\mu)e^{\mu_a(z-z_1)/\mu}-\frac{1}{\mu}\int_z^{z_1} G^-(\mu,z')e^{\mu_a(z-z')/\mu}\,dz'. \tag{1.3.8b}$$

Assuming that G is an integrable and continuous function of μ, and a twice continuously differentiable function of z, we integrate by parts twice and obtain

$$\begin{aligned} I^+(\mu,z) &= f_1(\mu)e^{-\mu_a z/\mu}+\frac{1}{\mu_a}\left[G^+(\mu,z)-G^+(\mu,0)e^{-\mu_a z/\mu}\right] \\ &\quad -\frac{\mu}{\mu_a^2}\left[G_z^+(\mu,z)-G_z^+(\mu,0)e^{-\mu_a z/\mu}\right]+\frac{\mu}{\mu_a^2}\int_0^z G_{zz}^+(\mu,z')e^{-\mu_a(z-z')/\mu}\,dz' \end{aligned} \tag{1.3.9a}$$

$$\begin{aligned} I^-(\mu,z) &= f_2(-\mu)e^{\mu_a(z-z_1)/\mu}+\frac{1}{\mu_a}\left[G^-(\mu,z_1)e^{\mu_a(z-z_1)/\mu}-G^-(\mu,z)\right] \\ &\quad +\frac{\mu}{\mu_a^2}\left[G_z^-(\mu,z_1)e^{\mu_a(z-z_1)/\mu}-G_z^-(\mu,z)\right]-\frac{\mu}{\mu_a^2}\int_z^{z_1} G_{zz}^-(\mu,z')e^{\mu_a(z-z')/\mu}\,dz' \end{aligned} \tag{1.3.9b}$$

Now consider the quantity

$$\begin{aligned}\Delta I(\mu,z) &= I^+(\mu,z) - I^-(\mu,z)\\ &= f_1(\mu)e^{-\mu_a z/\mu} - f_2(-\mu)e^{\mu_a(z-z_1)/\mu}\\ &\quad + \frac{1}{\mu_a}\left[G^+(\mu,z) - G^+(\mu,0)e^{-\mu_a z/\mu} + G^-(\mu,z) - G^-(\mu,z_1)e^{\mu_a(z-z_1)/\mu}\right]\\ &\quad - \frac{\mu}{\mu_a^2}\left[G_z^+(\mu,z) - G_z^+(\mu,0)e^{-\mu_a z/\mu} + G_z^-(\mu,z) - G_z^-(\mu,z_1)e^{\mu_a(z-z_1)/\mu}\right]\\ &\quad + \frac{\mu}{\mu_a^2}\left[\int_0^z G_{zz}^+(\mu,z')e^{-\mu_a(z-z')/\mu}\,dz' + \int_z^{z_1} G_{zz}^-(\mu,z')e^{\mu_a(z-z')/\mu}\,dz'\right].\end{aligned} \tag{1.3.10}$$

Letting $\mu \to 0^+$, we can now see that

$$\lim_{\mu\to 0^+}\Delta I(\mu,0) = f_1(0^+) + \frac{1}{\mu_a}G^-(0^+,0), \tag{1.3.11a}$$

$$\lim_{\mu\to 0^+}\Delta I(\mu,z_1) = -f_2(0^-) + \frac{1}{\mu_a}G^+(0^+,z_1), \tag{1.3.11b}$$

and

$$\lim_{\mu\to 0^+}\Delta I(\mu,z) = \frac{1}{\mu_a}\left[G^+(0^+,z) + G^-(0^+,z)\right], \quad z\in(0,z_1). \tag{1.3.12}$$

Hence, at least at the boundaries, we find that as $\mu \to 0^+$ that $I(\mu,z)$ is finitely discontinuous. This singularity carries upwards to the three dimensional and vector cases as well. In these cases, I will have finite discontinuities anywhere tangent to the boundary of the domain.

Within the scope of the one dimensional problem, we consider the particular form of the source term,

$$G(\mu,z) = -\mu_s I(\mu,z) + \mu_s\int_{-1}^{1}\mathbb{P}(\mu,\mu')I(\mu',z)\,d\mu' \tag{1.3.13}$$

Hence, the forward and backward version can be shown to be

$$G^+(\mu,z) = -\mu_s I^+(\mu,z) + \mu_s\int_0^1\mathbb{P}(\mu,\mu')I^+(\mu',z)\,d\mu' + \mu_s\int_0^1\mathbb{P}(\mu,-\mu')I^-(\mu',z)\,d\mu', \tag{1.3.14a}$$

$$G^-(\mu,z) = -\mu_s I^-(\mu,z) + \mu_s\int_0^1\mathbb{P}(-\mu,\mu')I^+(\mu',z)\,d\mu' + \mu_s\int_0^1\mathbb{P}(-\mu,-\mu')I^-(\mu',z)\,d\mu'. \tag{1.3.14b}$$

From the above work, we see clearly that any discontinuities stem only from boundary and internal sources. These decay exponentially with the depth of the slab so long as absorption is present.

1.4 Double spherical harmonics

We have demonstrated that (1.2.4) is discontinuous for $\mu = 0$ on the boundaries and that this discontinuity decays exponentially away from these boundaries due to scattering and absorption. In light of this discontinuity, we use the double spherical harmonics (DP_n) method to solve boundary value problem (1.2.4). The DP_n method explicitly takes into account this discontinuity by defining I piecewise over the half-ranges, $1 \leq \mu < 0$ and $0 < \mu \leq 1$.

The DP_n method is a well established approximation method [8]. In contrast to the spherical harmonics method, P_n, the DP_n method involves expanding the angular dependence of the specific intensity in half ranges. Mengüç and Iyer [29] have compared P_n and DP_n results and have shown that DP_n to be a better approximation. For example, they found that the DP_1 approximation to be nearly as accurate as the P_9 approximation in most cases. We describe the DP_n method in detail below.

1.4.1 Basis functions

Consider the set of spherical harmonics $\{Y_{nm}\}$, where Y_{nm} is defined as

$$Y_{nm}(\mu,\varphi) = \left[\frac{2n+1}{4\pi}\frac{(n-|m|)!}{(n+|m|)!}\right]^{1/2}(-1)^{(m+|m|)/2}P_n^{|m|}(\mu)e^{im\varphi}, \tag{1.4.1}$$

and where $\{P_n^{|m|}\}$ denotes the set of associated Legendre functions. Let $\tilde{Y}_{nm}(\mu,\varphi) = \sqrt{2}Y_{nm}(2\mu-1,\varphi)$ for the half-range, $0 < \mu \leq 1$. These functions obey the orthogonality relation

$$\int_0^{2\pi}\int_0^1 \tilde{Y}_{nm}(\mu,\varphi)\tilde{Y}^*_{n'm'}(\mu,\varphi)\; d\mu d\varphi = \delta_{n,n'}\delta_{m,m'}, \tag{1.4.2}$$

where δ is the Kronecker delta and the star denotes the complex conjugate. It can also be shown they satisfy the following recurrence relation:

$$\sqrt{2n+1}\tilde{Y}_{nm}(\mu,\varphi) = \sqrt{\frac{n^2-m^2}{2n-1}}\tilde{Y}_{n-1,m}(\mu,\varphi) + \sqrt{\frac{(n+1)^2-m^2}{2n+3}}\tilde{Y}_{n+1,m}(\mu,\varphi). \tag{1.4.3}$$

1.4.2 The DP_n method

We now denote $I^{\pm}(\mu,\varphi,\mathbf{r}) = I(\pm\mu,\varphi,\mathbf{r})$ and $Q^{\pm}(\mu,\varphi,\mathbf{r}) = Q(\pm\mu,\varphi,\mathbf{r})$, for $0 < \mu \leq 1$. Now we approximate $I^{\pm}$ using the truncated expansion in $\tilde{Y}_{nm}(\mu,\varphi)$,

$$I^{\pm}(\mu,\varphi,\mathbf{r}) \approx I_N^{\pm}(\mu,\varphi,\mathbf{r}) = \sum_{n=0}^{N}\sum_{m=n}^{n} c_{nm}^{\pm}(\mathbf{r})\tilde{Y}_{nm}(\mu,\varphi), \tag{1.4.4}$$

where $c_{nm}^{\pm}$ are coefficients to be determined.

For simplicity, we begin by considering the one dimensional, axi-symmetric, scattering in a slab, (1.2.6). In this case, (1.4.4) reduces to

$$I^{\pm}(\mu,z) \approx I_N^{\pm}(\mu,z) = \sum_{n=0}^{N} c_n^{\pm}(z)\tilde{P}_n(\mu), \tag{1.4.5}$$

with $\tilde{P}_n(\mu) = \sqrt{2n+1}P_n(2\mu-1)$, over $0 < \mu \leq 1$, and $\{P_n(\mu)\}$ the set of Legendre polynomials. Substituting this into (1.2.6), we get the coupled pair of equations

$$\mu\frac{\partial I^+}{\partial z} + I^+ = \frac{\varpi_0}{2}\int_0^1 \left[\mathbb{P}(\mu,\mu')I^+(\mu',z) + \mathbb{P}(\mu,-\mu')I^-(\mu',z)\right]\, d\mu' + Q^+(\mu,z), \quad (1.4.6a)$$

$$-\mu\frac{\partial I^-}{\partial z} + I^- = \frac{\varpi_0}{2}\int_0^1 \left[\mathbb{P}(\mu,-\mu')I^+(\mu',z) + \mathbb{P}(\mu,\mu')I^-(\mu',z)\right]\, d\mu' + Q^-(\mu,z), \quad (1.4.6b)$$

$$I^+(\mu,0) = f^+(\mu), \quad (1.4.6c)$$

$$I^-(\mu,z_1) = f^-(\mu). \quad (1.4.6d)$$

Here, due to the spherically symmetric scattering, we have $\mathbb{P}(-\mu,-\mu') = \mathbb{P}(\mu,\mu')$ and $\mathbb{P}(\mu,-\mu') = \mathbb{P}(-\mu,\mu')$. Substituting (1.4.5) into (1.4.6) and making us of orthogonality yields the system of equations in the vectors of coefficients, $\mathbf{c}^\pm = [c_0^\pm, c_1^\pm, \ldots, c_N^\pm]^T$,

$$\frac{d}{dz}\begin{bmatrix} A & 0 \\ 0 & -A \end{bmatrix}\begin{bmatrix}\mathbf{c}^+ \\ \mathbf{c}^-\end{bmatrix} = \begin{bmatrix} \varpi_0 H^{(1)} - \mathbb{I} & \varpi_0 H^{(2)} \\ \varpi_0 H^{(2)} & \varpi_0 H^{(1)} - \mathbb{I}\end{bmatrix}\begin{bmatrix}\mathbf{c}^+ \\ \mathbf{c}^-\end{bmatrix} + \begin{bmatrix}\mathbf{q}^+ \\ \mathbf{q}^-\end{bmatrix}, \quad (1.4.7)$$

with $\mathbb{I}$ denoting the identity matrix. The entries of A are given by

$$\begin{aligned} A_{m+1,n+1} &= \int_0^1 \tilde{P}_m(\mu)\tilde{P}_n(\mu)\mu\, d\mu \\ &= \frac{1}{2}\left[\frac{m}{\sqrt{(2m-1)(2m+1)}}\delta_{m,n-1} + \delta_{mn} + \frac{m+1}{\sqrt{(2m+1)(2m+3)}}\delta_{m,n+1}\right], \end{aligned} \quad (1.4.8)$$

for $m = 0, 1, \ldots, N$ and $n = 0, 1, \ldots, N$. Note that the matrix A is symmetric and tridiagonal. The entries of $H^{(1)}$ and $H^{(2)}$ are given by

$$H^{(1)}_{m+1,n+1} = \frac{1}{2}\int_0^1 \tilde{P}_m(\mu)\int_0^1 \mathbb{P}(\mu,\mu')\tilde{P}_n(\mu')\, d\mu d\mu' \quad (1.4.9a)$$

$$\text{and} \quad H^{(2)}_{m+1,n+1} = \frac{1}{2}\int_0^1 \tilde{P}_m(\mu)\int_0^1 \mathbb{P}(\mu,-\mu')\tilde{P}_n(\mu')\, d\mu d\mu', \quad (1.4.9b)$$

for $m = 0, 1, \ldots, N$ and $n = 0, 1, \ldots, N$. These matrices are also symmetric. We have also denoted the components of the source term vectors, $\mathbf{q}^\pm$, are $\mathbf{q}^\pm = [q_1^\pm, q_2^\pm, \ldots, q_{N+1}^\pm]^T$, with

$$q^\pm_{n+1}(z) = \int_0^1 Q^\pm(\mu,z)\tilde{P}_n(\mu)\, d\mu, \quad (1.4.10)$$

for $n = 0, 1, \ldots, N$.

Boundary conditions (1.4.6c) and (1.4.6d) are prescribed over the half-range, $0 < \mu \leq 1$. Consequently, for the DP_n method, we prescribe the boundary conditions

$$\mathbf{c}^+(0) = \mathbf{f}^+, \quad (1.4.11a)$$

$$\mathbf{c}^-(z_1) = \mathbf{f}^-, \quad (1.4.11b)$$

where $\mathbf{f}^{\pm}$ are the vectors whose components are

$$f^{+}_{n+1} = \int_0^1 f^{+}(\mu)\tilde{P}_n(\mu)\, d\mu, \tag{1.4.12a}$$

$$f^{-}_{n+1} = \int_0^1 f^{-}(-\mu)\tilde{P}_n(\mu)\, d\mu, \tag{1.4.12b}$$

for $n = 0, 1, \ldots, N$. This $2(N+1)$ system, which we call the DP_n system is suitable for numerical solution as is done in the later sections.

Suppose we have performed this truncation. Consider the following $2(N+1)\times 2(N+1)$ generalized eigenvalue problem:

$$\lambda \begin{bmatrix} A & 0 \\ 0 & -A \end{bmatrix} \begin{bmatrix} \mathbf{u} \\ \mathbf{v} \end{bmatrix} = \begin{bmatrix} \varpi_0 H^{(1)} - \mathbb{I} & \varpi_0 H^{(2)} \\ \varpi_0 H^{(2)} & \varpi_0 H^{(1)} - \mathbb{I} \end{bmatrix} \begin{bmatrix} \mathbf{u} \\ \mathbf{v} \end{bmatrix}, \tag{1.4.13}$$

resulting from substituting $\mathbf{c}^{+} = e^{\lambda z}\mathbf{u}$ and $\mathbf{c}^{-} = e^{\lambda z}\mathbf{v}$ into (1.4.7) with $\mathbf{q}^{\pm} = \mathbf{0}$. We will now prove a few facts about these eigenvalues and eigenvectors.

First we will show that (1.4.13) has real eigenvalues. Suppose the pair $(\lambda, \mathbf{x})$ satisfies (1.4.13), i.e.

$$\lambda \begin{bmatrix} A & \mathbf{0} \\ \mathbf{0} & -A \end{bmatrix} \mathbf{x} = \mathcal{L}\mathbf{x}, \tag{1.4.14}$$

with $\mathcal{L}$ the matrix operator on the right side of (1.4.13), which we know is symmetric and real. Now consider

$$\begin{aligned} \lambda \mathbf{x}^{\dagger} \begin{bmatrix} A & \mathbf{0} \\ \mathbf{0} & -A \end{bmatrix} \mathbf{x} \quad &= \mathbf{x}^{\dagger}(\mathcal{L}\mathbf{x} \\ &= \left(\mathbf{x}^{\dagger}\mathcal{L}^{\dagger}\mathbf{x}\right)^{\dagger} \\ &= \left(\mathbf{x}^{\dagger}\mathcal{L}\mathbf{x}\right)^{\dagger} \\ &= \left(\mathbf{x}^{\dagger}\lambda \begin{bmatrix} A & \mathbf{0} \\ \mathbf{0} & -A \end{bmatrix} \mathbf{x}\right)^{\dagger} \\ &= \lambda^{*}\mathbf{x}^{\dagger} \begin{bmatrix} A & \mathbf{0} \\ \mathbf{0} & -A \end{bmatrix} \mathbf{x}. \end{aligned} \tag{1.4.15}$$

Here, we have used $\dagger$ to denote the conjugate transpose. Hence, $\lambda = \lambda^{*}$, and therefore, λ is real valued.

Furthermore, we will now show that if λ is an eigenvalue of (1.4.13) with eigenvector $[\mathbf{u}, \mathbf{v}]^T$, then $-\lambda$ is also an eigenvalue with corresponding eigenvector $[\mathbf{v}, \mathbf{u}]^T$. Substituting $-\lambda$ and $[\mathbf{v}, \mathbf{u}]^T$ into (1.4.13), we get

$$-\lambda \begin{bmatrix} A & 0 \\ 0 & -A \end{bmatrix} \begin{bmatrix} \mathbf{v} \\ \mathbf{u} \end{bmatrix} = \begin{bmatrix} \varpi_0 H^{(1)} - \mathbb{I} & \varpi_0 H^{(2)} \\ \varpi_0 H^{(2)} & \varpi_0 H^{(1)} - \mathbb{I} \end{bmatrix} \begin{bmatrix} \mathbf{v} \\ \mathbf{u} \end{bmatrix}. \tag{1.4.16}$$

Note that this is easily rewritable as

$$-\lambda \begin{bmatrix} -A & 0 \\ 0 & A \end{bmatrix} \begin{bmatrix} \mathbf{u} \\ \mathbf{v} \end{bmatrix} = \begin{bmatrix} \varpi_0 H^{(1)} - \mathbb{I} & \varpi_0 H^{(2)} \\ \varpi_0 H^{(2)} & \varpi_0 H^{(1)} - \mathbb{I} \end{bmatrix} \begin{bmatrix} \mathbf{u} \\ \mathbf{v} \end{bmatrix}, \tag{1.4.17}$$

which once the negative is multiplied into the left hand matrix we get identically (1.4.13). In light of this symmetry, we index and order the eigenvalues according to

$$\lambda_{-(N+1)} \leq \cdots \leq \lambda_{-1} < 0 < \lambda_1 \leq \cdots \leq \lambda_{N+1}, \tag{1.4.18}$$

where $\lambda_{-j} = -\lambda_j$. We denote the eigenvectors corresponding to λ_j as $[\mathbf{u}_j, \mathbf{v}_j]^T$ for $j = 1, 2, \cdots$. When $\varpi_0 = 1$, $\lambda = 0$ is an eigenvalue, but otherwise $\lambda \neq 0$ as indicated in (1.4.18).

1.4.3 Convergence of c_n

To estimate the rate of convergence for these Fourier series, we examine the one dimensional expansion coefficients:

$$c_n(z) = \int_{-1}^{1} f(\mu, z) P_n(\mu)\, d\mu, \tag{1.4.19}$$

with $f(\mu, z)$ being an N-times differentiable function in μ, $N \geq 1$. Using the fact that

$$(2n+1)P_n(\mu) = \frac{d}{d\mu}\Big(P_{n+1}(\mu) - P_{n-1}(\mu)\Big), \tag{1.4.20}$$

and integrating (1.4.19) by parts, we find

$$\begin{aligned} c_n(z) &= \frac{1}{2n+1}\left[f(\mu, z)\Big(P_{n+1}(\mu) - P_{n-1}(\mu)\Big)\Big|_{-1}^{1} - \int_{-1}^{1} f_\mu(\mu, z)\Big(P_{n+1}(\mu) - P_{n-1}(\mu)\Big)\, d\mu \right] \\ &= -\frac{1}{2n+1}\int_{-1}^{1} f_\mu(\mu, z)\Big(P_{n+1}(\mu) - P_{n-1}(\mu)\Big)\, d\mu. \end{aligned} \tag{1.4.21}$$

Here we used the fact that $P_n(1) = 1$ and $P_n(0) = (-1)^n$. If we repeatedly integrate by parts, applying the following relations,

$$\sum_{i=0}^{k} \binom{k}{i} (-1)^i P_{n+k-2i}(-1) = \sum_{i=0} (-1)^i (-1)^{n+k-2i} = 0 \tag{1.4.22a}$$

$$\text{and } \sum_{i=0}^{k} \binom{k}{i} (-1)^i P_{n+k-2i}(1) = \sum_{i=0} \binom{k}{i} (-1)^i = 0, \tag{1.4.22b}$$

we find that

$$c_n(z) = \frac{(-1)^n}{(2n+1)^n} \int_{-1}^{1} \frac{\partial^n f(\mu, z)}{\partial \mu^n} \sum_{i=0}^{n} \binom{n}{i} (-1)^i P_{2(n-i)}(\mu)\, d\mu. \tag{1.4.23}$$

Since $|P_n(\mu)| \leq 1$, we see that

$$\begin{aligned} c_n(z) &= \frac{(-1)^n}{(2n+1)^n} \int_{-1}^{1} \frac{\partial^n f(mu, z)}{\partial \mu^n} \sum_{i=0}^{n} \binom{n}{i} (-1)^i P_{2(n-i)}(\mu)\ d\mu \\ &\leq \frac{(-1)^n}{(2n+1)^n} \int_{-1}^{1} \frac{\partial^n f(\mu, z)}{\partial \mu^n} \sum_{i=0}^{n} \binom{n}{i}\ d\mu \\ &= \frac{(-1)^n}{(2n+1)^n} \int_{-1}^{1} \frac{\partial^n f(\mu, z)}{\partial \mu^n} (2^n) \\ &= (-1)^n \frac{2^{n+1}}{(2n+1)^n} \bar{f}^{(n)}(\mu, z). \end{aligned} \tag{1.4.24}$$

Since we presume that f is finite, we may bound its average, $\bar{f}$, by some constant. Hence, as $n \to \infty$, the coefficients, $c_n(z)$, decay to zero at a rate on the order of $1/n^n$.

1.4.4 Equivalence with discrete ordinate method

Here we justify DP_n being equivalent to the discrete ordinate method, another well known method, employing a double-Gauss quadrature. We begin by examining (1.2.6) with $Q = 0$, which we evaluate over the quadrature points $\mu_j = 2\mu'_j - 1$, where μ'_j is the Gauss-Legendre quadrature points over $[-1, 1]$, and weights $w_j = 0.5w'_j$, yielding

$$\mu_j \partial_z I_j(z) = -I_j(z) + \sum_{k=0}^{K} \mathbb{P}(\mu_j, \mu_k) I_k(z) w_k. \tag{1.4.25}$$

Here, we have written $I_j(z) = I(\mu_j, z)$. Expanding $I_j(z) = \sum_{n=0}^{N} c_n(z) \tilde{P}_n(\mu_j)$, and splitting (1.4.25) into the positive and negative directions, gives us

$$\begin{aligned} \sum_{n=0}^{N} \Bigg\{ \mu_j \frac{d}{dz} c_n^+(z) \tilde{P}_n(\mu_j) &= -\tilde{P}_n(\mu_j) c_n^+(z) \\ &+ \sum_{k=0}^{K} \left[\mathbb{P}(\mu_j, \mu_k) \tilde{P}_n(\mu_k) w_k c_n^+(z) + \mathbb{P}(\mu_j, -\mu_k) \tilde{P}_n(\mu_k) w_k c_n^-(z) \right] \Bigg\}, \end{aligned} \tag{1.4.26a}$$

$$\begin{aligned} \sum_{n=0}^{N} \Bigg\{ -\mu_j \frac{d}{dz} c_n^-(z) \tilde{P}_n(\mu_j) &= -\tilde{P}_n(\mu_j) c_n^-(z) \\ &+ \sum_{k=0}^{K} \left[\mathbb{P}(-\mu_j, \mu_k) \tilde{P}_n(\mu_k) w_k c_n^+(z) + \mathbb{P}(-\mu_j, -\mu_k) \tilde{P}_n(\mu_k) w_k c_n^-(z) \right] \Bigg\}. \end{aligned} \tag{1.4.26b}$$

The term on the left hand side of both (1.4.26a) and (1.4.26b) can be modified by using the recurrence relation

$$\mu \tilde{P}_n(\mu) = \frac{1}{\sqrt{2n+1}} \left[(n+1) \tilde{P}_{n+1}(\mu) + (2n+1) \tilde{P}_n(\mu) + n \tilde{P}_{n-1}(\mu) \right] \tag{1.4.27}$$

to get

$$\sum_{n=0}^{N}\Bigg\{\left[\frac{n+1}{\sqrt{2n+1}}\tilde{P}_{n+1}(\mu_j)+\sqrt{2n+1}\tilde{P}_n(\mu_j)+n\tilde{P}_{n-1}(\mu_j)\right]\frac{d}{dz}c_n^+(z)=-\tilde{P}_n(\mu_j)c_n^+(z)$$
$$+\sum_{k=0}^{K}\left[\mathbb{P}(\mu_j,\mu_k)\tilde{P}_n(\mu_k)w_kc_n^+(z)+\mathbb{P}(\mu_j,-\mu_k)\tilde{P}_n(\mu_k)w_kc_n^-(z)\right]\Bigg\}, \quad (1.4.28a)$$

$$\sum_{n=0}^{N}\Bigg\{-\left[\frac{n+1}{\sqrt{2n+1}}\tilde{P}_{n+1}(\mu_j)+\sqrt{2n+1}\tilde{P}_n(\mu_j)+n\tilde{P}_{n-1}(\mu_j)\right]\frac{d}{dz}c_n^-(z)=-\tilde{P}_n(\mu_j)c_n^-(z)$$
$$+\sum_{k=0}^{K}\left[\mathbb{P}(-\mu_j,\mu_k)\tilde{P}_n(\mu_k)w_kc_n^+(z)+\mathbb{P}(-\mu_j,-\mu_k)\tilde{P}_n(\mu_k)w_kc_n^-(z)\right]\Bigg\}. \quad (1.4.28b)$$

Shifting indices and using the fact that for spherical scattering, $\mathbb{P}(\mu,\mu')=\mathbb{P}(-\mu,-\mu')$ and $\mathbb{P}(\mu,-\mu')=\mathbb{P}(-\mu,\mu')$, we may write (1.4.28a) and (1.4.28b) as

$$\sum_{n=0}^{N}\frac{n}{\sqrt{2n-1}}\tilde{P}_n(\mu_j)\frac{d}{dz}c_{n-1}^+(z)+\sum_{n=0}^{N}\sqrt{2n+1}\tilde{P}_n(\mu_j)\frac{d}{dz}c_n^+(z)+\sum_{n=0}^{N}\frac{n+1}{\sqrt{2n+3}}\tilde{P}_n(\mu_j)\frac{d}{dz}c_{n+1}^+(z)$$
$$=\sum_{n=0}^{N}\left[-\tilde{P}_n(\mu_j)c_n^+(z)+H_n^{(1)}(\mu_j)c_n^+(z)+H_n^{(2)}(\mu_j)c_n^-(z)\right], \quad (1.4.29a)$$

$$-\sum_{n=0}^{N}\frac{n}{\sqrt{2n-1}}\tilde{P}_n(\mu_j)\frac{d}{dz}c_{n-1}^-(z)-\sum_{n=0}^{N}\sqrt{2n+1}\tilde{P}_n(\mu_j)\frac{d}{dz}c_n^-(z)-\sum_{n=0}^{N}\frac{n+1}{\sqrt{2n+3}}\tilde{P}_n(\mu_j)\frac{d}{dz}c_{n+1}^-(z)$$
$$=\sum_{n=0}^{N}\left[-\tilde{P}_n(\mu_j)c_n^-(z)+H_n^{(2)}(\mu_j)c_n^+(z)+H_n^{(1)}(\mu_j)c_n^-(z)\right]. \quad (1.4.29b)$$

Here we have written

$$H_n^{(1)}(\mu_j)=\sum_{m=0}^{M}\mathbb{P}(\mu_j,\mu_m)\tilde{P}_m(\mu_m)w_m, \quad (1.4.30a)$$

$$\text{and}\quad H_n^{(2)}(\mu_j)=\sum_{m=0}^{M}\mathbb{P}(-\mu_j,\mu_m)\tilde{P}_m(\mu_m)w_m, \quad (1.4.30b)$$

and we use the fact that $c_{-1}(z)\equiv 0$, $c_{N+1}(z)\equiv 0$, and we may choose μ_j in such a fashion

as to force $\tilde{P}_{N+1}(\mu_j) \equiv 0$. Since $\tilde{P}_0(\mu_j) = 1$, we rewrite (1.4.29a) and (1.4.29b) as

$$\sum_{n=0}^{N} \tilde{P}_n(\mu_j) \Bigg\{ \frac{n}{\sqrt{2n-1}} \frac{d}{dz} c_{n-1}^{+}(z) + \sqrt{2n+1} \frac{d}{dz} c_n^{+}(z) + \frac{n+1}{\sqrt{2n+3}} \frac{d}{dz} c_{n+1}^{+}(z) + c_n^{+}(z) - \delta_{n,0} \sum_{n'=0}^{N} \left[H_{n'}^{(1)}(\mu_j) c_{n'}^{+}(z) + H_{n'}^{(2)}(\mu_j) c_{n'}^{-}(z) \right] \Bigg\} = 0, \quad (1.4.31a)$$

$$\sum_{n=0}^{N} \tilde{P}_n(\mu_j) \Bigg\{ - \frac{n}{\sqrt{2n-1}} \frac{d}{dz} c_{n-1}^{-}(z) - \sqrt{2n+1} \frac{d}{dz} c_n^{-}(z) - \frac{n+1}{\sqrt{2n+3}} \frac{d}{dz} c_{n+1}^{-}(z) + c_n^{-}(z) - \delta_{n,0} \sum_{n'=0}^{N} \left[H_{n'}^{(2)}(\mu_j) c_{n'}^{+}(z) + H_{n'}^{(1)}(\mu_j) c_{n'}^{-}(z) \right] \Bigg\} = 0, \quad (1.4.31b)$$

where δ is the Kronecker delta. Since $\tilde{P}_n(\mu_j) \neq 0$ for all μ_j, we conclude the expression in the brackets is equal to zero. However, we note that this expression is simply the DP_n equations with the integral expressions being approximated by the sums in $H_n^{(1)}$ and $H_n^{(2)}$. Since the numerical integration is exact for polynomials of up to degree $2(N+1)$, we find this is then exactly the DP_n equations evaluated at the quadrature points, μ_j.

Chapter 2

Generalized Kubelka-Munk theory

In this chapter, we present the formal derivation of the Kubelka-Munk equations systematically from the radiative transfer equation. We do this by introducing what we call the generalized Kubelka-Munk equations, a modified DP_1 method, expanding the KM system from a two-flux system to a four-flux system. We justify numerically the advantages of such a small increase in complexity at the end of the chapter, comparing the KM system, the gKM system, and actual solutions of the RTE computed via the discrete ordinate method.

2.1 The generalized Kubelka-Munk system

The key step in deriving KM theory from the RTE lies in analyzing the DP_1 system. To see why this relationship is important, recall that KM theory provides the governing equations for the positive- and negative-going fluxes defined in terms of the specific intensity as

$$F^{\pm}(z) = \int_0^1 \mu I^{\pm}(\mu, z)\, d\mu. \tag{2.1.1}$$

Inserting the expansion for I from (1.4.5), we find that

$$F^{\pm}(z) = \frac{1}{2}\left(c_0^{\pm}(z) + \frac{1}{\sqrt{3}} c_1^{\pm}(z)\right). \tag{2.1.2}$$

In other words, the power flowing in the positive- and negative-going directions can be expressed simply in terms of the first two expansion coefficients in (1.4.5). The smallest DP_n system involving just $c_0^{\pm}$ and $c_1^{\pm}$ is the DP_1 system.

Let us introduce the auxiliary quantities $G^{\pm}$ defined as

$$G^{\pm} = \frac{1}{2}\left(\frac{1}{\sqrt{3}} c_0^{\pm} + c_1^{\pm}\right). \tag{2.1.3}$$

Then, we have the following linear transformations

$$\begin{bmatrix} F^{\pm} \\ G^{\pm} \end{bmatrix} = \begin{bmatrix} \frac{1}{2} & \frac{1}{2\sqrt{3}} \\ \frac{1}{2\sqrt{3}} & \frac{1}{2} \end{bmatrix} \begin{bmatrix} c_0^{\pm} \\ c_1^{\pm} \end{bmatrix}. \tag{2.1.4}$$

The 2×2 matrix in (2.1.4) is the matrix A whose entries are defined in (1.4.8) for $m, n = 0, 1$. Let $\mathbf{y}^{\pm} = [F^{\pm}\ G^{\pm}]^T$. Using the inverse transformation $\mathbf{c}^{\pm} = A^{-1}\mathbf{y}^{\pm}$, we

transform the DP_1 system given in (1.4.7) to

$$\frac{\mathrm{d}}{\mathrm{d}z}\begin{bmatrix}\mathbb{I} & 0\\ 0 & -\mathbb{I}\end{bmatrix}\begin{bmatrix}\mathbf{y}^+\\ \mathbf{y}^-\end{bmatrix} = \begin{bmatrix}S_1 & S_2\\ S_2 & S_1\end{bmatrix}\begin{bmatrix}\mathbf{y}^+\\ \mathbf{y}^-\end{bmatrix} + \begin{bmatrix}\mathbf{q}^+\\ \mathbf{q}^-\end{bmatrix}, \tag{2.1.5}$$

with $S_1 = \varpi_0 H^{(1)} A^{-1} - A^{-1}$ and $S_2 = \varpi_0 H^{(2)} A^{-1}$. By left-multiplying boundary conditions (1.4.12) by A, we obtain the boundary conditions

$$\mathbf{y}^+(0) = A\mathbf{f}^+, \tag{2.1.6a}$$
$$\mathbf{y}^-(z) = A\mathbf{f}^-. \tag{2.1.6b}$$

We call (2.1.5), the generalized Kubelka-Munk (gKM) equations because it is a system governing the fluxes $F^\pm$ and the auxiliary quantities $G^\pm$. Boundary conditions for the gKM equations are given in (2.1.6). The gKM equations are valid when the truncation associated with the DP_1 system is valid. Since the DP_n approximation is based on (1.4.5), which represent $I^\pm$ as an expansion in orthogonal polynomials, the DP_1 system gives the optimal, piecewise linear representation of the specific intensity in the least-squares sense.

Consider the 4×4 eigenvalue problem

$$\tilde{\lambda}\begin{bmatrix}\mathbb{I} & 0\\ 0 & -\mathbb{I}\end{bmatrix}\begin{bmatrix}\tilde{\mathbf{u}}\\ \tilde{\mathbf{v}}\end{bmatrix} = \begin{bmatrix}S_1 & S_2\\ S_2 & S_1\end{bmatrix}\begin{bmatrix}\tilde{\mathbf{u}}\\ \tilde{\mathbf{v}}\end{bmatrix}, \tag{2.1.7}$$

associated to homogeneous gKM equations. Just as with the eigenvalue problem given in (1.4.13), if $\tilde{\lambda}$ is an eigenvalue with eigenvector $[\tilde{\mathbf{u}}, \tilde{\mathbf{v}}]^T$, then $-\tilde{\lambda}$ is an eigenvalue with eigenvector $[\tilde{\mathbf{v}}, \tilde{\mathbf{u}}]^T$. Thus, we index and order the eigenvalues according to

$$\tilde{\lambda}_{-2} \leq \tilde{\lambda}_{-1} < 0 < \tilde{\lambda}_1 \leq \tilde{\lambda}_2, \tag{2.1.8}$$

with $\tilde{\lambda}_{-j} = -\tilde{\lambda}_j$. The eigenvectors corresponding to $\tilde{\lambda}_j$ are denoted by $[\tilde{\mathbf{u}}_j, \tilde{\mathbf{v}}_j]^T$ for $j = 1, 2$. Consequently, the eigenvectors for $\tilde{\lambda}_{-j}$ are given by $[\tilde{\mathbf{v}}_j, \tilde{\mathbf{u}}_j]^T$ for $j = 1, 2$. Thus, the general form of the solution of (2.1.7) is given by

$$\begin{bmatrix}\mathbf{y}^+\\ \mathbf{y}^-\end{bmatrix} = \sum_{j=1}^{2}\left\{\begin{bmatrix}\tilde{\mathbf{u}}_j\\ \tilde{\mathbf{v}}_j\end{bmatrix} a_j(z) + \begin{bmatrix}\tilde{\mathbf{v}}_j\\ \tilde{\mathbf{u}}_j\end{bmatrix} b_j(z)\right\}, \tag{2.1.9}$$

where the functions $a_j(z)$ and $b_j(z)$, for $j = 1, 2$, are to be determined. For the homogeneous problem, in which $\mathbf{q}^\pm = \mathbf{0}$, these functions are given by $\tilde{a}_j(z) = \tilde{\alpha}_j e^{\tilde{\lambda}_j(z - z_1)}$, and $\tilde{b}_j(z) = \tilde{\beta}_j e^{-\tilde{\lambda}_j z}$ where the coefficients $\tilde{\alpha}_j$ and $\tilde{\beta}_j$ for $j = 1, 2$ are determined by imposing that the solution satisfies the boundary conditions in (2.1.6).

2.2 Deriving the Kubelka-Munk equations

The generalized Kubelka-Munk equations are a 4×4 system of first-order differential equations. Its general solution given in (2.1.9) is a superposition of four linearly independent solutions. From the homogeneous solution, we identify two scales: $\tilde{\lambda}_1$ and $\tilde{\lambda}_2$. In contrast, the Kubelka-Munk equations given in (1.1.1) is a first-order system with only one scale: $\sqrt{K(K+2S)}$. This is a known quantity, and in order to justify this, we examine (1.1.1),

written in matrix form as

$$\frac{d}{dz}\begin{bmatrix}F^+\\F^-\end{bmatrix}=\begin{bmatrix}-(K+S) & S\\ -S & K+S\end{bmatrix}\begin{bmatrix}F^+\\F^-\end{bmatrix}. \tag{2.2.1}$$

The corresponding eigenvalue problem is

$$\lambda\begin{bmatrix}u\\v\end{bmatrix}=\begin{bmatrix}-(K+S) & S\\ -S & K+S\end{bmatrix}\begin{bmatrix}u\\v\end{bmatrix}, \tag{2.2.2}$$

whose characteristic equation is $\lambda^2-(K+S)^2+S^2=0$. This is readily solved to yield $\lambda=\pm\sqrt{K(K+2S)}$.

To derive the Kubelka-Munk equations, we study the DP_1 system for the case of strong multiple scattering. When multiple scattering is dominant, $\varpi_0\sim 1$. For that case, we compute an asymptotic solution of the generalized eigenvalue problem (1.4.13) for the DP_1 system from which we derive the Kubelka-Munk equations. To make the assumption of strong multiple scattering precise, we introduce the small, dimensionless parameter, $0<\epsilon\ll 1$, and write $\varpi_0=1-\epsilon^2$, where $\epsilon^2=\mu_a/(\mu_s+\mu_a)$. For that case, after rearranging terms, (1.4.13) becomes

$$\lambda\begin{bmatrix}A & 0\\ 0 & -A\end{bmatrix}\begin{bmatrix}\mathbf{u}\\\mathbf{v}\end{bmatrix}+\epsilon^2\begin{bmatrix}H^{(1)} & H^{(2)}\\ H^{(2)} & H^{(1)}\end{bmatrix}\begin{bmatrix}\mathbf{u}\\\mathbf{v}\end{bmatrix}=\begin{bmatrix}H^{(1)}-\mathbb{I} & H^{(2)}\\ H^{(2)} & H^{(1)}-\mathbb{I}\end{bmatrix}\begin{bmatrix}\mathbf{u}\\\mathbf{v}\end{bmatrix}. \tag{2.2.3}$$

We obtain below an asymptotic solution to this generalized eigenvalue problem in the limit as $\epsilon\to 0^+$.

When $\epsilon=0$, (2.2.3) reduces to

$$\lambda\begin{bmatrix}A & 0\\ 0 & -A\end{bmatrix}\begin{bmatrix}\mathbf{u}\\\mathbf{v}\end{bmatrix}=\begin{bmatrix}H^{(1)}-\mathbb{I} & H^{(2)}\\ H^{(2)} & H^{(1)}-\mathbb{I}\end{bmatrix}\begin{bmatrix}\mathbf{u}\\\mathbf{v}\end{bmatrix}. \tag{2.2.4}$$

We recognize that this is the case when $\varpi_0=1$ for (1.4.7), for which $I=$ constant is a solution. This constant solution corresponds to the solution $\lambda=0$ and $\mathbf{u}=\mathbf{v}=\hat{\mathbf{e}}_1$, where $\hat{\mathbf{e}}_1=[1,0]^T$. Substituting this solution into (2.2.4) yields $H^{(1)}\hat{\mathbf{e}}_1+H^{(2)}\hat{\mathbf{e}}_1=\hat{\mathbf{e}}_1$. In other words, the sum of the first columns of $H^{(1)}$ and $H^{(2)}$ must be equal to $\hat{\mathbf{e}}_1$, a consequence of the normalization of the scattering phase function in (1.2.2).

The eigenvalue $\lambda=0$ is a double root of the characteristic polynomial associated with (2.2.4). By factoring out this double root from the characteristic polynomial, we obtain a quadratic equation with roots $\pm\lambda_2$, with $\lambda_2=O(1)$. We now use perturbation theory to obtain higher order corrections to the $\lambda=0$ eigenvalue. We will therefore, with the symmetry property given in (1.4.18), find the smallest (in magnitude) eigenvalues, $\pm\lambda_1$, and their corresponding eigenvectors, given by $[\mathbf{u}_1,\mathbf{v}_1]^T$ and $[\mathbf{v}_1,\mathbf{u}_1]^T$, respectively.

We seek these higher order corrections in the form $\lambda_1=\epsilon\lambda_1'+\epsilon^2\lambda_1''+O(\epsilon^3)$ and $[\mathbf{u},\mathbf{v}]^T=[\hat{\mathbf{e}}_1,\hat{\mathbf{e}}_1]^T+\epsilon[\mathbf{u}_1',\mathbf{v}_1']^T+\epsilon^2[\mathbf{u}_1'',\mathbf{v}_1'']^T+O(\epsilon^3)$. Substituting these asymptotic expansions into (1.4.13), and collecting like-powers of ϵ, we find to $O(\epsilon)$ that

$$\lambda_1'\begin{bmatrix}A\hat{\mathbf{e}}_1\\ -A\hat{\mathbf{e}}_1\end{bmatrix}=\begin{bmatrix}H^{(1)}-\mathbb{I} & H^{(2)}\\ H^{(2)} & H^{(1)}-\mathbb{I}\end{bmatrix}\begin{bmatrix}\mathbf{u}_1'\\\mathbf{v}_1'\end{bmatrix}. \tag{2.2.5}$$

For (2.2.5) to have a unique solution, its left-hand side must be orthogonal to $[\hat{\mathbf{e}}_1,\hat{\mathbf{e}}_1]^T$. Multiplying the left-hand side of (2.2.5) by $[\hat{\mathbf{e}}_1,\hat{\mathbf{e}}_1]$, we obtain zero identically, so that

this condition is satisfied. Next, we recognize that $\mathbf{m}_1 = A\hat{\mathbf{e}}_1$ is the first column of A, whose entries, according to (1.4.8), correspond to the projection of μ onto $\tilde{P}_m(\mu)$ for $m = 0, 1, 2, \cdots$. Therefore, the vector $[\mathbf{m}_1, -\mathbf{m}_1]^T$ corresponds to expansion coefficients for the functions $I^{\pm} = \pm\mu$. According to (1.2.3), μ (over the whole range $[-1, 1]$) is an eigenfunction of the integral operator in (1.2.6), with eigenvalue g. Consequently, the vector $[\mathbf{m}_1, -\mathbf{m}_1]^T$ is an eigenvector of the matrix in the right-hand side of (2.2.5), with eigenvalue $-(1-g)$. Therefore, we find that

$$\begin{bmatrix} \mathbf{u}_1' \\ \mathbf{v}_1' \end{bmatrix} = -\frac{\lambda_1'}{1-g} \begin{bmatrix} \mathbf{m}_1 \\ -\mathbf{m}_1 \end{bmatrix}. \tag{2.2.6}$$

To determine λ_1', we continue on to $O(\epsilon^2)$, in which we find that

$$\lambda_1'' \begin{bmatrix} A & 0 \\ 0 & -A \end{bmatrix} \begin{bmatrix} \hat{\mathbf{e}}_1 \\ \hat{\mathbf{e}}_1 \end{bmatrix} + \lambda_1' \begin{bmatrix} A & 0 \\ 0 & -A \end{bmatrix} \begin{bmatrix} \mathbf{u}_1' \\ \mathbf{v}_1' \end{bmatrix} + \begin{bmatrix} H^{(1)} & H^{(2)} \\ H^{(2)} & H^{(1)} \end{bmatrix} \begin{bmatrix} \hat{\mathbf{e}}_1 \\ \hat{\mathbf{e}}_1 \end{bmatrix} = \begin{bmatrix} H^{(1)} - \mathbb{I} & H^{(2)} \\ H^{(2)} & H^{(1)} - \mathbb{I} \end{bmatrix} \begin{bmatrix} \mathbf{u}_1'' \\ \mathbf{v}_1'' \end{bmatrix}. \tag{2.2.7}$$

The left-hand side of (2.2.7) must be orthogonal to $[\hat{\mathbf{e}}_1, \hat{\mathbf{e}}_1]^T$. By left-multiplying $[\hat{\mathbf{e}}_1, \hat{\mathbf{e}}_1]$ to the left-hand side of (2.2.7), setting that result to zero, substituting (2.2.6), and making use of the fact that $H^{(1)}\hat{\mathbf{e}}_1 + H^{(2)}\hat{\mathbf{e}}_1 = \hat{\mathbf{e}}_1$, we obtain, upon solving for ${\lambda_1'}^2$, that

$${\lambda_1'}^2 = \frac{(1-g)}{\|\mathbf{m}_1\|^2}. \tag{2.2.8}$$

According to (1.4.8), $\mathbf{m}_1 = [\frac{1}{2}, \frac{1}{2\sqrt{3}}]^T$. Thus, $\|\mathbf{m}_1\|^2 = 1/3$, and so $\lambda_1' = \sqrt{3(1-g)}$.

Thus, we have determined that $\lambda_1 = \epsilon\sqrt{3(1-g)} + O(\epsilon^2)$ is an eigenvalue with corresponding eigenvector $[\mathbf{u}_1, \mathbf{v}_1]^T = [\hat{\mathbf{e}}_1 - \epsilon\sqrt{3/(1-g)}\mathbf{m}_1, \hat{\mathbf{e}}_1 + \epsilon\sqrt{3/(1-g)}\mathbf{m}_1]^T + O(\epsilon^2)$. By the symmetry property of the eigenvalues, $-\lambda_1 = -\epsilon\sqrt{3(1-g)}$ is also an eigenvalue with corresponding eigenvector $[\mathbf{v}_1, \mathbf{u}_1]^T = [\hat{\mathbf{e}}_1 + \epsilon\sqrt{3/(1-g)}\mathbf{m}_1, \hat{\mathbf{e}}_1 - \epsilon\sqrt{3/(1-g)}\mathbf{m}_1]^T + O(\epsilon^2)$.

Since $\lambda_1 = O(\epsilon)$ is much smaller than $\lambda_2 = O(1)$, the leading order behavior of $\mathbf{c}^{\pm}$, governed by (1.4.7) when $\mathbf{q}^{\pm} = \mathbf{0}$, is given by

$$\begin{bmatrix} \mathbf{c}^+ \\ \mathbf{c}^- \end{bmatrix} \sim \begin{bmatrix} \mathbf{u}_1 \\ \mathbf{v}_1 \end{bmatrix} e^{\lambda_1(z-z_1)}\alpha_1 + \begin{bmatrix} \mathbf{v}_1 \\ \mathbf{u}_1 \end{bmatrix} e^{-\lambda_1 z}\beta_1 \tag{2.2.9}$$

in $0 < z < z_1$, where α_1 and β_1 are undetermined, scalar coefficients. Using (2.1.1) and our asymptotic results for $\mathbf{u}_1$ and $\mathbf{v}_1$, we find that

$$\begin{bmatrix} F^+ \\ F^- \end{bmatrix} = \begin{bmatrix} \bar{u} & \bar{v} \\ \bar{v} & \bar{u} \end{bmatrix} \begin{bmatrix} e^{\lambda_1(z-z_1)} & 0 \\ 0 & e^{-\lambda_1 z} \end{bmatrix} \begin{bmatrix} \alpha_1 \\ \beta_1 \end{bmatrix}, \tag{2.2.10}$$

with $\bar{u} = 1/2 - \epsilon/\sqrt{3(1-g)}$ and $\bar{v} = 1/2 + \epsilon/\sqrt{3(1-g)}$. Equation (2.2.10) is the general solution of the first-order system

$$\frac{\mathrm{d}}{\mathrm{d}\tau} \begin{bmatrix} F^+ \\ F^- \end{bmatrix} = \begin{bmatrix} \bar{u} & \bar{v} \\ \bar{v} & \bar{u} \end{bmatrix} \begin{bmatrix} \lambda_1 & 0 \\ 0 & -\lambda_1 \end{bmatrix} \begin{bmatrix} \bar{u} & \bar{v} \\ \bar{v} & \bar{u} \end{bmatrix}^{-1} \begin{bmatrix} F^+ \\ F^- \end{bmatrix}. \tag{2.2.11}$$

Substituting $\lambda_1 = \epsilon\sqrt{3(1-g)}$, $\epsilon = \sqrt{1-\varpi_0}$, and carrying out the matrix products in (2.2.11),

we obtain the Kubelka-Munk equations, given in (1.1.1), with

$$K = 2(1 - \varpi_0), \tag{2.2.12}$$

$$S = \frac{3}{4}(1 - g) - (1 - \varpi_0). \tag{2.2.13}$$

Let $\tilde{K} = (\mu_s + \mu_a)K$ and $\tilde{S} = (\mu_s + \mu_a)S$. Using $\varpi_0 = \mu_s/(\mu_s + \mu_a)$ and (2.2.12), we find that $\tilde{K} = 2\mu_a$. Similarly, using (2.2.13), we find that $\tilde{S} = \frac{3}{4}\mu_s(1 - g) - \frac{1}{4}\mu_a(1 - 3g)$.

The physically correct values for $\tilde{K}$ and $\tilde{S}$ have been the subject of several studies (see Refs. [16, 18, 30, 31] and references contained therein). Thennadil [18] summarizes different values found in the literature by introducing the parameters x and y and a general form for these coefficients: $\tilde{K} = 2\mu_a$ and $\tilde{S} = y\mu_s(1 - g) - x\mu_a$. For example, Gate [12] gives $x = 0$, and $y = \frac{3}{4}$. Brinkworth [11] gives $x = 1$ and $y = \frac{3}{4}$. Star *et al.* [32] give $x = \frac{1}{4}$ and $y = \frac{3}{4}$, which resembles the results above closest. The difference in the value for $\tilde{S}$ obtained above in that it has an additional term that is proportional to the product $\mu_a g$.

This derivation of the Kubelka-Munk equations is based on the assumption of strong multiple scattering. For that case, we find a separation of scales corresponding to $\lambda_1 \ll \lambda_2$. Notice that the leading order asymptotic behavior given in (2.2.9) is defined on the open interval $0 < z < z_1$. This leading order asymptotic behavior is equivalent to neglecting terms with $\tilde{\lambda}_2$ in the solution of the generalized Kubelka-Munk equations. Consequently, we have neglected two of the four linearly independent solutions for $F^{\pm}$ in generalized Kubelka-Munk to derive Kubelka-Munk. It is for this reason that one must introduce the so-called four-flux theory to deal with collimated sources [2], for example. The addition of those two fluxes in four-flux theory is compensating for neglecting those other two solutions that are in the generalized Kubelka-Munk equations.

2.3 Numerical results

In this section, we compare results from numerical solutions of the radiative transfer equation, the generalized Kubelka-Munk equations, and the Kubelka-Munk equations. We first study numerical solutions of these equations for a homogeneous problem. Then, we study the nonhomogeneous problem for the diffuse flux.

2.3.1 Homogeneous problem

We begin by studying the following homogeneous boundary value problem for the radiative transfer equation

$$\mu\frac{\partial I}{\partial \tau} + I = \frac{\varpi_0}{2}\int_{-1}^{1} h(\mu, \mu')I(\mu', \tau)\mathrm{d}\mu' \quad \text{in } 0 < \tau < \tau_1, \tag{2.3.1a}$$

$$I(\mu, 0) = e^{-100(\mu-1)^2} \quad \text{on } 0 < \mu \leq 1, \tag{2.3.1b}$$

$$I(\mu, \tau_1) = 1 \quad \text{on } -1 \leq \mu < 0. \tag{2.3.1c}$$

Here we have replaced z by τ to maintain consistency with the work the author has done previously [33]. To solve boundary value problem (2.3.1), we use the discrete ordinate method described in Chapter 11 of [2]. In particular, we use the Henyey-Greenstein scat-

tering phase function to compute the redistribution function defined as

$$h(\mu,\mu') = \frac{2(1-g^2)}{\pi(a-b)\sqrt{a+b}} E\left(\frac{2b}{a+b}\right), \tag{2.3.2}$$

where $a = 1+g^2-2g\mu\mu'$, $b = 2g\sqrt{1-\mu^2}\sqrt{1-\mu'^2}$, and $E(k)$ is the complete elliptic integral of the second kind. Upon numerical solution of boundary value problem (2.3.1), we compute $F^{\pm}$ defined in (2.1.1) using the same Gauss-Legendre quadrature rule used for the discrete ordinate method.

For the generalized Kubelka-Munk system, we calculated numerically the entries of $H^{(1)}$ and $H^{(2)}$ using h defined in (2.3.2), and Gauss-Legendre quadrature. We also compute the vectors $\mathbf{f}^{\pm}$ defined in (1.4.12) using Gauss-Legendre quadrature. With those matrices and vectors defined, we solve numerically the generalized eigenvalue problem (1.4.13) and obtain $\tilde{\lambda}_j$, $\tilde{\mathbf{u}}_j$, and $\tilde{\mathbf{v}}_j$ for $j = 1, 2$. The solution of the generalized Kubelka-Munk equations is given by (2.1.9) with $\tilde{a}_j(\tau) = e^{\tilde{\lambda}_j(\tau-\tau_1)}\tilde{\alpha}_j$, and $\tilde{b}_j(\tau) = e^{-\tilde{\lambda}_j\tau}\tilde{\beta}_j$. Evaluating this solution at $\tau = 0$ and substituting that result into (2.1.6a), we find that

$$\sum_{j=1}^{2}\left\{\tilde{\mathbf{u}}_j e^{-\tilde{\lambda}_j\tau_1}\tilde{\alpha}_j + \tilde{\mathbf{v}}_j\tilde{\beta}_j\right\} = A\mathbf{f}^{+}. \tag{2.3.3}$$

Evaluating the solution at $\tau = \tau_1$ and substituting that result into (2.1.6b), we find that

$$\sum_{j=1}^{2}\left\{\tilde{\mathbf{v}}_j\tilde{\alpha}_j + \tilde{\mathbf{u}}_j e^{-\tilde{\lambda}_j\tau_1}\tilde{\beta}_j\right\} = A\mathbf{f}^{-}. \tag{2.3.4}$$

Combining (2.3.3) and (2.3.4) yields a 4×4 linear system of equations for $\tilde{\alpha}_j$ and $\tilde{\beta}_j$ for $j = 1, 2$. With $\tilde{\alpha}_j$ and $\tilde{\beta}_j$ determined, we compute $F^{\pm}$ through evaluation of

$$F^{+}(\tau) = \sum_{j=1}^{2}\{\tilde{U}_{1j}e^{\tilde{\lambda}_j(\tau-\tau_1)}\tilde{\alpha}_j + \tilde{V}_{1j}e^{-\tilde{\lambda}_j\tau_1}\tilde{\beta}_j\}, \tag{2.3.5}$$

$$F^{-}(\tau) = \sum_{j=1}^{2}\{\tilde{V}_{1j}e^{\tilde{\lambda}_j(\tau-\tau_1)}\tilde{\alpha}_j + \tilde{U}_{1j}e^{-\tilde{\lambda}_j\tau_1}\tilde{\beta}_j\}. \tag{2.3.6}$$

Here, $\tilde{U}_{1j}$ denotes the first entry of $\tilde{\mathbf{u}}_j$, and $\tilde{V}_{1j}$ denotes the first entry of $\tilde{\mathbf{v}}_j$.

We solve the Kubelka-Munk system (1.1.1) using K and S defined in (2.2.12) and (2.2.13), respectively. We supplement this system with the boundary conditions

$$F^{+}(0) = \int_0^1 f^{+}(\mu)\mu\mathrm{d}\mu, \tag{2.3.7}$$

$$F^{-}(\tau_1) = \int_0^1 f^{-}(-\mu)\mu\mathrm{d}\mu. \tag{2.3.8}$$

We compute the integrals in (2.3.7) and (2.3.8) using Gauss-Legendre quadrature.

In Fig. 2.1 we show results comparing solutions to (2.3.1) computed using the radiative transfer equation (solid curves), the generalized Kubelka-Munk equations (dashed curves), and the Kubelka-Munk equations (dot-dashed curves). Here, we have set $\tau_1 = 1$, $\varpi_0 = 0.99$,

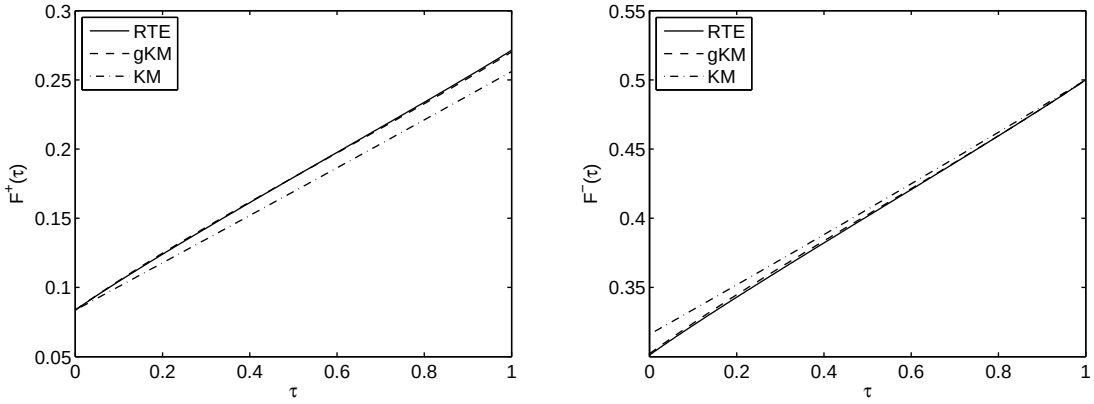

Figure 2.1: Comparisons of $F^+(\tau)$ (left) and $F^-(\tau)$ (right) computed from solutions of boundary value problem (2.3.1) using the radiative transfer equation (RTE), the generalized Kubelka-Munk (gKM) equations, and the Kubelka-Munk (KM) equations. Here, $\tau_1 = 1$, $\varpi_0 = 0.99$, and $g = 0$.

and $g = 0$. The left plot shows F^+ as a function of τ, and the right plot shows F^- as a function of τ. The generalized Kubelka-Munk theory gives a more accurate solution compared to Kubelka-Munk theory. It is nearly indistinguishable from that computed through the solution of the radiative transport equation.

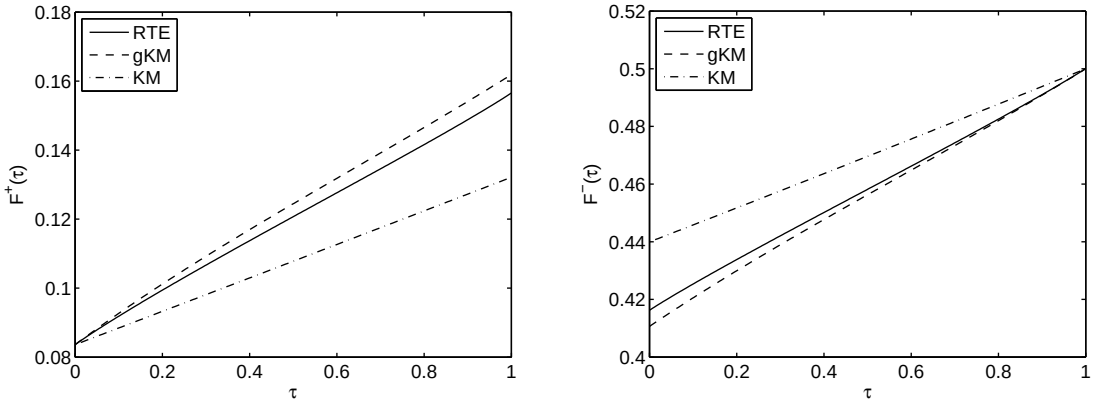

Figure 2.2: Comparisons of $F^+(\tau)$ (left) and $F^-(\tau)$ (right) computed from solutions of boundary value problem (2.3.1) using the radiative transfer equation (RTE), the generalized Kubelka-Munk (gKM) equations, and the Kubelka-Munk (KM) equations. Here, $\tau_1 = 1$, $\varpi_0 = 0.99$, and $g = 0.8$.

In Fig. 2.2 we plot the results when $\varpi_0 = 0.99$, and $g = 0.8$. For this case, scattering is forward-peaked. Consequently, the specific intensity is not approximated well by a piecewise linear approximation. Thus, DP_1 is not as good of an approximation, which, in turn, means that the generalized Kubelka-Munk and Kubelka-Munk systems are less accurate. This is evidenced by the fact that both the generalized Kubelka-Munk and Kubelka-Munk results are less accurate than those shown in Fig. 2.1. Nonetheless, Fig. 2.2 shows that the gKM equations are still much more accurate than the KM equations.

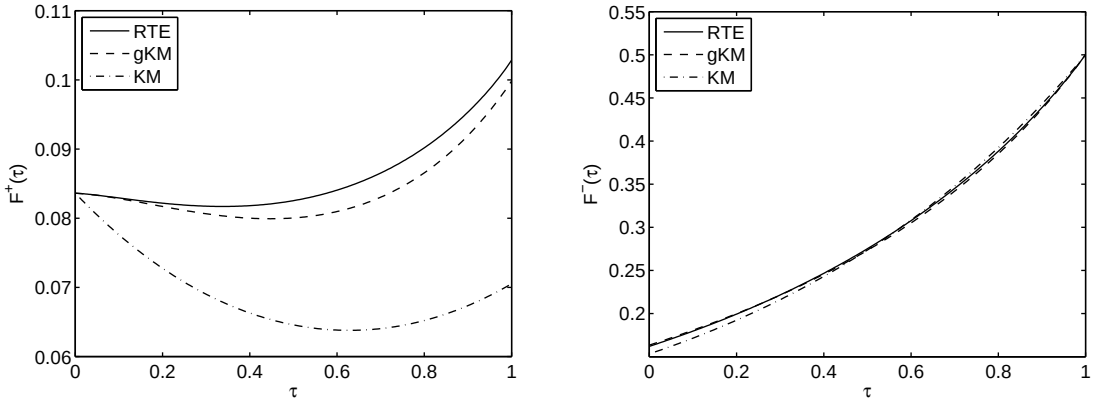

Figure 2.3: Comparisons of $F^+(\tau)$ (left) and $F^-(\tau)$ (right) computed from solutions of boundary value problem (2.3.1) using the radiative transfer equation (RTE), the generalized Kubelka-Munk (gKM) equations, and the Kubelka-Munk (KM) equations. Here, $\tau_1 = 1$, $\varpi_0 = 0.5$, and $g = 0$.

Next, we investigate reducing the value of ϖ_0. For this case, the Kubelka-Munk equations are known to be inaccurate [18, 20, 30]. Fig. 3.3 shows results for $\varpi_0 = 0.5$ and $g = 0$. Although scattering is isotropic, so that $g = 0$, we find that the KM equations are much less accurate than the generalized Kubelka-Munk equations. The error is worse for $F^+(\tau)$ than for $F^-(\tau)$ presumably because it must also take into account the non-constant boundary condition (2.3.1b). When scattering is also forward-peaked, as shown in Fig. 2.4, we find that the Kubelka-Munk equations produce negative values for F^+, which are unphysical. However, even with $\varpi_0 = 0.5$, the gKM equations yield accurate results. Even at a lower albedo ($\varpi \sim 0$), the generalized Kubelka-Munk equations yield qualitatively correct results. Although we do not show these results here, we have found that computing solutions with smaller ($\tau_1 \sim 0.1$) and larger ($\tau_1 \sim 10$) optical thicknesses yield similar results to those shown here.

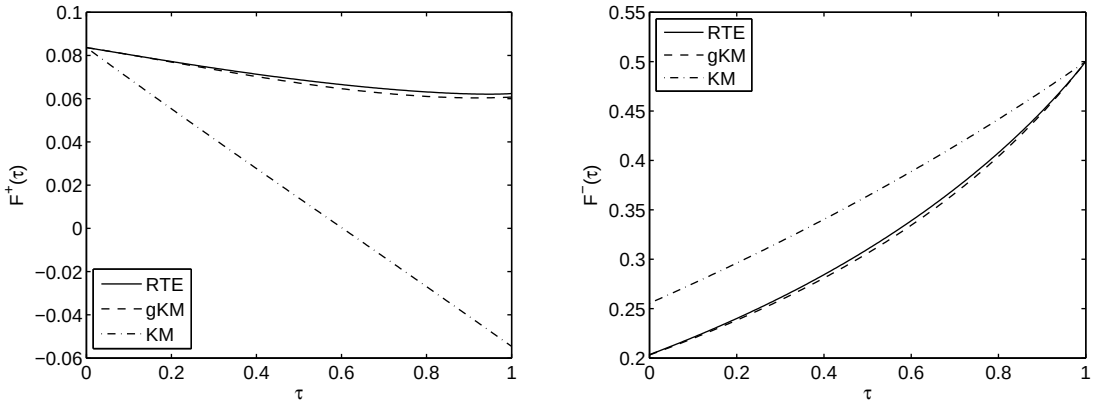

Figure 2.4: Comparisons of $F^+(\tau)$ (left) and $F^-(\tau)$ (right) computed from solutions of boundary value problem (2.3.1) using the radiative transfer equation (RTE), the generalized Kubelka-Munk (gKM) equations, and the Kubelka-Munk (KM) equations. Here, $\tau_1 = 1$, $\varpi_0 = 0.5$, and $g = 0.8$.

2.3.2 Nonhomogeneous problem for the diffuse flux

We now study the boundary value problem

$$\mu\frac{\partial I}{\partial\tau}+I=\frac{\varpi_0}{2}\int_{-1}^{1}h(\mu,\mu')I(\mu',\tau)\mathrm{d}\mu' \quad \text{in } 0<\tau<\tau_1, \tag{2.3.9a}$$

$$I(\mu,0)=\delta(\mu-\mu_0) \quad \text{on } 0<\mu\leq 1, \tag{2.3.9b}$$

$$I(\mu,\tau_1)=0 \quad \text{on } -1\leq\mu<0. \tag{2.3.9c}$$

This boundary value problem governs a plane wave with unit incident flux on a plane-parallel slab in the direction $\mu=\mu_0$. It is a fundamental problem in the study of radiative transfer [1, 2]. A complication in solving boundary value problem (2.3.9) is the Dirac delta function appearing in boundary condition (2.3.9b). To study this problem, one represents the specific intensity as the sum $I=I_{\mathrm{ri}}+I_{\mathrm{d}}$. Here, I_{ri} denotes the reduced intensity satisfying

$$\mu\frac{\partial I_{\mathrm{ri}}}{\partial\tau}+I_{\mathrm{ri}}=0, \tag{2.3.10a}$$

$$I_{\mathrm{ri}}(\mu,0)=\delta(\mu-\mu_0) \quad \text{on } 0<\mu\leq 1, \tag{2.3.10b}$$

$$I_{\mathrm{ri}}(\mu,\tau_1)=0 \quad \text{on } -1\leq\mu<0. \tag{2.3.10c}$$

The solution of boundary value problem (2.3.10) is readily found to be $I_{\mathrm{ri}}=\delta(\mu-\mu_0)e^{-\tau/\mu}$. The diffuse intensity, I_{d}, satisfies the following nonhomogeneous, boundary value problem for the radiative transfer equation:

$$\mu\frac{\partial I_{\mathrm{d}}}{\partial\tau}+I_{\mathrm{d}}=\frac{\varpi_0}{2}\int_{-1}^{1}h(\mu,\mu')I_{\mathrm{d}}(\mu',\tau)\mathrm{d}\mu'+Q_{\mathrm{ri}}, \tag{2.3.11a}$$

$$I_{\mathrm{d}}(\mu,0)=0 \quad \text{on } 0<\mu\leq 1, \tag{2.3.11b}$$

$$I_{\mathrm{d}}(\mu,\tau_1)=0 \quad \text{on } -1\leq\mu<0. \tag{2.3.11c}$$

The nonhomogeneous term, $Q_{\mathrm{ri}}=\frac{1}{2}\varpi_0 h(\mu,\mu_0)e^{-\tau/\mu_0}$, in (2.3.11a) comes from inserting I_{ri} into the integral operation in the radiative transport equation.

We compute the diffuse fluxes, defined as

$$F_{\mathrm{d}}^{\pm}(\tau)=\int_0^1 I_{\mathrm{d}}(\mu,\tau)\mu\mathrm{d}\mu, \tag{2.3.12}$$

by solving boundary value problem (2.3.11) directly, and by solving the generalized Kubelka-Munk equations for this problem. To solve boundary value problem (2.3.11), we use the same method that we use to solve boundary value problem (2.3.1). The generalized Kubelka-Munk equations for this problem take the form

$$\begin{bmatrix}\mathbb{I} & 0\\ 0 & -\mathbb{I}\end{bmatrix}\frac{\mathrm{d}}{\mathrm{d}\tau}\begin{bmatrix}\mathbf{y}^+\\ \mathbf{y}^-\end{bmatrix}=\begin{bmatrix}S_1 & S_2\\ S_2 & S_1\end{bmatrix}\begin{bmatrix}\mathbf{y}^+\\ \mathbf{y}^-\end{bmatrix}+\frac{\varpi_0}{2}\begin{bmatrix}\mathbf{h}^+\\ \mathbf{h}^-\end{bmatrix}e^{-\tau/\mu_0}, \tag{2.3.13}$$

where the entries of the vectors $\mathbf{h}^{\pm}$ are given by

$$h_{n+1}^{\pm}=\int_0^1 h(\pm\mu,\mu_0)P_n(\mu)\mathrm{d}\mu, \quad n=0,1. \tag{2.3.14}$$

We compute the solution of (2.3.13) as the sum of the homogeneous and particular solutions: $\mathbf{y}^{\pm} = \mathbf{y}_H^{\pm} + \mathbf{y}_P^{\pm}$. We seek the particular solution in the form $\mathbf{y}_P^{\pm} = \boldsymbol{\eta}^{\pm} e^{-\tau/\mu_0}$, where $\boldsymbol{\eta}^{\pm}$ satisfies the 4×4 linear system

$$\begin{bmatrix} -\mathbb{I} - S_1 & -S_2 \\ -S_2 & \mathbb{I} - S_1 \end{bmatrix} \begin{bmatrix} \boldsymbol{\eta}^{+} \\ \boldsymbol{\eta}^{-} \end{bmatrix} = \frac{\varpi_0}{2} \begin{bmatrix} \mathbf{h}^{+} \\ \mathbf{h}^{-} \end{bmatrix}. \tag{2.3.15}$$

The homogeneous solution $\mathbf{y}_H^{\pm}$ is given by (2.1.9) with $\tilde{a}_j(\tau) = e^{\tilde{\lambda}_j \tau} \tilde{\alpha}_j$, and $\tilde{b}_j(\tau) = e^{-\tilde{\lambda}_j \tau} \tilde{\beta}_j$. Evaluating our results for $\mathbf{y}^{\pm} = \mathbf{y}_H^{\pm} + \mathbf{y}_P^{\pm}$ at $\tau = 0$ and substituting that result into (2.1.6a) with $\mathbf{f}^{+} = \mathbf{0}$, we find that

$$\sum_{j=1}^{2} \left\{ \tilde{\mathbf{u}}_j e^{-\tilde{\lambda}_j \tau_1} \tilde{\alpha}_j + \tilde{\mathbf{v}}_j \tilde{\beta}_j \right\} = -\boldsymbol{\eta}^{+} \tag{2.3.16}$$

Evaluating the solution at $\tau = \tau_1$ and substituting that result into (2.1.6b) with $\mathbf{f}^{-} = \mathbf{0}$, we find that

$$\sum_{j=1}^{2} \left\{ \tilde{\mathbf{v}}_j \tilde{\alpha}_j + \tilde{\mathbf{u}}_j e^{-\tilde{\lambda}_j \tau_1} \tilde{\beta}_j \right\} = -\boldsymbol{\eta}^{-} e^{-\tau_1/\mu_0}. \tag{2.3.17}$$

Combining (2.3.3) and (2.3.4) yields a 4×4 linear system of equations for $\tilde{\alpha}_j$ and $\tilde{\beta}_j$ for $j = 1, 2$. With $\tilde{\alpha}_j$ and $\tilde{\beta}_j$ determined, we compute $F^{\pm}$ through evaluation of

$$F^{+}(\tau) = \sum_{j=1}^{2} \{ \tilde{U}_{1j} e^{\tilde{\lambda}_j (\tau - \tau_1)} \tilde{\alpha}_j + \tilde{V}_{1j} e^{-\tilde{\lambda}_j \tau} \tilde{\beta}_j \} + \eta_1^{+} e^{-\tau/\mu_0}, \tag{2.3.18}$$

$$F^{-}(\tau) = \sum_{j=1}^{2} \{ \tilde{V}_{1j} e^{\tilde{\lambda}_j (\tau - \tau_1)} \tilde{\alpha}_j + \tilde{U}_{1j} e^{-\tilde{\lambda}_j \tau} \tilde{\beta}_j \} + \eta_1^{-} e^{-\tau/\mu_0}, \tag{2.3.19}$$

with $\eta_1^{\pm}$ denoting the first entries of $\boldsymbol{\eta}^{\pm}$.

In Fig. 2.5, we compare the diffuse fluxes computed from solutions of (2.3.11) by solving the radiative transfer equation (solid curves), and the generalized Kubelka-Munk equations (dashed curves). Here, we have set $\tau_1 = 1$, $\varpi_0 = 0.99$, and $g = 0$ with $\mu_0 = 1.0$. Here, the gKM equations provide a very accurate approximation to the radiative transfer equation. Fig. 2.6 compares the diffuse fluxes for the case in which $g = 0.7$. As expected, the approximation produced by the generalized Kubelka-Munk equations are less accurate when scattering is forward-peaked than when it is isotropic. Nonetheless, the gKM equations still provide an accurate approximation to the radiative transfer equation for the diffuse fluxes. Although we do not show these results here, we find that generalized Kubelka-Munk equations still approximate the radiative transfer equation in the manner shown in Figs. 2.5 and 2.6 with lower albedo values, and for both smaller and larger optical thicknesses.

2.4 Summary of results

We have systematically derived the KM equations from the RTE. This derivation involves the application of the DP_n method to solve the RTE. By transforming the DP_1 system of equations, we obtained the gKM equations. Then, by studying the DP_1 system of equations in the limit of strong multiple scattering, we derived the KM equations.

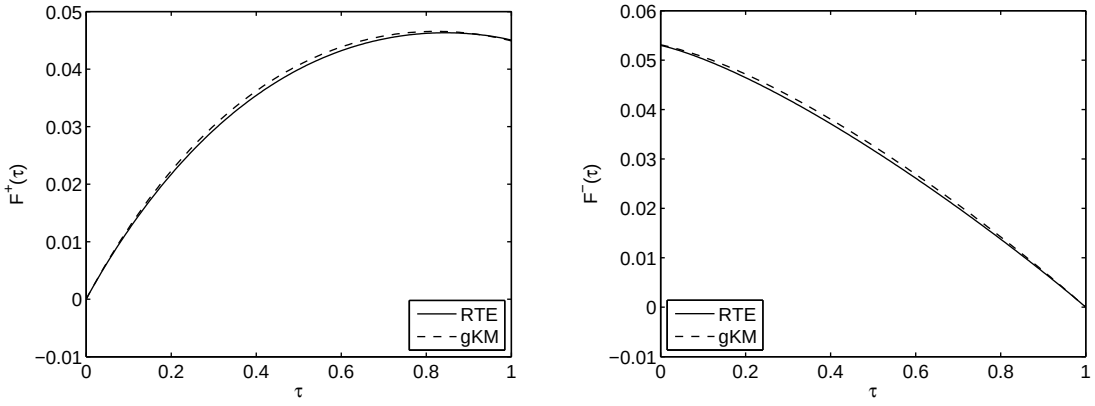

Figure 2.5: Comparisons of $F^+(\tau)$ (left) and $F^-(\tau)$ (right) computed from solutions of boundary value problem (2.3.11) using the radiative transfer equation (RTE), and the generalized Kubelka-Munk (gKM) equations. Here, $\tau_1 = 1$, $\varpi_0 = 0.99$, and $g = 0$ with $\mu_0 = 1.0$.

For the KM equations, we have determined all coefficients explicitly. In particular, we have found that $\tilde{K} = 2\mu_a$ and $\tilde{S} = (3/4)\mu_s(1-g) - (1/4)\mu_a(1-3g)$. These results agree closely with those found in the literature. However, the significant difference in the results found here is the term in $\tilde{S}$ proportional to $\mu_a g$. Moreover, we established this theory's range of validity as a consequence of the asymptotic analysis used to derive it.

The gKM equations can easily account for general boundary conditions and nonhomogeneous problems. The numerical results shown here demonstrate that the gKM equations are much better than the KM equations at approximating the solutions of the RTE. The complexity of the gKM equations is only slightly larger, since it is a 4×4 system rather than a 2×2 one. Since it is more accurate than the KM system of equations, more broadly applicable, and only slightly more difficult to solve, the gKM equations should be very useful in all areas that KM theory currently is favored and more.

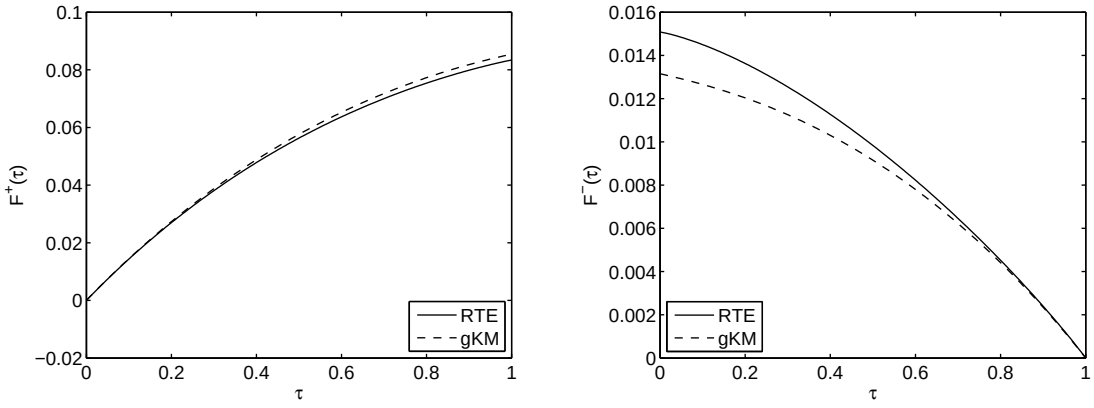

Figure 2.6: Comparisons of $F^+(\tau)$ (left) and $F^-(\tau)$ (right) computed from solutions of boundary value problem (2.3.11) using the radiative transfer equation (RTE), and the generalized Kubelka-Munk (gKM) equations. Here, $\tau_1 = 1$, $\varpi_0 = 0.99$, and $g = 0.7$ with $\mu_0 = 1.0$.

Chapter 3

Extending gKM to three dimensions

Now that we have established the theoretical foundation for KM, we are poised to extend generalized Kubelka-Munk theory to three-dimensions and use that to study the backscattering and transmission of collimated beams by a plane-parallel slab composed of a uniform absorbing and scattering medium. This particular problem is fundamentally important to several applications such as geophysical remote sensing [34, 35] and biomedical optics [4]. In both of these applications, measurements of the radiance due to a collimated beam incident on the medium are used to determine optical properties, thereby revealing important characteristics for these applications. The result of this extension is a 8×8 system of partial differential equations that can be solved readily. Through comparisons with Monte Carlo simulations of the radiative transfer equation, we study the effectiveness of this approximation and identify its range of validity. Besides one dimensional plane-parallel problems, the DP_n approximation has been applied to problems in two dimensions [36], problems with spherically symmetric geometry [37], and two dimensional problems with cylindrically symmetric geometry [29]. To the best of our knowledge, this approximation has not been applied to the problem we study here.

3.1 Three-dimensional transfer equation

We seek to solve (1.2.1) in the plane-parallel slab, $\{\mathbf{r} \in \mathbb{R}^3 | -\infty < x, y < \infty, 0 < z < z_0\}$. On the boundary plane, $z = 0$, we prescribe that

$$I(\hat{\mathbf{\Omega}}, x, y, 0) = F_0 \delta(\hat{\mathbf{\Omega}} - \hat{z}) e^{-2(x^2+y^2)/W_0^2}, \quad \text{on } \hat{\mathbf{\Omega}} \cdot \hat{z} > 0. \tag{3.1.1}$$

Boundary condition (3.1.1) corresponds to a Gaussian beam with beam size W_0 incident normally on the $z = 0$ boundary plane with total power $\frac{1}{2}\pi W_0^2 F_0$ [2, 38, 39]. On the boundary plane, $z = z_0$, we prescribe

$$I(\hat{\mathbf{\Omega}}, x, y, z_0) = 0 \quad \text{on } \hat{\mathbf{\Omega}} \cdot \hat{z} < 0, \tag{3.1.2}$$

corresponding to no light entering into the slab through this boundary.

We seek the solution of the boundary value problem comprised of (1.2.1) with boundary conditions (3.1.1) and (3.1.2) as the sum $I = I_{\text{ri}} + I_{\text{d}}$ where I_{ri} is the reduced intensity

and I_{d} is the diffuse intensity. The reduced intensity is given by [2, 38, 39]

$$I_{\mathrm{ri}}(\hat{\mathbf{\Omega}}, x, y, z) = F_0 \delta(\hat{\mathbf{\Omega}} - \hat{z}) e^{-2(x^2+y^2)/W_0^2 - z}. \tag{3.1.3}$$

This result is an approximation that assumes that beam spread and other geometric factors are negligible compared to attenuation [2]. Consequently, the diffuse intensity satisfies

$$\hat{\mathbf{\Omega}} \cdot \nabla I_{\mathrm{d}} + I_{\mathrm{d}} = \varpi_0 \int_{S^2} p(\hat{\mathbf{\Omega}} \cdot \hat{\mathbf{\Omega}}') I_{\mathrm{d}}(\hat{\mathbf{\Omega}}', \mathbf{r}) \mathrm{d}\hat{\mathbf{\Omega}}' + Q_{\mathrm{ri}} e^{-z}, \tag{3.1.4}$$

where the source term, Q_{ri}, is defined as

$$Q_{\mathrm{ri}} = \varpi_0 F_0 p(\hat{\mathbf{\Omega}} \cdot \hat{z}) e^{-2(x^2+y^2)/W_0^2}. \tag{3.1.5}$$

The boundary conditions are

$$I_{\mathrm{d}}(\hat{\mathbf{\Omega}}, x, y, 0) = 0 \quad \text{on } \hat{\mathbf{\Omega}} \cdot \hat{z} > 0. \tag{3.1.6}$$

and

$$I_{\mathrm{d}}(\hat{\mathbf{\Omega}}, x, y, z_0) = 0 \quad \text{on } \hat{\mathbf{\Omega}} \cdot \hat{z} < 0. \tag{3.1.7}$$

Upon solution of the boundary value problem consisting of (3.1.4) subject to boundary conditions (3.1.6) and (3.1.7), we obtain I_{d}. We then study the spatial distribution of the power flow in the $\pm\hat{z}$ directions by computing

$$F^{\pm}(x, y, z) = \int_{\hat{\mathbf{\Omega}} \cdot (\pm\hat{\mathbf{z}})} I_{\mathrm{d}}(\hat{\mathbf{\Omega}}, x, y, z) \hat{\mathbf{\Omega}} \cdot (\pm\hat{\mathbf{z}}) \mathrm{d}\hat{\mathbf{\Omega}}, \tag{3.1.8}$$

respectively. Note that this particular problem possesses axisymmetry since the beam is incident normally on the slab. This axisymmetry can be used to simplify this problem as is done in [39, 40] and for the results given in Section 8. We proceed first without addressing explicitly this axisymmetry to keep the analysis general.

3.2 Three dimensional generalized Kubelka-Munk equations

In terms of μ and φ, (3.1.4) is given by

$$\begin{aligned} \mu \partial_z I_{\mathrm{d}} + \sqrt{1-\mu^2}(\cos\varphi \partial_x I_{\mathrm{d}} + \sin\varphi \partial_y I_{\mathrm{d}}) + I_{\mathrm{d}} & \\ = \varpi_0 \int_0^{2\pi} \int_{-1}^{1} p(\mu, \mu', \varphi - \varphi') I_{\mathrm{d}}(\mu', \varphi', x, y, z) \mathrm{d}\mu' \mathrm{d}\varphi' & \\ + Q_{\mathrm{ri}}(\mu, x, y) e^{-z}. & \end{aligned} \tag{3.2.1}$$

In light of I_{d} being discontinuous at $\mu = 0$ due to boundary conditions (3.1.6) and (3.1.7), we introduce $I_{\mathrm{d}}^{\pm}(\mu, \varphi, x, y, z) = I_{\mathrm{d}}(\pm\mu, \varphi, x, y, z)$, for $0 < \mu \leq 1$, satisfying the coupled

system

$$\begin{aligned}\pm\mu\partial_z I_{\mathrm{d}}^{\pm} + \sqrt{1-\mu^2}(\cos\varphi\partial_x I_{\mathrm{d}}^{\pm} + \sin\varphi\partial_y I_{\mathrm{d}}^{\pm}) + I_{\mathrm{d}}^{\pm} \\ = \varpi_0 \int_0^{2\pi}\int_0^1 p^{(1)}(\mu,\mu',\varphi-\varphi')I_{\mathrm{d}}^{\pm}(\mu',\varphi',x,y,z)\mathrm{d}\mu'\mathrm{d}\varphi' \\ + \varpi_0 \int_0^{2\pi}\int_0^1 p^{(2)}(\mu,\mu',\varphi-\varphi')I_{\mathrm{d}}^{\mp}(\mu',\varphi',x,y,z)\mathrm{d}\mu'\mathrm{d}\varphi' \\ + Q_{\mathrm{ri}}^{\pm}(\mu,x,y)e^{-z},\end{aligned} \tag{3.2.2}$$

with

$$Q_{\mathrm{ri}}^{\pm}(\mu,x,y) = Q_{\mathrm{ri}}(\pm\mu,x,y), \tag{3.2.3}$$

$$p^{(1)}(\mu,\mu,\varphi-\varphi') = p(\mu,\mu',\varphi-\varphi') \tag{3.2.4}$$

$$p^{(2)}(\mu,\mu',\varphi-\varphi') = p(\mu,-\mu',\varphi-\varphi'). \tag{3.2.5}$$

Because $p = p(\hat{\mathbf{\Omega}}\cdot\hat{\mathbf{\Omega}}')$, it follows that $p(-\mu,-\mu',\varphi-\varphi') = p^{(1)}(\mu,\mu',\varphi-\varphi')$, and $p(-\mu,\mu',\varphi-\varphi') = p^{(2)}(\mu,\mu',\varphi-\varphi')$, which we have used in writing (3.2.2). In terms of $I_{\mathrm{d}}^{\pm}$, boundary conditions (3.1.6) and (3.1.7) are given by

$$I_{\mathrm{d}}^{+}(\mu,\varphi,x,y,0) = 0, \tag{3.2.6}$$

and

$$I_{\mathrm{d}}^{-}(\mu,\varphi,x,y,z_0) = 0, \tag{3.2.7}$$

respectively.

We now apply the double spherical harmonics method to solve (3.2.2) subject to boundary conditions (3.2.6) and (3.2.7). Here, we use the set of spherical harmonics, defined in (1.4.1), to expand I as in (1.4.4). We set $N = 1$ and derive the system of equations for the expansion coefficients, $c_{nm}^{\pm}$. Instead of using $\tilde{Y}_{nm}$ directly, we expand $I_1^{\pm}$ as

$$I_1^{\pm} = \sum_{k=1}^{4} \Phi_k(\mu,\varphi)u_k^{\pm}(x,y,z), \tag{3.2.8}$$

where the orthonormal set of basis functions $\{\Phi_k\}_{k=1}^4$ are defined as

$$\Phi_1 = \frac{1}{\sqrt{2\pi}}, \tag{3.2.9a}$$

$$\Phi_2 = \sqrt{\frac{3}{2\pi}}(2\mu-1), \tag{3.2.9b}$$

$$\Phi_3 = \sqrt{\frac{3}{2\pi}}\sqrt{1-(2\mu-1)^2}\cos\varphi, \tag{3.2.9c}$$

$$\Phi_4 = \sqrt{\frac{3}{2\pi}}\sqrt{1-(2\mu-1)^2}\sin\varphi. \tag{3.2.9d}$$

The expansion coefficients, $u_k^{\pm}$, for $k = 1, 2, 3, 4$, in (3.2.8) satisfy the following system

$$\begin{bmatrix} A & 0 \\ 0 & -A \end{bmatrix} \begin{bmatrix} \mathbf{u}^+ \\ \mathbf{u}^- \end{bmatrix}_z + \begin{bmatrix} B & 0 \\ 0 & B \end{bmatrix} \begin{bmatrix} \mathbf{u}^+ \\ \mathbf{u}^- \end{bmatrix}_x + \begin{bmatrix} C & 0 \\ 0 & C \end{bmatrix} \begin{bmatrix} \mathbf{u}^+ \\ \mathbf{u}^- \end{bmatrix}_y + \begin{bmatrix} \mathbb{I} - \varpi_0 H^{(1)} & -\varpi_0 H^{(2)} \\ -\varpi_0 H^{(2)} & \mathbb{I} - \varpi_0 H^{(1)} \end{bmatrix} \begin{bmatrix} \mathbf{u}^+ \\ \mathbf{u}^- \end{bmatrix} = \begin{bmatrix} \mathbf{q}_{\mathrm{ri}}^+(x, y) \\ \mathbf{q}_{\mathrm{ri}}^-(x, y) \end{bmatrix} e^{-z}. \quad (3.2.10)$$

Here, $\mathbf{u}^{\pm} = (u_1^{\pm}, u_2^{\pm}, u_3^{\pm}, u_4^{\pm})$. Boundary conditions for $\mathbf{u}^{\pm}$ are

$$\mathbf{u}^+(x, y, 0) = 0, \quad (3.2.11)$$

$$\mathbf{u}^-(x, y, z_0) = 0, \quad (3.2.12)$$

respectively. We call the system (3.2.10) subject to boundary conditions (3.2.11) and (3.2.12) the DP_1 equations.

Let (f, g) denote the inner product defined as

$$(f, g) = \int_0^{2\pi} \int_0^1 f(\mu, \varphi) g(\mu, \varphi) \mathrm{d}\mu \mathrm{d}\varphi. \quad (3.2.13)$$

The entries of the 4×4 matrix A are defined as $A_{ij} = (\Phi_i, \mu\Phi_j)$, which yields

$$A = \frac{1}{2} \begin{bmatrix} 1 & \frac{1}{\sqrt{3}} & 0 & 0 \\ \frac{1}{\sqrt{3}} & 1 & 0 & 0 \\ 0 & 0 & 1 & 0 \\ 0 & 0 & 0 & 1 \end{bmatrix}. \quad (3.2.14)$$

The entries of the 4×4 matrices B and C are defined as $B_{ij} = (\Phi_i, \sqrt{1-\mu^2}\cos\varphi\Phi_j)$ and $C_{ij} = (\Phi_i, \sqrt{1-\mu^2}\sin\varphi\Phi_j)$, respectively, which yield

$$B = \begin{bmatrix} 0 & 0 & b & 0 \\ 0 & 0 & c & 0 \\ b & c & 0 & 0 \\ 0 & 0 & 0 & 0 \end{bmatrix}, \quad \text{and} \quad C = \begin{bmatrix} 0 & 0 & 0 & b \\ 0 & 0 & 0 & c \\ 0 & 0 & 0 & 0 \\ b & c & 0 & 0 \end{bmatrix}, \quad (3.2.15)$$

with $b = (11\sqrt{2} - 9\sinh^{-1}(1))/(8\sqrt{3})$ and $c = (75\sinh^{-1}(1) - 49\sqrt{2})/32$. The 4×4 matrices, $H^{(1)}$ and $H^{(2)}$, have entries

$$H_{ij}^{(1,2)} = \int_0^{2\pi} \int_0^1 \Phi_i(\mu, \varphi) \int_0^{2\pi} \int_0^1 p_{1,2}(\mu, \mu', \varphi - \varphi') \Phi_j(\mu', \varphi') \mathrm{d}\mu' \mathrm{d}\varphi' \mathrm{d}\mu \mathrm{d}\varphi, \quad (3.2.16)$$

respectively. We compute these matrix entries numerically. Note that the matrices A, B, C, and $H^{(1,2)}$ are all symmetric. The entries of the vectors $\mathbf{q}_{\mathrm{ri}}^{\pm}$ are defined as $[\mathbf{q}_{\mathrm{ri}}^{\pm}]_i = (\Phi_i, Q_{\mathrm{ri}}^{\pm})$.

The system of generalized Kubelka-Munk equations is simply a linear transformation of the system of DP_1 equations [33]. Substituting $I_1^{\pm}$ given by (3.2.8) into (3.1.8), we find that

$$F^{\pm} = \sqrt{2\pi} \left[\frac{1}{2} u_1^{\pm} + \frac{1}{2\sqrt{3}} u_2^{\pm} \right]. \quad (3.2.17)$$

We also introduce the auxiliary quantities

$$G^{\pm} = \sqrt{2\pi}\left[\frac{1}{2\sqrt{3}}u_1^{\pm} + \frac{1}{2}u_2^{\pm}\right]. \tag{3.2.18}$$

In light of (3.2.17) and (3.2.18), we introduce the linear transformation $\mathbf{v}^{\pm} = \sqrt{2\pi}A\mathbf{u}^{\pm}$, where the components of $\mathbf{v}^{\pm}$ are $\mathbf{v}^{\pm} = (F^{\pm}, G^{\pm}, \sqrt{2\pi}u_3, \sqrt{2\pi}u_4)$. Substituting this linear transformation into (3.2.10), we obtain

$$\begin{bmatrix}\mathbb{I} & 0\\ 0 & -\mathbb{I}\end{bmatrix}\begin{bmatrix}\mathbf{v}^+\\ \mathbf{v}^-\end{bmatrix}_z + \begin{bmatrix}\tilde{B} & 0\\ 0 & \tilde{B}\end{bmatrix}\begin{bmatrix}\mathbf{v}^+\\ \mathbf{v}^-\end{bmatrix}_x + \begin{bmatrix}\tilde{C} & 0\\ 0 & \tilde{C}\end{bmatrix}\begin{bmatrix}\mathbf{v}^+\\ \mathbf{v}^-\end{bmatrix}_y + \begin{bmatrix}\tilde{H}^{(1)} & \tilde{H}^{(2)}\\ \tilde{H}^{(2)} & \tilde{H}^{(1)}\end{bmatrix}\begin{bmatrix}\mathbf{v}^+\\ \mathbf{v}^-\end{bmatrix} = \sqrt{2\pi}\begin{bmatrix}\mathbf{q}_{\mathrm{ri}}^+(x,y)\\ \mathbf{q}_{\mathrm{ri}}^-(x,y)\end{bmatrix}e^{-z}, \tag{3.2.19}$$

with

$$\tilde{B} = BA^{-1} = \begin{bmatrix}0 & 0 & 2b & 0\\ 0 & 0 & 2c & 0\\ 3b-\sqrt{3}c & 3c-\sqrt{3}b & 0 & 0\\ 0 & 0 & 0 & 0\end{bmatrix}, \tag{3.2.20}$$

$$\tilde{C} = CA^{-1} = \begin{bmatrix}0 & 0 & 0 & 2b\\ 0 & 0 & 0 & 2c\\ 0 & 0 & 0 & 0\\ 3b-\sqrt{3}c & 3c-\sqrt{3}b & 0 & 0\end{bmatrix}, \tag{3.2.21}$$

$\tilde{H}^{(1)} = (\mathbb{I} - \varpi_0 H^{(1)})A^{-1}$, and $\tilde{H}^{(2)} = -\varpi_0 H^{(2)}A^{-1}$. By transforming boundary conditions (3.2.8) and (3.2.9), we obtain

$$\mathbf{v}^+(x,y,0) = 0, \tag{3.2.22}$$

$$\mathbf{v}^-(x,y,z_0) = 0. \tag{3.2.23}$$

We call (3.2.19) subject to boundary conditions (3.2.22) and (3.2.23) the generalized Kubelka-Munk equations.

3.3 Numerical results

We now evaluate the accuracy of the generalized Kubelka-Munk (gKM) approximation by comparing its results with those of Monte Carlo (MC) simulations of the full radiative transfer equation. For all of the numerical results shown here, we have set the total power to $P_0 = 1$ and the beam radius to $W_0 = 1$.

For the gKM results, we have used a quasi-fast Hankel transforms, computed on a 256 point radial grid over the interval, $0 < \rho < 20$. For the MC results, we have used the Virtual Photonics Technology Initiative software (`http://virtualphotonics.codeplex.com`). This MC software implements the discrete absorption weighting, which was shown to be more accurate than continuous absorption weighting for moderate to highly absorbing media or isotropic scattering media [41]. For the MC simulations results shown below, we have used 10^7 photons for all cases except for the case in which $\varpi_0 = 0.85$ and $z_0 = 10$, where we have used 10^8 photons. The results shown here used 200 radial detectors over the interval $0 < \rho < 20$.

For one dimensional problems in Chapter 2, the gKM approximation was shown to work best for strong, isotropic scattering media [33]. The gKM approximation is quantitatively accurate for those problems, and it improves as the optical thickness of the medium increases, thereby approaching the diffusion limit. For media with higher absorption, the gKM approximation was shown to be qualitatively accurate, but exhibited larger quantitative error. The gKM approximation exhibited a very large error for highly anisotropic scattering media because the approximation made is not capable of taking into account the angular dependence of the intensity for anisotropic scattering problems. Since the extension to three dimensions presented here is based on the same approximation used for the one dimensional problem, we find in the results below that the performance of the gKM approximation is largely consistent with the performance evaluated for the one dimensional problem.

3.3.1 Isotropic scattering

We first investigate the gKM approximation for isotropic scattering problems for which the scattering phase function is

$$p = \frac{1}{4\pi}. \tag{3.3.1}$$

For that case, $H_{11}^{(1)} = H_{11}^{(2)} = 1/2$, and $H_{ij}^{(1)} = H_{ij}^{(2)} = 0$ otherwise. In Fig. 3.1, we plot the power backscattered, $F^-(\rho, 0)$, [left column] and transmitted, $F^+(\rho, z_0)$, [right column] for a strongly isotropic scattering medium with $\varpi_0 = 0.99$ for optical thicknesses $z_0 = 1$ [top row], 5 [middle row], and 10 [bottom row]. The solid curves show the MC results and the dashed curves show the gKM results.

These results show that the gKM approximation is accurate for optically thick, isotropic scattering media. For the $z_0 = 1$ results, we see that the gKM approximation is accurate for $\rho \lesssim 4$, but diverges from the MC results for $\rho \gtrsim 4$ values. For the $z_0 = 5$ and 10 results, we see that gKM accurately approximates the MC results. In fact, the gKM results for $z_0 = 10$ are nearly indistinguishable from the MC results. To quantify the error, we have interpolated the numerical results on a uniformly spaced radial grid over the interval $0 < \rho < 10$ with grid spacing $\Delta\rho = 0.1$, and then computed the error made by the gKM approximation relative to the MC results. The minimum and maximum relative errors are given in Table 3.1. The relative errors are quite large for $z_0 = 1$ due to the errors observed for $\rho \gtrsim 4$. As z_0 increases, we see that the relative errors decrease significantly. For the $z_0 = 10$ case, we find that the relative error made by the gKM approximation for $F^-(\rho, 0)$ is less than 14% and for $F^+(\rho, z_0)$ is less than 5%.

Table 3.1: Minimum (MIN) and maximum (MAX) errors made by the gKM approximation relative to MC results for the results shown in Fig. 3.1.

	$F^-(\rho, 0)$		$F^+(\rho, z_0)$	
z_0	MIN	MAX	MIN	MAX
1	0.0033	0.9996	0.0012	0.9999
5	0.0012	0.2778	0.0020	0.2530
10	0.0002	0.1369	0.0005	0.0545

The results shown in Fig. 3.1 demonstrate that the gKM approximation improves as the optical thickness of the medium increases in its approach to the diffusion limit. However,

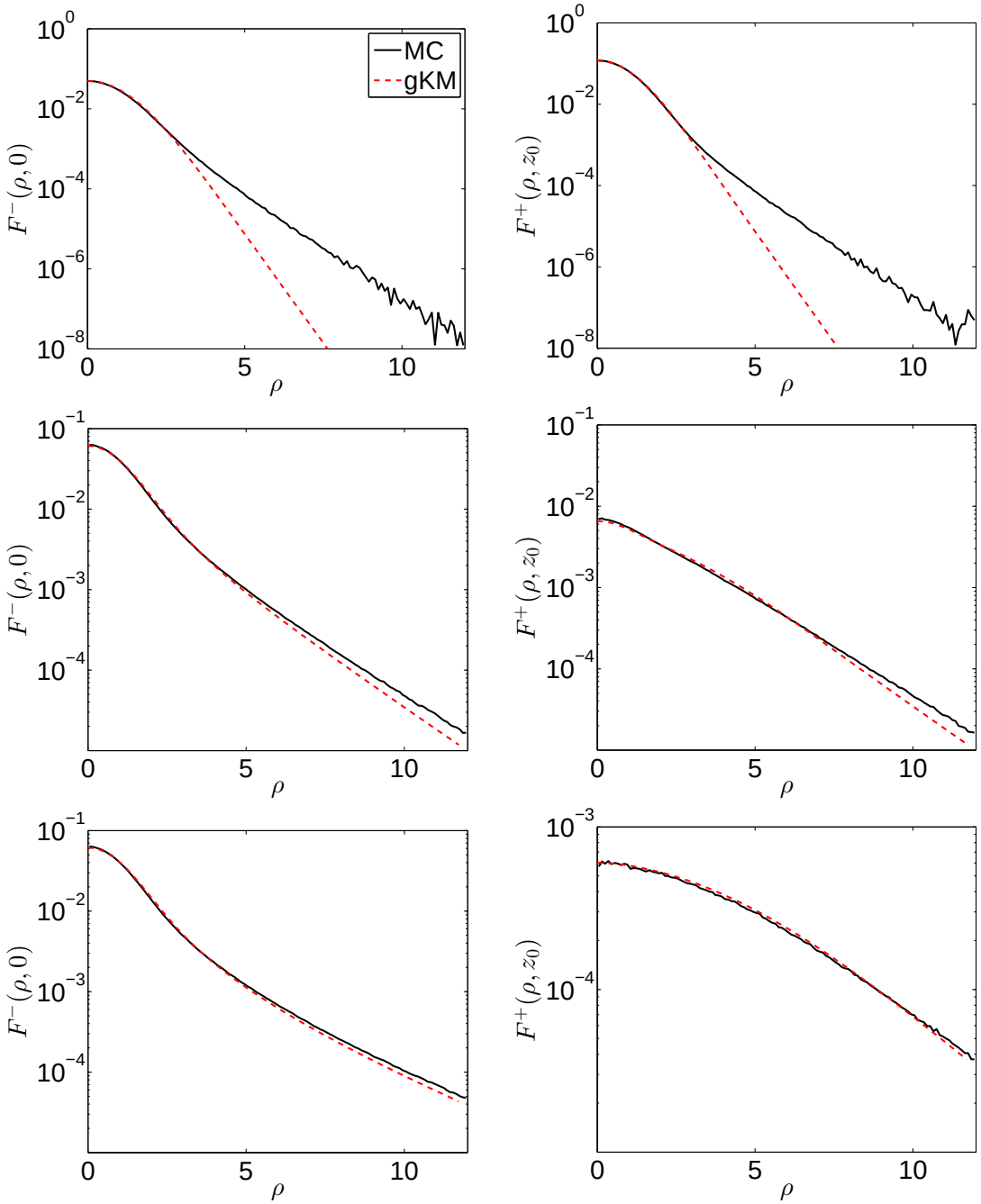

Figure 3.1: Plots of $F^-(\rho,0)$ [left column] and $F^+(\rho,z_0)$ [right column] computed using Monte Carlo (MC) simulations [solid curves] and the generalized Kubelka-Munk (gKM) equations [dashed curves] with $\varpi_0 = 0.99$, $g = 0$, and $z_0 = 1$ [top row], 5, [middle row] and 10 [bottom row].

we observe here the gKM approximation does not correctly capture the transition to the diffusion limit. As a beam penetrates deep into an optically thick medium, it spreads due to multiple scattering and eventually diffuses. The beam governed by the gKM does not spread correctly in the transition to diffusion. This incorrect spread accounts for the error

seen for the $z_0 = 1$ case for $\rho \gtrsim 4$.

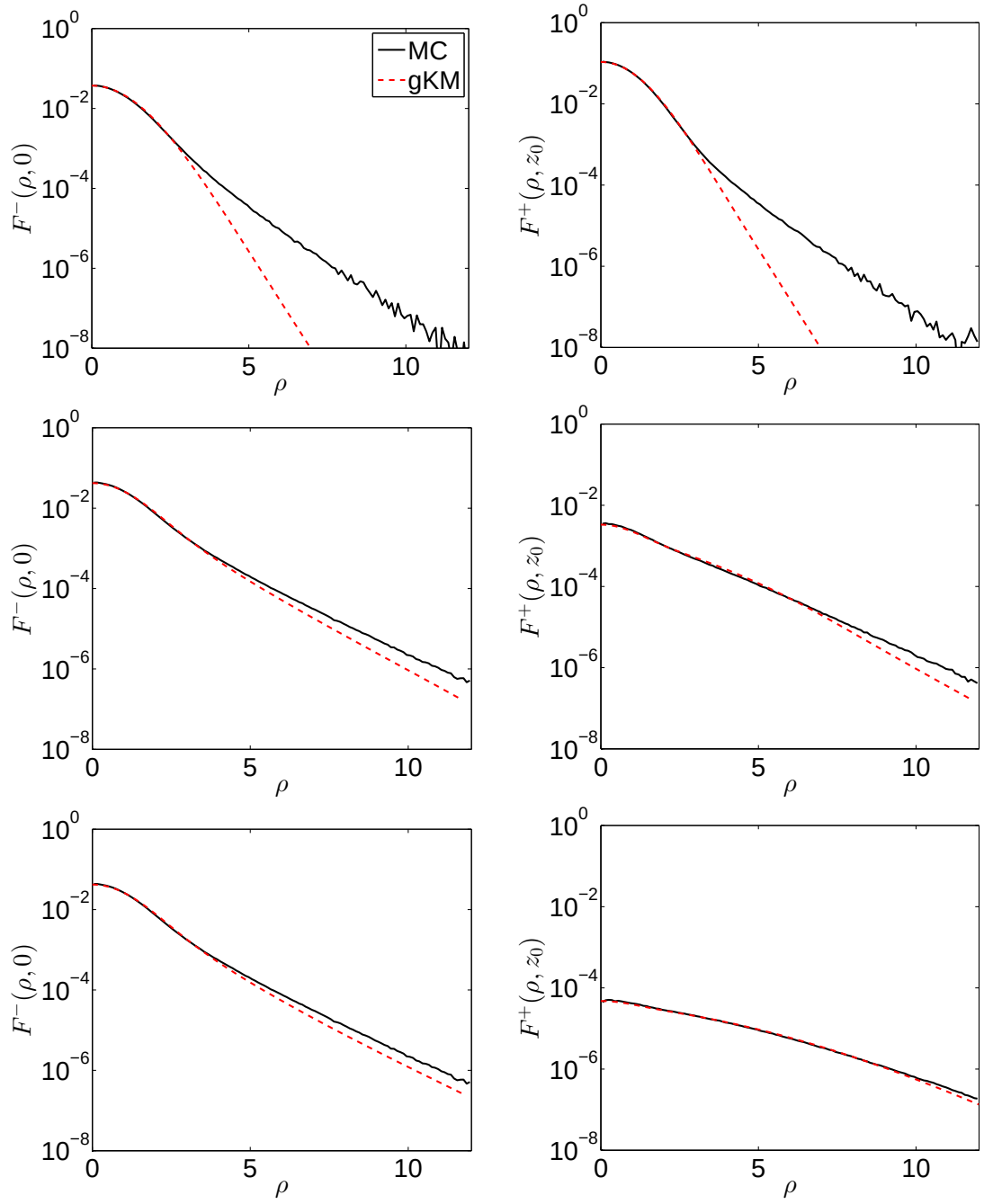

Figure 3.2: Same as Fig. 3.1 except that $\varpi_0 = 0.85$.

In Fig. 3.2 we show results when the medium has more absorption, specifically with $\varpi_0 = 0.85$. We observe in Fig. 3.2 that the gKM approximation is qualitatively accurate in a manner consistent with the results shown in Fig. 3.1. However, there appears to be a larger error introduced for large ρ values. The quantitative errors that the gKM approximation made relative to the MC results are given in Table 3.2. These relative errors show that the gKM approximation is less accurate for this case than the $\varpi_0 = 0.99$ case. In particular, the

maximum relative errors have significantly increased for $z_0 = 5$ and 10 due to the decreased accuracy of the gKM approximation for large ρ values.

Table 3.2: Minimum (MIN) and maximum (MAX) errors made by the gKM approximation relative to MC results for the results shown in Fig. 3.2.

	$F^-(\rho, 0)$		$F^+(\rho, z_0)$	
z_0	MIN	MAX	MIN	MAX
1	0.0015	0.9999	0.0001	1.0006
5	0.0007	0.5755	0.0011	0.5109
10	0.0004	0.4476	0.0014	0.0892

For this problem, $F^+(\rho, z_0) \to 0$ and $F^-(\rho, 0) \to R_\infty(\rho)$ as $z_0 \to \infty$, where $R_\infty(\rho)$ denotes the distribution of power backscattered by the semi-infinite half space, $z > 0$. The gKM approximation appears to capture these limits correctly. Errors made by the gKM approximation are most apparent for the $z_0 = 1$ results. In those results, we find that the gKM approximation does not capture the correct asymptotic behavior as $\rho \to \infty$. The transverse spatial variables, x and y, are coupled to the azimuthal angle, φ, in (3.2.1). Since basis functions Φ_3 and Φ_4, given in (3.2.9c) and (3.2.9d), respectively, only involve $\cos\varphi$ and $\sin\varphi$, the gKM approximation is limited in its ability to take into account high azimuthal angle modes. This, in turn, affects the gKM approximation's ability to take into account steep transverse spatial gradients. The inaccuracy of the gKM approximation in capturing the correct asymptotic behavior for large ρ when $z_0 = 1$ is due to the fact that the gKM approximation is unable to resolve the high space-angle modes that are non-negligible in the true solution. As a consequence to all of this, the beam width, W_0, also plays an important role in the accuracy of this approximation. As $W_0 \to 0$, thereby approaching an infinitesimally narrow pencil beam, the transverse spatial gradient becomes infinitely steep. The gKM approximation will be inaccurate until a sufficient amount of scattering has effectively smoothed those steep transverse spatial gradients. In contrast, the accuracy of the gKM approximation will generally improve for wider beam widths.

3.3.2 Anisotropic scattering

We now consider forward-peaked, anisotropic scattering using the Henyey-Greenstein scattering phase function

$$p = \frac{1}{4\pi} \frac{1 - g^2}{(1 + g^2 - 2g\xi)^{3/2}}, \tag{3.3.2}$$

with

$$\xi = \mu\mu' + \sqrt{1 - \mu^2}\sqrt{1 - \mu'^2}\cos(\varphi - \varphi'). \tag{3.3.3}$$

Here, $-1 \le g \le 1$ denotes the anisotropy factor or mean cosine of the scattering angle. For forward-peaked anisotropic scattering media, $g \sim 1$. To compute the $H^{(1)}$ and $H^{(2)}$ matrices defined in (3.2.16), we have used a product quadrature rule that uses 32-point Gauss-Legendre quadrature rule in μ and a 64-point repeated trapezoid rule in φ.

In Fig. 3.3, we plot the power backscattered, $F^-(\rho, 0)$, [left column] and transmitted, $F^+(\rho, z_0)$, [right column] for a forward-peaked anisotropic scattering medium with $g = 0.85$ and $\varpi_0 = 0.99$ for optical thicknesses $z_0 = 1$ [top row], 5 [middle row], and 10 [bottom row]. The solid curves show the MC results and the dashed curves show the gKM results.

The results show overall that the gKM approximation is much less accurate for

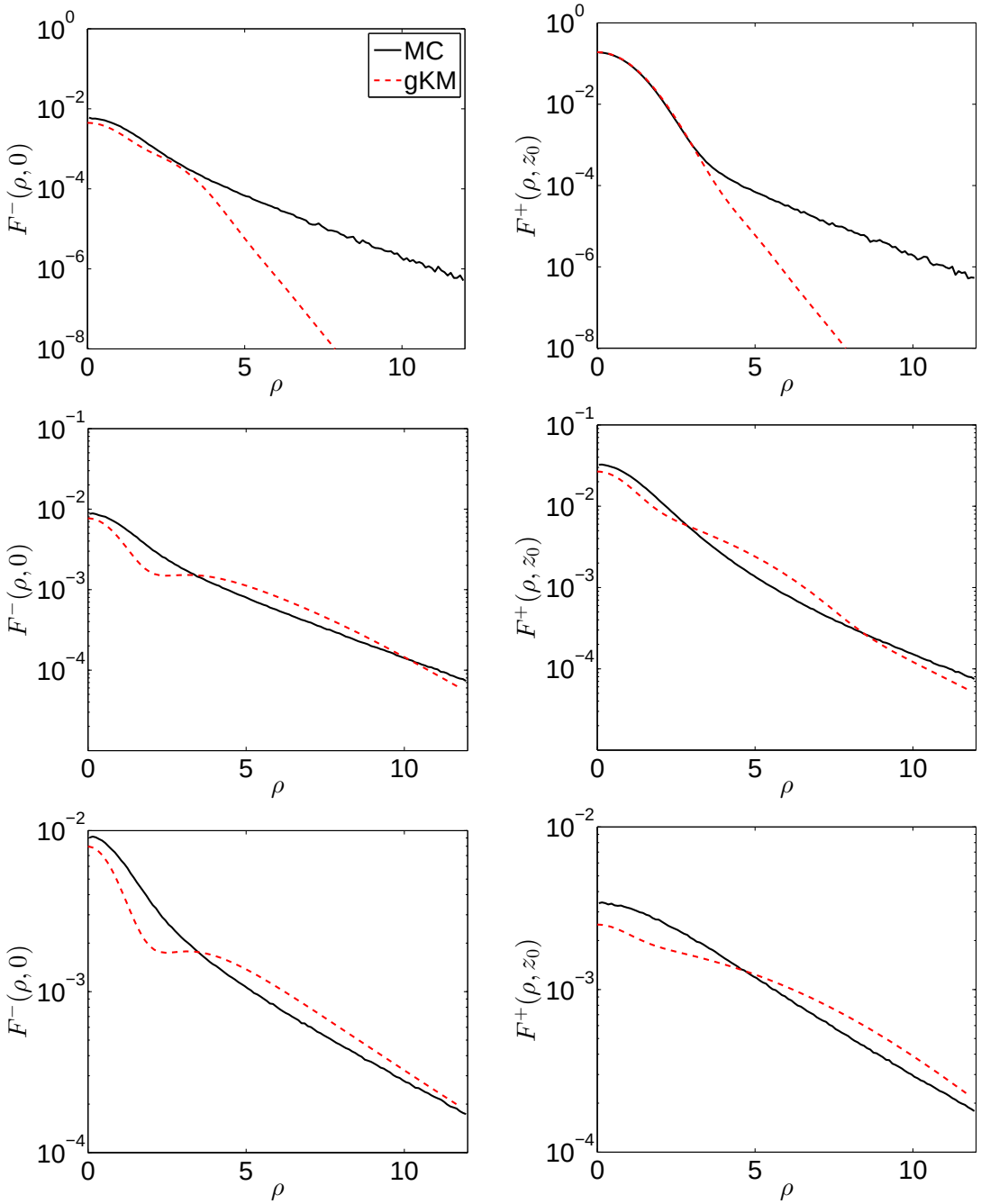

Figure 3.3: Same as Fig. 3.1, except that the medium is composed of a forward-peaked anisotropic scattering medium governed by the Henyey-Greenstein scattering phase function given in (3.3.2) with $g = 0.8$.

anisotropic scattering than for isotropic scattering. Similar to the isotropic scattering results for $z_0 = 1$ shown above, the gKM results shown in Fig. 3.3 show that the gKM approximation does not accurately capture the large ρ behaviors correctly. For $z_0 = 5$ and 10 we observe that the gKM approximation yields results that are at the same order of magnitude as the MC simulation results. However, they are qualitatively different. Table 3.3 gives the

errors made by the gKM approximation relative to the MC results. Those relative errors show that the gKM approximation is doing a poor job for this case. In particular, errors appear in Fig. 3.3 as spurious oscillations in ρ for both $F^-(\rho, 0)$ and $F^+(\rho, z_0)$. In fact, these errors grow monotonically as g increases. For even larger values of g, we have found that the oscillations in the gKM solutions cause negative values which are nonphysical.

Table 3.3: Minimum (MIN) and maximum (MAX) errors made by the gKM approximation relative to MC results for the results shown in Fig. 3.3.

	$F^-(\rho, 0)$		$F^+(\rho, z_0)$	
z_0	MIN	MAX	MIN	MAX
1	0.1400	1.0000	0.0130	1.0001
5	0.0062	0.5069	0.0036	0.8160
10	0.0048	0.4880	0.0014	0.3480

Because the gKM system given in (3.2.19) is just a linear transformation of the DP_1 system given in (3.2.10), the fundamental assumption of the gKM approximation is that (3.2.8) provides an accurate approximation of the forward and backward half-range intensities, $I^{\pm}$. For strong, isotropic scattering, this assumption is accurate and is demonstrated by the agreements seen between the gKM approximation and MC simulation results in Fig. 3.1. For isotropic scattering with moderate absorption, the gKM approximation is less accurate in that this approximation over-damps the decay of $F^+(\rho, z_0)$ to zero as $z_0 \to 0$. When scattering is anisotropically forward-peaked, the angular distribution of the forward and backward half-range intensities, $I^{\pm}$, cannot be accurately approximated by (3.2.8). Consequently, the gKM approximation is less accurate for anisotropic scattering problems. This inaccuracy was shown to be the case for the one dimensional problem [33]. The results shown here demonstrate further that the gKM approximation is limited in its use for forward-peaked anisotropic scattering problems.

3.4 Summary of results

We have systematically extended the gKM approximation to the three-dimensional RTE. The resulting 8×8 system of partial differential equations, resulting from application of the DP_1 method, is much easier to solve than the full RTE. We then specialized this result to axisymmetric problems to study a collimated Gaussian beam incident normally on a plane-parallel slab composed of a uniform absorbing and scattering medium.

By comparing the gKM approximation with results from MC simulations, we demonstrate the effectiveness of this approximation. In particular, we have found that the gKM approximation is accurate for isotropic scattering. The approximation loses some accuracy as the absorption increases, but maintains excellent qualitative agreement. Finally, we have found that the gKM approximation is not accurate for anisotropic, forward-peaked scattering media. In fact, if scattering is too sharply forward-peaked, the gKM approximation yields unphysical results. Overall, the accuracy of the gKM equations is improved as the beam width, W_0, increases.

This extension opens up the ability to consider three-dimensional problems with nonuniform sources in a relatively simple mathematical framework. The key advantage to studying multiple scattering of light using the gKM approximation is that they are substantially easier to solve than the radiative transfer equation. The disadvantage of using

them is that accuracy is limited to isotropic or weakly anisotropic scattering media. Even in those cases, one must take care to consider the relationship between the beam width and the thickness of the medium to ensure that transverse spatial gradients are not too steep for this approximation to be accurate. Because the KM equations have been successfully applied to a broad variety of problems, the advantages of using this extension of the gKM approximation should be very useful in several practical problems.

Chapter 4

Generalized Kubelka-Munk for polarized light

In this chapter, we further explore the extension of the gKM method to polarized light. The previous chapters studied the scalar radiative transfer problem, whereas we require the vector radiative transfer equation (vRTE) for when polarization is considered. As in previous chapters, we seek to apply the double spherical harmonics method of order one, DP_1, to the vRTE and transform the result to obtain the gKM equations for the vectorized problem. Once we have established the gKM equations for this case, we derive the polarized KM coefficients and compare numerical outputs to benchmark results. This is done for Rayleigh scattering for a finite depth slab as well as for larger size scatterers over a semi-infinite slab.

4.1 Vector radiative transfer equation

We have derived the generalized Kubelka-Munk equations for the scalar, or unpolarized, case for radiative transfer. If light is polarized, it may be expressed via Stokes parameters in the form of the Stokes vector $\mathbf{I}(\mu, \varphi, z) = [I, Q, U, V]^T$. Here, I is the specific intensity, which is what we have been studying for the scalar case done prior, Q and U represent the linear polarizations, and V is the circular polarization. This Stokes vector satisfies the one dimensional vector radiative transfer equation

$$\mu \frac{\partial}{\partial z}\mathbf{I}(\mu, \varphi, z) + \mathbf{I}(\mu, \varphi, z) = \varpi_0 \int_0^{2\pi} \int_{-1}^{1} \mathbf{Z}(\mu, \mu', \varphi - \varphi')\mathbf{I}(\mu', \varphi', z)\ d\mu'\ d\varphi' + \mathbf{Q}(\mu, \varphi, z), \tag{4.1.1}$$

over the slab $0 \leq z \leq z_1$. We define $\mathbf{Z}(\mu, \mu', \varphi - \varphi')$ as the 4×4 scattering matrix, and $\mathbf{Q}(\mu, \varphi, z)$ is a source. We also impose the boundary conditions

$$\mathbf{I}(\mu, \varphi, 0) = \mathbf{f}^+(\mu, \varphi), \qquad 0 < \mu \leq 1, \tag{4.1.2a}$$

$$\mathbf{I}(\mu, \varphi, z_1) = \mathbf{f}^-(\mu, \varphi), \qquad -1 \leq \mu < 0. \tag{4.1.2b}$$

with $\mathbf{f}^{\pm} = [\mathbf{f}^{\pm}_{\mathscr{I}}, \mathbf{f}^{\pm}_{\mathscr{Q}}, \mathbf{f}^{\pm}_{\mathscr{U}}, \mathbf{f}^{\pm}_{\mathscr{V}}]^T$.

4.2 Polarized gKM equations

We make the usual definition $\mathbf{I}^{\pm}(\mu,\varphi,z)=\mathbf{I}(\pm\mu,\varphi,z)$ over $0<\mu\leq 1$, and we expand over the gKM basis, $\{\Phi_j(\mu,\varphi)\}$, $j=1,\ldots,4$, defined in (3.2.9), as

$$\mathbf{I}^{\pm}(\mu,\varphi,z)=\sum_{j=1}^{4}\mathbf{c}_j^{\pm}(z)\Phi_j(\mu,\varphi). \tag{4.2.1}$$

Here, we have written $\mathbf{c}_j^{\pm}(z)=[\mathscr{I}_j^{\pm}(z),\mathscr{Q}_j^{\pm}(z),\mathscr{U}_j^{\pm}(z),\mathscr{V}_j^{\pm}(z)]^T$, with entries denoting coefficients for I,Q,U, and V, respectively. Substituting (4.2.1) into (4.1.1) yields

$$\begin{aligned}\sum_{j=1}^{4}\Bigg\{\pm\mu\Phi_j\left(\mathbf{c}_j^{\pm}\right)'=-\Phi_j\mathbf{c}_j^{\pm}+\varpi_0\int_0^{2\pi}\int_0^1\mathbf{Z}(\pm\mu,\mu',\varphi-\varphi')\Phi_j(\mu',\varphi',z)\;d\mu'\;d\varphi'\mathbf{c}_j^{+}\\ +\varpi_0\int_0^{2\pi}\int_0^1\mathbf{Z}(\pm\mu,-\mu',\varphi-\varphi')\Phi_j(\mu',\varphi',z)\;d\mu'\;d\varphi'\mathbf{c}_j^{-}\Bigg\}+\mathbf{Q}(\pm\mu,\varphi,z)\end{aligned} \tag{4.2.2}$$

Multiplying (4.2.2) by Φ_k and integrating with respect to μ and φ, we obtain

$$\begin{aligned}\sum_{j=1}^{4}\Bigg\{\pm(\Phi_k,\mu\Phi_j)\left(\mathbf{c}_j^{\pm}\right)'=-(\Phi_k,\Phi_j)\mathbf{c}_j^{\pm}+\varpi_0(\Phi_k,\mathbf{P}_{1,j})\mathbf{c}_j^{+}\\ +\varpi_0(\Phi_k,\mathbf{P}_{2,j})\mathbf{c}_j^{-}\Bigg\}+(\Phi_k,\mathbf{Q}^{\pm}),\end{aligned} \tag{4.2.3}$$

where we have notated

$$\mathbf{P}_{1,j}=\int_0^{2\pi}\int_0^1\mathbf{Z}(\pm\mu,\mu',\varphi-\varphi')\Phi_j(\mu',\varphi',z)\;d\mu'\;d\varphi' \tag{4.2.4a}$$

$$\text{and}\quad\mathbf{P}_{2,j}=\int_0^{2\pi}\int_0^1\mathbf{Z}(\pm\mu,-\mu',\varphi-\varphi')\Phi_j(\mu',\varphi',z)\;d\mu'\;d\varphi', \tag{4.2.4b}$$

and $(f,g)=\int_0^{2\pi}\int_0^1 f(\mu,\varphi)g(\mu,\varphi)\;d\mu d\varphi$. Now, let us define $\mathbf{w}^{\pm}=[\vec{\mathscr{I}}^{\pm},\vec{\mathscr{Q}}^{\pm},\vec{\mathscr{U}}^{\pm},\vec{\mathscr{V}}^{\pm}]^T$, where each component vector is the vector of those coefficients, i.e. $\vec{\mathscr{I}}^{\pm}=[\mathscr{I}_j^{\pm}]$, $j=1,\ldots,4$. Recall that $\mathbf{A}=[A_{nm}]=(\Phi_n,\mu\Phi_m)$, and let us further define $\mathbf{Z}_1=[(\Phi_k,\mathbf{P}_{1,j}^{+})]$, $\mathbf{Z}_2=[(\Phi_k,\mathbf{P}_{1,j}^{-})]$, $\mathbf{Z}_3=[(\Phi_k,\mathbf{P}_{2,j}^{+})]$, and $\mathbf{Z}_4=[(\Phi_k,\mathbf{P}_{2,j}^{-})]$. Now, we rewrite (4.2.3) in matrix form as

$$\begin{aligned}\begin{bmatrix}\mathbf{A}_B & \mathbf{0}\\ \mathbf{0} & -\mathbf{A}_B\end{bmatrix}\begin{bmatrix}\mathbf{w}^{+}\\ \mathbf{w}^{-}\end{bmatrix}'&=-\begin{bmatrix}\mathbf{w}^{+}\\ \mathbf{w}^{-}\end{bmatrix}+\varpi_0\begin{bmatrix}\mathbf{Z}_1 & \mathbf{Z}_2\\ \mathbf{Z}_3 & \mathbf{Z}_4\end{bmatrix}\begin{bmatrix}\mathbf{w}^{+}\\ \mathbf{w}^{-}\end{bmatrix}+\begin{bmatrix}\mathbf{\Gamma}^{+}\\ \mathbf{\Gamma}^{-}\end{bmatrix}\\ &=\begin{bmatrix}-\mathbb{I}+\varpi_0\mathbf{Z}_1 & \varpi_0\mathbf{Z}_2\\ \varpi_0\mathbf{Z}_3 & -\mathbb{I}+\varpi_0\mathbf{Z}_4\end{bmatrix}\begin{bmatrix}\mathbf{w}^{+}\\ \mathbf{w}^{-}\end{bmatrix}+\begin{bmatrix}\mathbf{\Gamma}^{+}\\ \mathbf{\Gamma}^{-}\end{bmatrix}.\end{aligned} \tag{4.2.5}$$

Here we have defined, for simplicity, $\mathbf{A}_B = \text{diag}(\mathbf{A}, \mathbf{A}, \mathbf{A}, \mathbf{A})$ and $\mathbf{\Gamma}^{\pm} = (\Phi_k, \mathbf{Q}^{\pm})$. The boundary conditions, projected onto the basis functions are given by

$$\mathbf{w}^{+}(0) = \begin{bmatrix} (\Phi_k, \mathbf{f}^{+}_{\mathscr{I}}) \\ (\Phi_k, \mathbf{f}^{+}_{\mathscr{Q}}) \\ (\Phi_k, \mathbf{f}^{+}_{\mathscr{U}}) \\ (\Phi_k, \mathbf{f}_{\mathscr{V}}) \end{bmatrix}, \tag{4.2.6a}$$

$$\mathbf{w}^{-}(z_1) = \begin{bmatrix} (\Phi_k, \mathbf{f}^{-}_{\mathscr{I}}) \\ (\Phi_k, \mathbf{f}^{-}_{\mathscr{Q}}) \\ (\Phi_k, \mathbf{f}^{-}_{\mathscr{U}}) \\ (\Phi_k, \mathbf{f}^{-}_{\mathscr{V}}) \end{bmatrix}. \tag{4.2.6b}$$

As we have done in previous chapters, we make the linear transform $\mathbf{y}^{\pm} = \sqrt{2\pi}\mathbf{A_B}\mathbf{w}^{\pm}$. With this, (4.2.5) becomes

$$\begin{bmatrix} \mathbb{I} & \mathbf{0} \\ \mathbf{0} & -\mathbb{I} \end{bmatrix} \begin{bmatrix} \mathbf{y}^{+} \\ \mathbf{y}^{-} \end{bmatrix}' = \begin{bmatrix} \tilde{\mathbf{S}}_1 & \tilde{\mathbf{S}}_2 \\ \tilde{\mathbf{S}}_3 & \tilde{\mathbf{S}}_4 \end{bmatrix} \begin{bmatrix} \mathbf{y}^{+} \\ \mathbf{y}^{-} \end{bmatrix} + \sqrt{2\pi} \begin{bmatrix} \mathbf{\Gamma}^{+} \\ \mathbf{\Gamma}^{-} \end{bmatrix}, \tag{4.2.7}$$

where $\tilde{\mathbf{S}}_{1,4} = (-\mathbb{I} + \varpi_0 \mathbf{Z}_{1,4})\,\mathbf{A}_B^{-1}$ and $\tilde{\mathbf{S}}_{2,3} = \varpi_0 \mathbf{Z}_{2,3}\mathbf{A}_B^{-1}$. The system given by (4.2.7) are the polarized gKM equations, subject to the transformed boundary conditions

$$\mathbf{y}^{+}(0) = \sqrt{2\pi}\mathbf{A}_B\mathbf{w}^{+}(0), \tag{4.2.8a}$$

$$\mathbf{y}^{-}(z_1) = \sqrt{2\pi}\mathbf{A}_B\mathbf{w}^{-}(z_1), \tag{4.2.8b}$$

We write the Stokes vector now, as before, as the sum of the diffuse and reduced intensities, $\mathbf{I} = \mathbf{I}_d + \mathbf{I}_{ri}$. Here, $\mathbf{I}_{ri}$ satisfies the homogeneous boundary value problem

$$\mu \frac{\partial}{\partial z}\mathbf{I}_{ri}(\mu, \varphi, z) + \mathbf{I}_{ri}(\mu, \varphi, z) = \mathbf{0}, \tag{4.2.9a}$$

$$\text{subject to} \quad \mathbf{I}_{ri}(\mu, \varphi, 0) = \mathbf{Q}_0 \delta(\mu - \mu_0)\delta(\varphi - \varphi_0), \quad 0 < \mu \leq 1, \tag{4.2.9b}$$

$$\mathbf{I}_{ri}(\mu, \varphi, z_1) = \mathbf{0}, \quad -1 \leq \mu < 0, \tag{4.2.9c}$$

with $\mathbf{Q}_0$ denoting the polarization state of the incident light. The solution is $\mathbf{I}_{ri}(\mu, \varphi, z) = \mathbf{Q}_0 \delta(\mu - \mu_0)\delta(\varphi - \varphi_0)e^{-z/\mu}$. Substituting $\mathbf{I} = \mathbf{I}_d + \mathbf{I}_{ri}$ into (4.1.1), we find that I_d satisfies (4.1.1) subject to boundary conditions (4.1.2) with

$$\begin{aligned} \mathbf{Q}^{\pm} &= \varpi_0 \int_{-\pi}^{\pi} \int_{-1}^{1} \mathbf{Z}(\pm\mu, \mu', \varphi - \varphi')\mathbf{Q}_0 \delta(\mu - \mu_0)\delta(\varphi - \varphi_0)e^{-z/\mu'}\, d\mu'\, d\varphi', \\ &= \varpi_0 \mathbf{Z}(\pm\mu, \mu_0, \varphi - \varphi_0)\mathbf{Q}_0 e^{-z/\mu_0}. \end{aligned} \tag{4.2.10}$$

To solve this boundary value problem, we use the generalized eigenvalue problem below to solve (4.1.1) for $\mathbf{I}_d$ with zero boundary conditions.

$$\lambda \begin{bmatrix} \mathbb{I} & \mathbf{0} \\ \mathbf{0} & -\mathbb{I} \end{bmatrix} \begin{bmatrix} \mathbf{u} \\ \mathbf{v} \end{bmatrix} = \begin{bmatrix} \tilde{\mathbf{Z}}_1 & \tilde{\mathbf{Z}}_2 \\ \tilde{\mathbf{Z}}_3 & \tilde{\mathbf{Z}}_4 \end{bmatrix} \begin{bmatrix} \mathbf{u} \\ \mathbf{v} \end{bmatrix}. \tag{4.2.11}$$

Setting $\mathbf{y} = \mathbf{y}_h + \mathbf{y}_p$, with

$$\mathbf{y}_h = \sum_{j=1}^{16} \left(a_j \begin{bmatrix} \mathbf{u}_j \\ \mathbf{v}_j \end{bmatrix} e^{\lambda_j (z - z_1)} + b_j \begin{bmatrix} \mathbf{v}_j \\ \mathbf{u}_j \end{bmatrix} e^{-\lambda_j z} \right) \tag{4.2.12}$$

satisfying (4.2.11), where $\lambda_{-j} = -\lambda_j$, and assuming that $\mathbf{y}_p = \boldsymbol{\eta} e^{-z/\mu_0}$, we find that $\boldsymbol{\eta}$ must satisfy

$$\begin{bmatrix} -\mathbb{I} - \tilde{\mathbf{Z}}_1 & -\tilde{\mathbf{Z}}_2 \\ -\tilde{\mathbf{Z}}_3 & \mathbb{I} - \tilde{\mathbf{Z}}_4 \end{bmatrix} \begin{bmatrix} \boldsymbol{\eta}^+ \\ \boldsymbol{\eta}^- \end{bmatrix} = \sqrt{2\pi} \begin{bmatrix} \Gamma^+ \\ \Gamma^- \end{bmatrix}. \tag{4.2.13}$$

We write the general solution as

$$\mathbf{y} = \sum_{j=1}^{16} \left(a_j \begin{bmatrix} \mathbf{u}_j \\ \mathbf{v}_j \end{bmatrix} e^{\lambda_j (z - z_1)} + b_j \begin{bmatrix} \mathbf{v}_j \\ \mathbf{u}_j \end{bmatrix} e^{-\lambda_j z} \right) + \boldsymbol{\eta} e^{-z/\mu_0}. \tag{4.2.14}$$

To determine the coefficients a_j and b_j, we apply boundary conditions (4.2.8), resulting in the system of equations

$$\sum_{j=1}^{16} \left(a_j \mathbf{u}_j e^{-\lambda_j z_1} + b_j \mathbf{v}_j \right) = \mathbf{y}^+(0) - \boldsymbol{\eta}^+, \tag{4.2.15a}$$

$$\sum_{j=1}^{16} \left(a_j \mathbf{v}_j + b_j \mathbf{u}_j e^{-\lambda_j z_1} \right) = \mathbf{y}^+(z_1) - \boldsymbol{\eta}^- e^{-z_1/\mu_0}, \tag{4.2.15b}$$

which we solve numerically.

4.3 Deriving the polarized KM equations

We derive the KM equations for polarized light, and as with our study in Chapter 2, we consider the case when $\mu_a = 0$, i.e. $\varpi_0 = 1$. Here the vRTE is solved by a constant vector solution, and hence has a zero eigenvalue. (4.2.11) yields

$$\begin{bmatrix} -\mathbb{I} + \tilde{\mathbf{Z}}_1 & \tilde{\mathbf{Z}}_2 \\ \tilde{\mathbf{Z}}_3 & \mathbb{I} + \tilde{\mathbf{Z}}_4 \end{bmatrix} \begin{bmatrix} \mathbf{u} \\ \mathbf{v} \end{bmatrix} = \mathbf{0}, \tag{4.3.1}$$

which when coupled with the normalization of $\mathbf{Z}$, i.e. $\frac{1}{4\pi} \iint_\Omega \mathbf{Z} \, d\Omega = \mathbb{I}$, yields that $\mathbf{Z}_1 \hat{\mathbf{e}}_1^B + \mathbf{Z}_2 \hat{\mathbf{e}}_1^B = \hat{\mathbf{e}}_1^B$ and $\mathbf{Z}_3 \hat{\mathbf{e}}_1^B + \mathbf{Z}_4 \hat{\mathbf{e}}_1^B = \hat{\mathbf{e}}_1^B$. Here we define $\hat{\mathbf{e}}_1^B = [\hat{\mathbf{e}}_1, \hat{\mathbf{e}}_1, \hat{\mathbf{e}}_1, \hat{\mathbf{e}}_1]^T$, and, hence, for $\lambda = 0$,

$$\begin{bmatrix} \mathbf{u}_0 \\ \mathbf{v_0} \end{bmatrix} = \begin{bmatrix} \hat{\mathbf{e}}_1^B \\ \hat{\mathbf{e}}_1^B \end{bmatrix} \tag{4.3.2}$$

As before, we perturb from this zero eigenvalue, quantifying it by setting $\varpi_0 = 1 - \epsilon^2$, $\epsilon \ll 1$. (4.2.11) becomes

$$\lambda \begin{bmatrix} \mathbf{A}_B & \mathbf{0} \\ \mathbf{0} & -\mathbf{A}_B \end{bmatrix} \begin{bmatrix} \mathbf{u} \\ \mathbf{v} \end{bmatrix} + \epsilon^2 \begin{bmatrix} \mathbf{Z}_1 & \mathbf{Z}_2 \\ \mathbf{Z}_3 & \mathbf{Z}_4 \end{bmatrix} \begin{bmatrix} \mathbf{u} \\ \mathbf{v} \end{bmatrix} = \begin{bmatrix} \mathbf{Z}_1 - \mathbb{I} & \mathbf{Z}_2 \\ \mathbf{Z}_3 & \mathbf{Z}_4 - \mathbb{I} \end{bmatrix} \begin{bmatrix} \mathbf{u} \\ \mathbf{v} \end{bmatrix}. \tag{4.3.3}$$

We expand $\lambda_1 = \epsilon\lambda_1' + \epsilon^2\lambda_1'' + O(\epsilon^3)$ and

$$\begin{bmatrix}\mathbf{u}_1\\ \mathbf{v}_1\end{bmatrix} = \begin{bmatrix}\hat{\mathbf{e}}_1^B\\ \hat{\mathbf{e}}_1^B\end{bmatrix} + \epsilon\begin{bmatrix}\mathbf{u}_1'\\ \mathbf{v}_1'\end{bmatrix} + \epsilon^2\begin{bmatrix}\mathbf{u}_1''\\ \mathbf{v}_1''\end{bmatrix} + O(\epsilon^3), \tag{4.3.4}$$

and (4.3.3) becomes, to $O(\epsilon)$,

$$\lambda_1'\begin{bmatrix}\mathbf{A}_B & \mathbf{0}\\ \mathbf{0} & -\mathbf{A}_B\end{bmatrix}\begin{bmatrix}\hat{\mathbf{e}}_1^B\\ \hat{\mathbf{e}}_1^B\end{bmatrix} = \begin{bmatrix}\mathbf{Z}_1 - \mathbb{I} & \mathbf{Z}_2\\ \mathbf{Z}_3 & \mathbf{Z}_4 - \mathbb{I}\end{bmatrix}\begin{bmatrix}\mathbf{u}_1'\\ \mathbf{v}_1'\end{bmatrix} \tag{4.3.5}$$

We again recognize the left-hand side as the projection onto μ, which is an eigenfunction of the scattering matrix [42]. This once more yields

$$\begin{bmatrix}\mathbf{u}_1'\\ \mathbf{v}_1'\end{bmatrix} = -\frac{\lambda_1'}{1-g}\begin{bmatrix}\mathbf{m}_1\\ -\mathbf{m}_1\end{bmatrix}, \tag{4.3.6}$$

with $\mathbf{m}_1 = \mathbf{A}_B\hat{\mathbf{e}}_1^B$. Now, to $O(\epsilon^2)$, (4.3.3) becomes

$$\lambda_1''\begin{bmatrix}\mathbf{A}_B & \mathbf{0}\\ \mathbf{0} & -\mathbf{A}_B\end{bmatrix}\begin{bmatrix}\hat{\mathbf{e}}_1^B\\ \hat{\mathbf{e}}_1^B\end{bmatrix} + \lambda_1'\begin{bmatrix}\mathbf{A}_B & \mathbf{0}\\ \mathbf{0} & -\mathbf{A}_B\end{bmatrix}\begin{bmatrix}\mathbf{u}_1'\\ \mathbf{v}_1'\end{bmatrix} + \begin{bmatrix}\mathbf{Z}_1 & \mathbf{Z}_2\\ \mathbf{Z}_3 & \mathbf{Z}_4\end{bmatrix}\begin{bmatrix}\hat{\mathbf{e}}_1^B\\ \hat{\mathbf{e}}_1^B\end{bmatrix} = \begin{bmatrix}\mathbf{Z}_1 - \mathbb{I} & \mathbf{Z}_2\\ \mathbf{Z}_3 & \mathbf{Z}_4 - \mathbb{I}\end{bmatrix}\begin{bmatrix}\mathbf{u}_1''\\ \mathbf{v}_1''\end{bmatrix}, \tag{4.3.7}$$

which when projected on $[\hat{\mathbf{e}}_1^B, \hat{\mathbf{e}}_1^B]$ yields $\lambda_1' = \sqrt{3(1-g)}$ as before. This gives us the familiar result of

$$\begin{bmatrix}\mathbf{u}_1\\ \mathbf{v}_1\end{bmatrix} = \begin{bmatrix}\hat{\mathbf{e}}_1^B\\ \hat{\mathbf{e}}_1^B\end{bmatrix} + \epsilon\sqrt{3/(1-g)}\begin{bmatrix}-\mathbf{m}_1\\ \mathbf{m}_1\end{bmatrix} + O(\epsilon^2) \tag{4.3.8}$$

As with the scalar case, we find this satisfies the system of differential equations for the flux,

$$\frac{d}{dz}\begin{bmatrix}\mathbf{F}^+\\ \mathbf{F}^-\end{bmatrix} = \tilde{\mathbf{U}}\mathbf{L}\tilde{\mathbf{U}}^{-1}\begin{bmatrix}\mathbf{F}^+\\ \mathbf{F}^-\end{bmatrix}, \tag{4.3.9}$$

with $\tilde{u} = 1/2 - \epsilon/\sqrt{3(1-g)}$, $\tilde{v} = 1/2 + \epsilon/\sqrt{3(1-g)}$, and

$$\tilde{\mathbf{U}} = \begin{bmatrix}\tilde{u} & \tilde{v} & 0 & 0 & 0 & 0 & 0 & 0\\ 0 & 0 & \tilde{u} & \tilde{v} & 0 & 0 & 0 & 0\\ 0 & 0 & 0 & 0 & \tilde{u} & \tilde{v} & 0 & 0\\ 0 & 0 & 0 & 0 & 0 & 0 & \tilde{u} & \tilde{v}\\ \tilde{v} & \tilde{u} & 0 & 0 & 0 & 0 & 0 & 0\\ 0 & 0 & \tilde{v} & \tilde{u} & 0 & 0 & 0 & 0\\ 0 & 0 & 0 & 0 & \tilde{v} & \tilde{u} & 0 & 0\\ 0 & 0 & 0 & 0 & 0 & 0 & \tilde{v} & \tilde{u}\end{bmatrix}, \tag{4.3.10a}$$

$$\mathbf{L} = \begin{bmatrix}\lambda_1 & 0 & 0 & 0 & 0 & 0 & 0 & 0\\ 0 & -\lambda_1 & 0 & 0 & 0 & 0 & 0 & 0\\ 0 & 0 & \lambda_1 & 0 & 0 & 0 & 0 & 0\\ 0 & 0 & 0 & -\lambda_1 & 0 & 0 & 0 & 0\\ 0 & 0 & 0 & 0 & \lambda_1 & 0 & 0 & 0\\ 0 & 0 & 0 & 0 & 0 & -\lambda_1 & 0 & 0\\ 0 & 0 & 0 & 0 & 0 & 0 & \lambda_1 & 0\\ 0 & 0 & 0 & 0 & 0 & 0 & 0 & -\lambda_1\end{bmatrix}. \tag{4.3.10b}$$

We may write this in a more familiar form, which we call the polarized Kubelka-Munk equations,

$$\frac{d}{dz}\mathbf{F}^+ = -(K+S)\mathbf{F}^+ + S\mathbf{F}^-, \tag{4.3.11a}$$

$$\frac{d}{dz}\mathbf{F}^- = -S\mathbf{F}^+ + (K+S)\mathbf{F}^-, \tag{4.3.11b}$$

with $S = \frac{3}{4}(1-g) - (1-\varpi_0)$ and $K = 2(1-\varpi_0)$. As before this gives the same result as the scalar case,

$$\tilde{K} = (\mu_s + \mu_a)K = 2\mu_a, \tag{4.3.12a}$$

$$\tilde{S} = (\mu_s + \mu_a)S = \frac{3}{4}\mu_s(1-g) - \frac{1}{4}\mu_a(1-3g). \tag{4.3.12b}$$

4.4 Numerical Results

The scattering operator for spherical particles, given by (A.1.1), is derived from Mie scattering theory [44]. It is described using the set of "scattering" constants, (A.1.5), for each of the Fourier modes in $\varphi - \varphi'$. In this section, we evaluate the accuracy of the polarized gKM equations, (4.2.7), for various sizes of the spherical scatterers that constitute the medium. We also seek to analyze their performance for non-normally incident boundary sources, i.e. for $0 < \mu_0 < 1$.

Rayleigh scattering corresponds to the case when the wavelength of the incident source is much larger than the size of the scattering particles within the medium. We may use (A.4.6) to compute the scattering operator in (4.2.5) for increased speed and less storage. Here we choose the depolarization ratio, ρ, to be zero, and we have the boundary source to be normally incident to the slab, i.e. $\mu_0 = 1$.

We proceed by computing and comparing ratios for the cross-polarization discriminant and circular polarization for the flux, $p_l(z)$ and $p_c(z)$, respectively, defined as

$$p_l(z) = \frac{F_I(z) + F_Q(z)}{F_I(z) - F_Q(z)} \tag{4.4.1a}$$

$$p_c(z) = F_V(z)/F_I(z), \tag{4.4.1b}$$

where $\mathbf{F}(z) = [F_I(z), F_Q(z), F_U(z), F_V(z)]^T$ is the Stokes vector for the flux.

For an unpolarized source, we have the amplitude vector for the source term given by $\mathbf{Q}_0 = [1,0,0,0]^T$ in (4.2.9). Figure 4.1 shows the results of applying the polarized gKM equations to this unpolarized source, and we compare them to a discrete ordinate solution of the vector transport equation (4.1.1). For a slab of thickness $z_1 = 25.0$ with an albedo of $\varpi_0 = 0.99$, we show the linear polarization ratio (top) and the circular polarization ratio (bottom). We see that as the solutions decay toward zero (left column), small errors are magnified in the relative error computations (right column). These manifest for the deeper portions of the slab, with the largest error occurring in a boundary layer about the far boundary of the slab. This is due to the zero boundary condition imposed at the end of the slab causing near zero denominators in (4.4.1). We report only the absolute error for p_c, as the solution in this case is identically zero. Qualitatively, gKM captures the behavior of the solution's decay quite well.

Figure 4.2 shows the same situation as Fig. 4.1 but with a polarized source, $\mathbf{Q}_0 =$

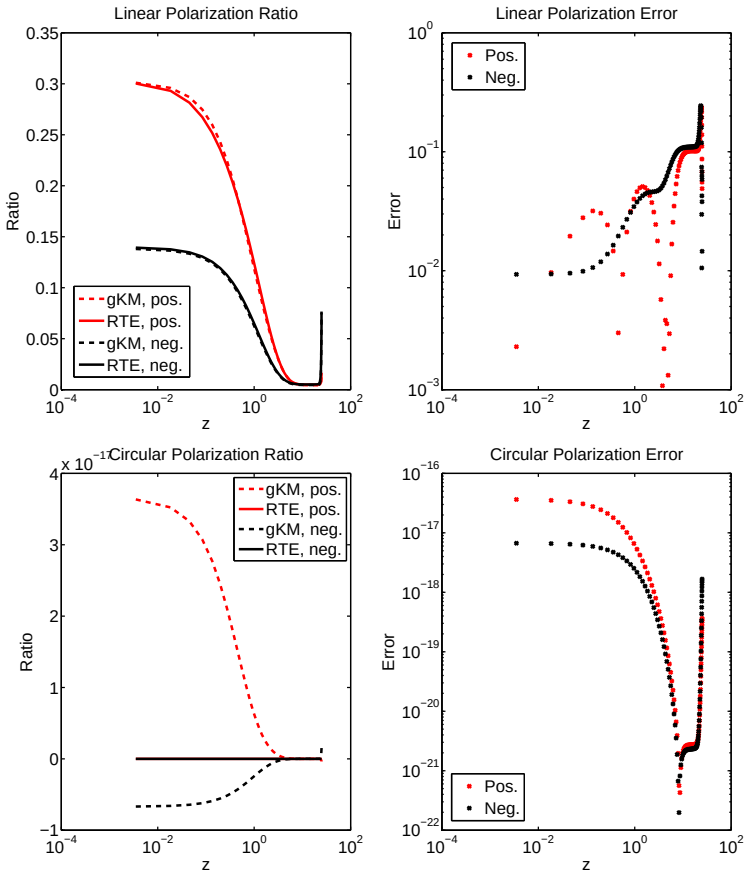

Figure 4.1: Here we show (left column) comparisons of $p_l(z)$ (top) and $p_c(z)$ (bottom) computed from solutions of boundary value problem consisting of (4.1.1) and (4.1.2), using (4.4.1) for the forward (red) and backward (black) fluxes. Here, $z_1 = 25$ and $\varpi_0 = 0.99$ with an unpolarized source, i.e. $\mathbf{Q}_0 = [1, 0, 0, 0]^T$ in (4.2.9), and zero boundary conditions. The right column shows the relative error for each, computed across the slab.

$[2, 1, 0, 1]^T$. As with the unpolarized case, the gKM approximation qualitatively captures the behavior of the solutions, though the relative error increases, as before, as the solutions decay to zero.

It is apparent that the gKM system for polarized light normally incident on the slab provides a good approximation for Rayleigh scattering, when the incident wavelength is much larger than the scattering particles of the slab. This is due to small number of Fourier modes associated with the Rayleigh scattering matrix (see Appendix A.4), as it depends solely on modes $l = 0, 1$, and 2. For $l = 0$, we simply have the scalar case, and we have demonstrated that gKM is a good approximation in this regime. When $l = 1$, we introduce the first dependence on $\varphi - \varphi'$, which is accommodated by the basis functions $\Phi_3(\mu, \varphi)$ and $\Phi_4(\mu, \varphi)$ in (3.2.9c) and (3.2.9d), respectively. Despite not including a basis function explicitly for the terms including $\cos 2(\varphi - \varphi')$ and $\sin 2(\varphi - \varphi')$, i.e. when $l = 2$, we find that gKM maintains good agreement with solutions of the vRTE for this type of scattering.

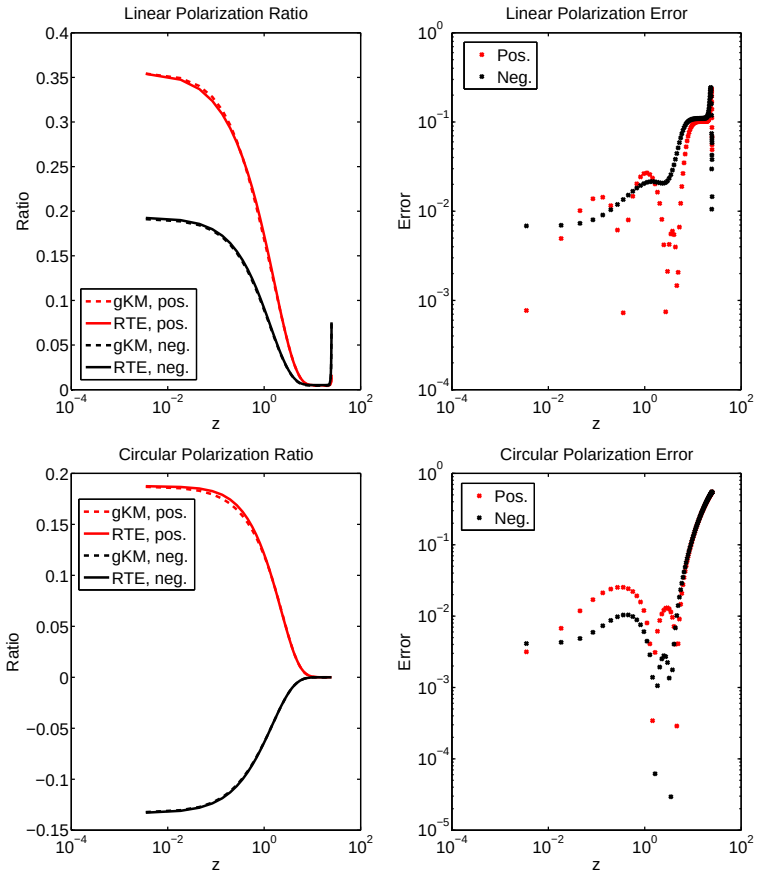

Figure 4.2: Same as Fig. 4.1 but with $\mathbf{Q}_0 = [2, 1, 0, 1]^T$.

4.5 Summary of results

In this chapter, we have derived the gKM equations for a polarized source, incident normally on a slab governed by Rayleigh scattering. We apply the DP_1 approximation for each of the components of the Stokes vector and transform them to create the 16×16 polarized gKM system. The resulting boundary value problem is then solved numerically and the values of the linear cross-polarization discriminant, $p_l(z)$, and the circular polarization ratio, p_c, were compared to those computed using the discrete ordinate method.

We find that the polarized gKM approximation performs with nearly the same level of accuracy as the scalar case. It is clear that the ratio p_l is approximated well across the slab. We also so from the results for p_c for a polarized source that the exclusion of higher Fourier modes in the gKM solutions hinders the accuracy of the model. Despite this, it clearly captures the qualitative behavior of this more complex scenario across the slab, only diminishing in accuracy for very thin slabs while modeling the diffusion limit for thicker slabs well. This extension of the gKM method to the vector, polarized case should allow for many other areas of study to make use of this rather simple approximation.

Chapter 5

Reflectance by a half-space

We examine the case of a semi-infinite slab, computing the half-space reflectance from a boundary source incident on the slab. Here, we use the gKM approximation for larger spherical scatterers and non-normal incident angles. We compare the gKM results to those computed via code available for the full vRTE by Mishchenko (`http://www.giss.nasa.gov/staff/mmishchenko/brf/`). Here we find that dependence on higher Fourier modes ($l > 2$) increases (see Appendix A.1).

For this half-space problem, we compute the reflectance [43] defined according to

$$\tilde{\mathbf{I}}(0, -\mu, \varphi) = \frac{\mu_0}{\pi}\mathbf{R}(\mu, \varphi; \mu_0, \varphi_0)\mathbf{I}_0, \tag{5.0.1}$$

where $\mathbf{R}(\mu, \varphi; \mu_0, \varphi_0)$ is the 4×4 half-space reflectance matrix described by Mishchenko, (μ_0, φ_0) is the incident direction, and $\mathbf{I}_0(\mu, \varphi)$ is the four-component Stokes vector of the incident light. We note that we may relate (5.0.1) to the boundary source term in (4.2.9) via $\mathbf{Q}_0 = (2\mu_0\sqrt{2/\pi})\mathbf{I}_0$. To quantify our results, we use the dimensionless ratio of the scatterer's radius to the wavelength of the incident light, $\chi = 2\pi r/\lambda$, where r is the radius and λ the wavelength. Here, r has values from 0.001 to 1.000 and $\lambda = 0.55$. Rayleigh scattering corresponds to a value of $\chi \ll 1$, with moderate to larger values ranging from $\chi \sim 5$ to $\chi \sim 10$, respectively.

We calculate the linear cross-polarization discriminant and the circular polarization ratio, p_l and p_c, respectively defined in (4.4.1a) and (4.4.1b), over this range of χ. We approximate a semi-infinite slab by setting $z_1 = 500$ for the gKM method. In the following, we examine the performance of the gKM method for a range of sphere radii and for angles of incidence. For the latter, we expect a poorer performance from gKM due to larger incident angles having a larger dependence on higher modes for $\varphi - \varphi'$.

5.1 Linear polarization

In this section, we study p_l for a linearly polarized source, incident normally on the slab with $\mathbf{I}_0 = [1, 1, 0, 0]^T$. Since the last two components of $\mathbf{I}_0$ are zero, we find that p_c is identically zero as well for this case. In light of this, we only show results for p_l and note that the gKM method comes within machine precision for $p_c \equiv 0$.

We first examine the gKM approximation as a function of χ. The left plot of Figure 5.1 shows how well the gKM method (dashed line) calculates the cross-polarization

discriminant, p_l, when compared to values computed using (5.0.1) (solid line) [1]. The right plot shows the relative error over the range of χ. We can see that the gKM method shows excellent agreement with the true solution for the entire range, maintaining accuracy near that of the scalar case. This dwindles only slightly at the larger size scatterers, approximately $\chi \geq 8$. It is apparent that the gKM approximation succeeds in capturing the qualitative behavior of the system. This also implies that is capable of modeling essential features to correctly capture the physics involved.

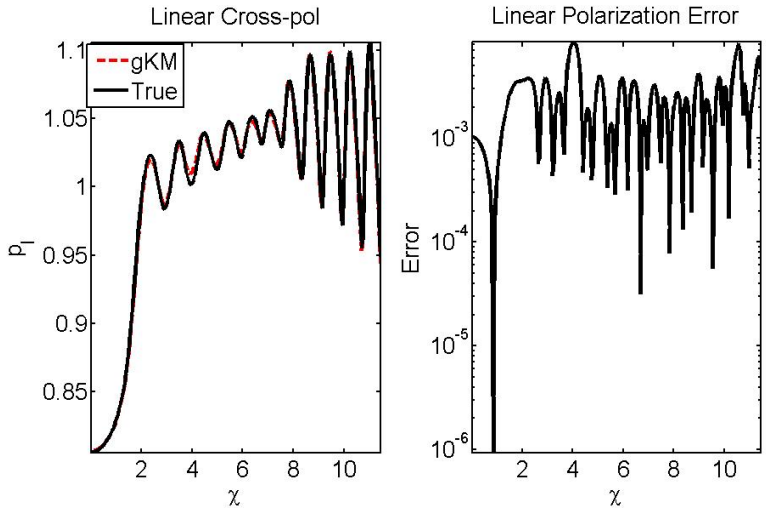

Figure 5.1: Results for p_l computed using gKM (dashed) and Mishchenko et. al. (solid) for a linearly polarized source, incident normally on the slab (left plot). The right plot shows the relative error over the range of χ. Here, $\mathbf{I}_0 = [1, 1, 0, 0]^T$ with $z_1 = 500$.

For oblique angles of incidence, we find, not unexpectedly, that the accuracy of the gKM method decreases as the angle of incidence increases. This is shown in Figure 5.2, where we have plotted the gKM values (dotted line) versus the values computed using (5.0.1) for the linear cross-polarization discriminant, p_l. Here we fix $\chi \sim 0.011$, corresponding to a sphere radius of $r = 0.001$, which is within the domain of Rayleigh scattering. We see that gKM is doing a poor job for values below $\mu_0 \sim 0.8$. This decay is due to increasing dependence of the full vRTE solution on the higher Fourier modes. The gKM approximation is not able to capture these modes.

It is clear that the performance of the gKM method for a linearly polarized source is limited by the direction of the incidence. However, we see that gKM yields remarkable agreement over the range of values for χ used. This is demonstrated by the computation of the linear cross-polarization ratio in Figures 5.1 and 5.2, and is due to the higher modes being negligible for a linearly polarized source. This allows the gKM method to maintain the accuracy demonstrated in the scalar case.

5.2 Circular polarization

For a circularly polarized source, we set $\mathbf{I}_0 = [1, 0, 0, 1]^T$, and consider, once again, normal incidence. For this case, neither p_l nor p_c are identically zero, and we report both values'

[1] computed using Mishchenko, et. al.'s code

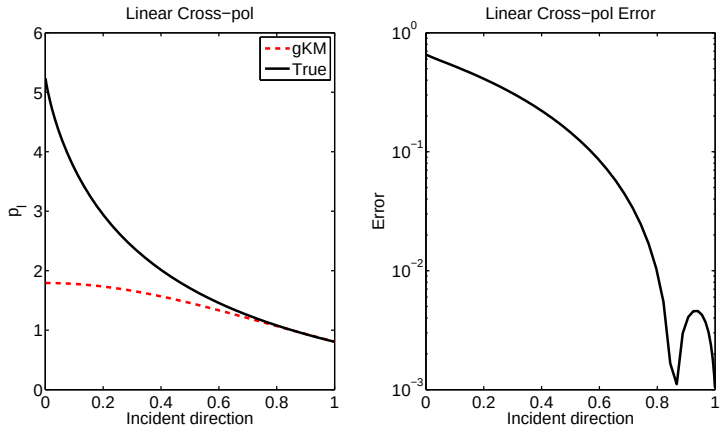

Figure 5.2: Results for p_l computed using gKM (dashed) and Mishchenko et. al. (solid) for a linearly polarized source for the range of incident source directions, μ_0 (left plot). Here, $\mathbf{I}_0 = [1, 1, 0, 0]^T$ with $z_1 = 500$ and $\chi = 0.011$. The right plot shows the relative error.

results. As before, we compare the results of the gKM method to that of Mishchenko via (5.0.1).

We find results similar to the linearly polarized source for near normal angles of incidence, and the performance of the gKM approximation wanes greatly for more oblique incident angles. Figure 5.3 shows this case, plotting p_l over the incident direction, μ_0, for $\chi = 0.011$, in the left plot. Here, we see in the error plot, on the right, that the range of scalar-level accuracy is now much smaller, and hovers closer to values near normally incident ($\mu_0 \approx 0.9$ and higher). Below this, we once more see that gKM cannot capture the behavior of the solution for these more skewed angles of incidence.

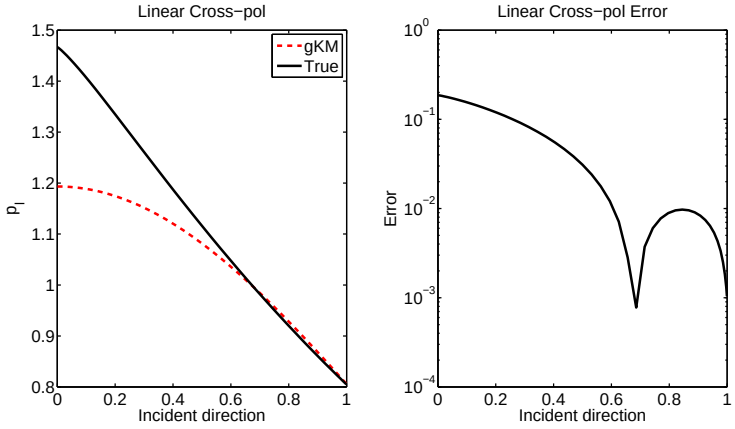

Figure 5.3: Results of p_l computed using gKM (dashed) and the Mishchenko et. al. (solid) for various incident directions (left plot) over the range of incident directions. Here, $\mathbf{I}_0 = [1, 0, 0, 1]^T$ with $z_1 = 500$ and $\chi = 0.011$. The right column shows the relative error for the p_l ratio.

The left column of Figure 5.4 shows the performance of the gKM approximation as a function of χ for the ratios p_l (top row) and p_c (bottom row). The right column displays the relative error for both ratios. Here, we see that the approximation for the linear cross-

polarization ratio is similar to the previous, linearly polarized, case. This is again due to p_l having negligible dependence on the angular quantity $\varphi - \varphi'$, a domain in which gKM has been shown to perform well.

We see that the gKM method is not nearly as accurate for the circular polarization ratio, p_c, decaying in accuracy for values of approximately $\chi \geq 3$. The higher values of χ indicate larger radius spheres, which require the higher Fourier modes for which gKM is unable to completely reconcile. However, despite this, it is clear that it qualitatively captures the behavior of the solution for the whole range of χ. For smaller values of χ, we enjoy the accuracy the gKM approximation has previously demonstrated.

This region of smaller spheres contains a critical value for χ where the value of the circular polarization ratio changes sign. This indicates that the circular component of the light is the same helicity as the incident's. This phenomenon is known as "polarization memory," and is a subject of study in recent decades. We see that the gKM approximation is robust enough to capture complex scattering phenomenon such as this. We intend on utilizing this robustness to study polarization memory in future work.

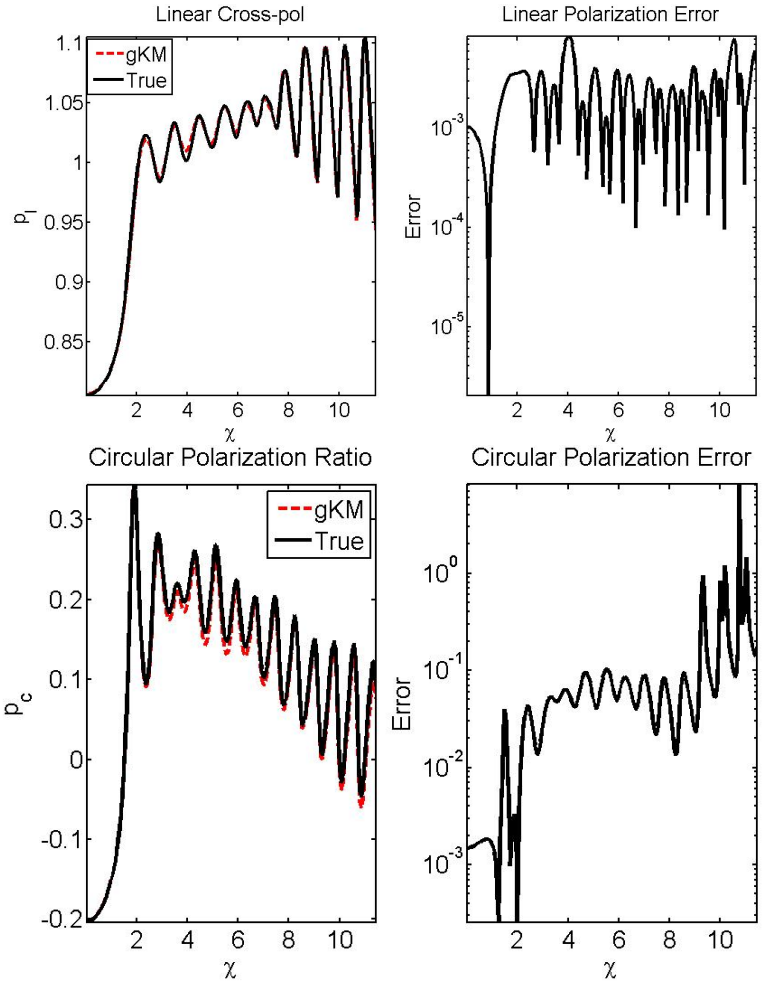

Figure 5.4: Same as Fig. 5.1, but with $\mathbf{I}_0 = [1, 0, 0, 1]^T$ for both p_l and p_c.

5.3 Summary of results

Here we have furthered the domain of applicability for the gKM approximation. We have explored its extension to oblique angles of incidence and larger sized scatterers. To examine the range of validity for these, we have once more computed the ratios p_l and p_c and compared them to results obtained by Mishchenko et. al. for a semi-infinite slab.

For when the angle of incidence is non-normal, we find that the gKM approximation expectedly dwindles in accuracy as the incident angle grows. These larger angles invoke larger dependence on the higher Fourier modes that the gKM approximation neglects, and it is not able to capture the behavior well in these cases. For angles approaching normalcy, we see the expected accuracy of the gKM approximation, providing a good estimate to the actual solution.

The previous chapter explored when scattering was governed by Rayleigh scattering, when the wavelength of the incident light is much larger than the size of the scattering particles. When this ratio, χ, is higher, we see a decrease in the accuracy of the gKM approximation, which once more stems from larger dependence on the higher modes. This, however, does not detract from the ability of gKM to model the qualitative behavior of the system. It is clear that the gKM system is capable of capturing the physics of this complex system, and should provide an excellent method to study such phenomenon as polarization memory.

Chapter 6

Conclusion

In this work, we began by establishing the theoretical foundation for the two-flux, Kubelka-Munk theory. We derived the KM equations by analyzing the DP_1 system of equations via a perturbation on the single scattering albedo, ϖ_0. This yielded two scales, for which the KM system only captures one, and produced the generalized Kubelka-Munk system. This four-flux approximation provided much greater accuracy and a wider domain of applicability. We were then able to accommodate non-isotropic scattering and non-homogeneous source terms, which the original KM theory lacked. Once solid theoretical underpinnings were established, we were then able to compute the long sought KM coefficients and tie them to radiative transfer theory.

From here, we sought to extend gKM to higher dimensions and incorporate a Gaussian beam source. We did this via expansion using spherical harmonics basis functions, once more exploring the application of the gKM approximation in this setting. We demonstrated the range of validity of this model, finding that the interdependence of the spatial terms and the angular quantity, φ, directly affects the accuracy. This is affected further for when the width of the beam is sufficiently small, though all these errors decay as the diffusion limit is approached. Outside this range, the gKM approximation provided good approximation to the outgoing fluxes in a three-dimensional planar slab.

Lastly, we were able to apply gKM theory to the vector, or polarized, case using the vector radiative transfer equation. We did so by creating four sets of coupled 1-D gKM approximations, for each of the Stokes components of the polarized light. This system was solved numerically and the linear cross-polarization discriminant and circular polarization ratio were computed to evaluate the effectiveness of the approximation. We compared these to benchmark results for Rayleigh scattering in a finite one-dimensional slab, showing that gKM provided a good approximation for the case when sphere size is much smaller than the wavelength of the incident light. Next, we considered the semi-infinite slab in order to examine the effects of the size of the spherical scatterers and incident direction. We compared results from the gKM method to results obtained by Mishchenko, establishing that, qualitatively, it captures the behavior of the solution. This includes capturing complex physical phenomenon such as polarization memory, hence further demonstrating an extended flexibility and range of validity for the gKM model.

Over the decades, KM theory has found a home in a breadth of applications, from spectroscopy to remote imaging. Generalized Kubelka-Munk theory broadens this already popular method's ability and range of applicability. The usage of gKM theory will enhance the performance and accuracy of fields that already make use of KM theory, and it has the

potential to now be applied to many fields beyond the original theory's domain of use. This improvement in performance and utility should allow gKM theory to enjoy as much success as, if not more than, its predecessor.

Appendix A

gKM basis and the scattering matrix

A.1 The scattering matrix

The scattering matrix, $\mathbf{Z}(\mu, \mu', \varphi - \varphi')$, following Siewert's convention [44], may be written as

$$\mathbf{Z}(\mu, \mu', \varphi - \varphi') = \sum_{m=0}^{L} \frac{1}{2}(2 - \delta_{0,m}) \left[C^m(\mu, \mu') \cos(m(\varphi - \varphi')) + S^m(\mu, \mu') \sin(m(\varphi - \varphi')) \right]. \tag{A.1.1}$$

Here,

$$C^m(\mu, \mu') = A^m(\mu, \mu') + DA^m(\mu, \mu')D, \qquad S^m(\mu, \mu') = A^m(\mu, \mu')D - DA^m(\mu, \mu'), \tag{A.1.2}$$

$$A^m(\mu, \mu') = \sum_{l=m}^{L} \mathbb{P}_l^m(\mu) \mathbb{B}_l \mathbb{P}_l^m(\mu'), \quad \text{and} \quad D = \text{diag}\{1, 1, -1, -1\} \tag{A.1.3}$$

The matrices, $\mathbb{P}_l^m(\mu)$, have the form

$$\mathbb{P}_l^m(\mu) = \begin{bmatrix} P_l^m(\mu) & 0 & 0 & 0 \\ 0 & R_l^m(\mu) & -T_l^m(\mu) & 0 \\ 0 & -T_l^m(\mu) & R_l^m(\mu) & 0 \\ 0 & 0 & 0 & P_l^m(\mu) \end{bmatrix}, \tag{A.1.4}$$

Now, we adopt the definition of these "normalized auxiliary functions" as $P_l^m(\cos\theta) = d_{0,m}^l(\theta)$,
$R_l^m(\cos\theta) = \frac{1}{2}\left(d_{2,m}^l(\theta) + d_{-2,m}^l(\theta)\right)$, and $T_l^m(\cos\theta) = \frac{1}{2}\left(d_{2,m}^l(\theta) - d_{-2,m}^l(\theta)\right)$, with $d_{km}^l(\theta)$ denoting the Wigner-d functions using the convention of Varshalovich et. al. [45] We also call the set of $\mathbb{B}_l$ the "scattering law," and has the form

$$\mathbb{B}_l = \begin{bmatrix} \beta_l & \gamma_l & 0 & 0 \\ \gamma_l & \alpha_l & 0 & 0 \\ 0 & 0 & \zeta_l & -\epsilon_l \\ 0 & 0 & \epsilon_l & \delta_l \end{bmatrix} \tag{A.1.5}$$

Multiplying the matrix product in (A.1.3), we find that

$$A^m(\mu,\mu') = \sum_{l=m}^{L} \left[\begin{array}{cc} P_l^m(\mu)P_l^m(\mu')\beta_l & P_l^m(\mu)R_l^m(\mu')\gamma_l \\ R_l^m(\mu)P_l^m(\mu')\gamma_l & R_l^m(\mu)R_l^m(\mu')\alpha_l + T_l^m(\mu)T_l^m(\mu')\zeta_l \\ -T_l^m(\mu)P_l^m(\mu')\gamma_l & -T_l^m(\mu)R_l^m(\mu')\alpha_l - R_l^m(\mu)T_l^m(\mu')\zeta_l \\ 0 & -P_l^m(\mu)T_l^m(\mu')\epsilon_l \end{array} \right.$$
$$\left. \begin{array}{cc} -P_l^m(\mu)T_l^m(\mu')\gamma_l & 0 \\ -R_l^m(\mu)T_l^m(\mu')\alpha_l - T_l^m(\mu)R_l^m(\mu')\zeta_l & T_l^m(\mu)P_l^m(\mu')\epsilon_l \\ T_l^m(\mu)T_l^m(\mu')\alpha_l + R_l^m(\mu)R_l^m(\mu')\zeta_l & -R_l^m(\mu)P_l^m(\mu')\epsilon_l \\ P_l^m(\mu)R_l^m(\mu')\epsilon_l & P_l^m(\mu)P_l^m(\mu')\delta_l \end{array} \right]. \tag{A.1.6}$$

We will begin by examining the integral portion of the transport equation, i.e.

$$\frac{1}{4\pi}\int_{-1}^{1}\int_{0}^{2\pi} \mathbf{Z}(\mu,\mu',\varphi-\varphi')\mathbf{I}(\mu',\varphi',z)\ d\mu' d\varphi'. \tag{A.1.7}$$

Furthermore, since projection onto the gKM basis functions (3.2.9) is also done, we are interested in the quantity

$$\frac{1}{4\pi}\int_{0}^{1}\int_{0}^{2\pi} \Phi_j(\mu,\varphi)\int_{0}^{1}\int_{0}^{2\pi} \mathbf{Z}(\mu,\mu',\varphi-\varphi')\Phi_k(\mu',\varphi')\ d\mu' d\varphi'\ d\mu d\varphi. \tag{A.1.8}$$

A.2 Integrating over $\varphi - \varphi'$

According to equation (A.1.1), we write (A.1.8) as

$$\frac{1}{4\pi}\sum_{m=0}^{L}\frac{1}{2}(2-\delta_{0,m})\int_{0}^{2\pi}\Phi_j(\mu,\varphi) \times \int_{0}^{2\pi}\left[C^m(\mu,\mu')\cos(m(\varphi-\varphi')) + S^m(\mu,\mu')\sin(m(\varphi-\varphi'))\right]\Phi_k(\mu',\varphi')\ d\varphi'\ d\varphi \tag{A.2.1}$$

Expressing this in matrix form, we get

$$\frac{1}{8\pi}\sum_{m=0}^{L}(2-\delta_{0,m})\int_{0}^{2\pi}\int_{0}^{2\pi}\left[C^m(\mu,\mu')\cos(m(\varphi-\varphi')) + S^m(\mu,\mu')\sin(m(\varphi-\varphi'))\right] \otimes \mathbf{\Phi}(\mu,\mu',\varphi,\varphi')\ d\varphi'\ d\varphi, \tag{A.2.2}$$

where we have written the matrix

$$\begin{aligned}\mathbf{\Phi}(\mu,\mu',\varphi,\varphi') &= [\Phi_1(\mu,\varphi),\Phi_2(\mu,\varphi),\Phi_3(\mu,\varphi),\Phi_4(\mu,\varphi)]^T\ [\Phi_1(\mu,\varphi),\Phi_2(\mu,\varphi),\Phi_3(\mu,\varphi),\Phi_4(\mu,\varphi)] \\ &= [\tilde{\Phi}_1(\mu),\tilde{\Phi}_2(\mu),\tilde{\Phi}_3(\mu)\cos\varphi,\tilde{\Phi}_4(\mu)\sin\varphi]^T\ [\tilde{\Phi}_1(\mu),\tilde{\Phi}_2(\mu),\tilde{\Phi}_3(\mu)\cos\varphi,\tilde{\Phi}_4(\mu)\sin\varphi],\end{aligned} \tag{A.2.3}$$

and $\otimes$ is the Kronecker product. Observing that for values of $m > 1$, the set of $\{\Phi_j\}$ is orthogonal to $\cos(m(\varphi-\varphi'))$ and $\sin(m(\varphi-\varphi'))$, we need only consider the values $m = 0$

and 1. For $m = 0$, we find that (A.2.2) yields

$$\frac{1}{8\pi}\int_0^{2\pi}\int_0^{2\pi} C^0(\mu,\mu')\otimes\mathbf{\Phi}(\mu,\mu',\varphi,\varphi')\;d\varphi'\;d\varphi. \tag{A.2.4}$$

Completing the integrations, we find (A.2.4) becomes

$$\frac{\pi}{2}C^0(\mu,\mu')\otimes\begin{bmatrix}\tilde{\Phi}_1(\mu)\tilde{\Phi}_1(\mu') & \tilde{\Phi}_1(\mu)\tilde{\Phi}_2(\mu') & 0 & 0\\ \tilde{\Phi}_2(\mu)\tilde{\Phi}_1(\mu') & \tilde{\Phi}_2(\mu)\tilde{\Phi}_2(\mu') & 0 & 0\\ 0 & 0 & 0 & 0\\ 0 & 0 & 0 & 0\end{bmatrix} = \frac{\pi}{2}C^0(\mu,\mu')\otimes\Gamma_1(\mu,\mu') \tag{A.2.5}$$

Meanwhile, for $m = 1$, (A.2.2) gives

$$\frac{1}{4\pi}\int_0^{2\pi}\int_0^{2\pi}\left[C^1(\mu,\mu')\cos(\varphi-\varphi') + S^1(\mu,\mu')\sin(\varphi-\varphi')\right]\otimes\mathbf{\Phi}(\mu,\mu',\varphi,\varphi')\;d\varphi'\;d\varphi. \tag{A.2.6}$$

Performing the integrations and writing in matrix form, (A.2.6) becomes

$$\begin{aligned}\frac{\pi}{4}C^1(\mu,\mu')\otimes&\begin{bmatrix}0&0&0&0\\0&0&0&0\\0&0&\tilde{\Phi}_3(\mu)\tilde{\Phi}_3(\mu')&0\\0&0&0&\tilde{\Phi}_4(\mu)\tilde{\Phi}_4(\mu')\end{bmatrix}\\ +\frac{\pi}{4}S^1(\mu,\mu')\otimes&\begin{bmatrix}0&0&0&0\\0&0&0&0\\0&0&0&-\tilde{\Phi}_3(\mu)\tilde{\Phi}_4(\mu')\\0&0&\tilde{\Phi}_4(\mu)\tilde{\Phi}_3(\mu')&0\end{bmatrix}\\ &= \frac{\pi}{4}\left[C^1(\mu,\mu')\otimes\Gamma_2(\mu,\mu') + S^1(\mu,\mu')\otimes\Gamma_3(\mu,\mu')\right]\end{aligned} \tag{A.2.7}$$

Hence, (A.1.8) now may be written as

$$\frac{\pi}{4}\int_0^1\int_0^1\left[2C^0(\mu,\mu')\otimes\Gamma_1(\mu,\mu') + C^1(\mu,\mu')\otimes\Gamma_2(\mu,\mu') + S^1(\mu,\mu')\otimes\Gamma_3(\mu,\mu')\right]\;d\mu' d\mu. \tag{A.2.8}$$

Equation (A.2.8) shows that only certain projections need be made in μ and μ', and equations (A.1.2) and (A.1.3) require these computed onto the components of $A^{0,1}(\mu,\mu')$ only. Hence, we consider the quantities

$$\int_0^1\int_0^1\tilde{\Phi}_j(\mu)\tilde{\Phi}_k(\mu')A^0(\mu,\mu')\;d\mu' d\mu, \quad j,k = 1,2 \tag{A.2.9a}$$

$$\int_0^1\int_0^1\tilde{\Phi}_j(\mu)\tilde{\Phi}_k(\mu')A^1(\mu,\mu')\;d\mu' d\mu, \quad j,k = 3,4 \tag{A.2.9b}$$

This in turn allows us to further consider only the quantities

$$\int_0^1 \int_0^1 \tilde{\Phi}_j(\mu)\tilde{\Phi}_k(\mu')P_l^m(\mu)P_l^m(\mu')\ d\mu' d\mu, \tag{A.2.10a}$$

$$\int_0^1 \int_0^1 \tilde{\Phi}_j(\mu)\tilde{\Phi}_k(\mu')P_l^m(\mu)R_l^m(\mu')\ d\mu' d\mu, \tag{A.2.10b}$$

$$\int_0^1 \int_0^1 \tilde{\Phi}_j(\mu)\tilde{\Phi}_k(\mu')P_l^m(\mu)T_l^m(\mu')\ d\mu' d\mu, \tag{A.2.10c}$$

$$\int_0^1 \int_0^1 \tilde{\Phi}_j(\mu)\tilde{\Phi}_k(\mu')R_l^m(\mu)R_l^m(\mu')\ d\mu' d\mu, \tag{A.2.10d}$$

$$\int_0^1 \int_0^1 \tilde{\Phi}_j(\mu)\tilde{\Phi}_k(\mu')R_l^m(\mu)T_l^m(\mu')\ d\mu' d\mu, \tag{A.2.10e}$$

$$\int_0^1 \int_0^1 \tilde{\Phi}_j(\mu)\tilde{\Phi}_k(\mu')T_l^m(\mu)T_l^m(\mu')\ d\mu' d\mu. \tag{A.2.10f}$$

In light of equation (A.2.8), we only need evaluate these for $j,k = 1,2$ when $m = 0$ and for $j,k = 3,4$ when $m = 1$. These direct computations of the scattering matrix projections should allow for less overhead and more efficient and accurate computations.

A.3 Normalized auxiliary functions

We need only examine these normalized auxiliary functions for $m = 0, 1$. Hence for when $m = 0$, we find that $P_l^0(\mu) = P_l(\mu)$, $R_l^0(\mu) = P_l^2(\mu)$, and $T_l^0(\mu) = 0$. For $m = 1$, we're forced to turn to the recurrence relations

$$l\sqrt{(l+1)^2-4}\sqrt{(l+1)^2-1}R_{l+1}^1(x) = l(l+1)(2l+1)xR_l^1(x) - (l+1)\sqrt{l^2-4}\sqrt{l^2-1}R_{l-1}^1(x) - 2(2l+1)T_l^1(x), \tag{A.3.1a}$$

$$l\sqrt{(l+1)^2-4}\sqrt{(l+1)^2-1}T_{l+1}^1(x) = l(l+1)(2l+1)xT_l^1(x) - (l+1)\sqrt{l^2-4}\sqrt{l^2-1}T_{l-1}^1(x) - 2(2l+1)R_l^1(x) \tag{A.3.1b}$$

for $R_l^1(x)$ and $T_l^1(x)$, while $P_l^2(x)$ is simply the normalized associated Legendre function. We calculate the basis for the recursion as

$$R_2^1(x) = -\frac{1}{2}x\sqrt{1-x^2}, \tag{A.3.2a}$$

$$R_3^1(x) = \frac{1}{4}\sqrt{\frac{5}{2}}\sqrt{1-x^2}(1-3x^2), \tag{A.3.2b}$$

$$T_2^1(x) = -\frac{1}{2}\sqrt{1-x^2}, \tag{A.3.2c}$$

$$T_3^1(x) = -\frac{1}{2}\sqrt{\frac{5}{2}}x\sqrt{1-x^2}. \tag{A.3.2d}$$

Note that $R_l^1(x) = T_l^1(x) = 0$ for $l < 2$.

A.4 Rayleigh scattering

When the wavelength of the incident light is much larger than the size of the scattering paricles within the medium, known as Rayleigh scattering, we find that the scattering matrix requires only modes 0,1, and 2 in its Fourier expansion over $\varphi - \varphi'$. Hence, we need only consider $0 \leq l \leq 2$ in computing (A.1.6) and, hence, equation (A.2.10). The scattering law associated with it is $\alpha_2 = 6(1-\rho)/(2+\rho)$, $\beta_0 = 1$, $\beta_2 = (1-\rho)/(2+\rho)$, $\gamma_2 = -\sqrt{6}(1-\rho)/(2+\rho)$, and $\delta_1 = 3(1-2\rho)/(2+\rho)$. Here, ρ is the depolarization ratio [46]. The remaining entries of $\mathbb{B}_l$ are 0. Using these values, we may rewrite (A.1.6) as

$$A^m(\mu,\mu') = \begin{bmatrix} P_0^m(\mu)P_0^m(\mu')\beta_0 + P_2^m(\mu)P_2^m(\mu')\beta_2 & P_2^m(\mu)R_2^m(\mu')\gamma_2 & -P_2^m(\mu)T_2^m(\mu')\gamma_2 & 0 \\ R_2^m(\mu)P_2^m(\mu')\gamma_2 & R_2^m(\mu)R_2^m(\mu')\alpha_2 & -R_2^m(\mu)T_2^m(\mu')\alpha_2 & 0 \\ -T_2^m(\mu)P_2^m(\mu')\gamma_2 & -T_2^m(\mu)R_2^m(\mu')\alpha_2 & T_2^m(\mu)T_2^m(\mu')\alpha_2 & 0 \\ 0 & 0 & 0 & P_1^m(\mu)P_1^m(\mu')\delta_1 \end{bmatrix} \tag{A.4.1}$$

For the values of $m = 0, 1$, we find

$$A^0(\mu,\mu') = \begin{bmatrix} P_0(\mu)P_0(\mu')\beta_0 + P_2(\mu)P_2(\mu')\beta_2 & P_2(\mu)P_2^2(\mu')\gamma_2 & 0 & 0 \\ P_2^2(\mu)P_2(\mu')\gamma_2 & P_2^2(\mu)P_2^2(\mu')\alpha_2 & 0 & 0 \\ 0 & 0 & 0 & 0 \\ 0 & 0 & 0 & P_1(\mu)P_1(\mu')\delta_1 \end{bmatrix} \tag{A.4.2}$$

and

$$A^1(\mu,\mu') = \begin{bmatrix} P_2^1(\mu)P_2^1(\mu')\beta_2 & P_2^1(\mu)R_2^1(\mu')\gamma_2 & -P_2^1(\mu)T_2^1(\mu')\gamma_2 & 0 \\ R_2^1(\mu)P_2^1(\mu')\gamma_2 & R_2^1(\mu)R_2^1(\mu')\alpha_2 & -R_2^1(\mu)T_2^1(\mu')\alpha_2 & 0 \\ -T_2^1(\mu)P_2^1(\mu')\gamma_2 & -T_2^1(\mu)R_2^1(\mu')\alpha_2 & T_2^1(\mu)T_2^1(\mu')\alpha_2 & 0 \\ 0 & 0 & 0 & P_1^1(\mu)P_1^1(\mu')\delta_1 \end{bmatrix} \tag{A.4.3}$$

Using the definitions in (A.1.2) and (A.1.3), we can use (A.4.2) and (A.4.3) to write

$$C^0(\mu,\mu') = A^0(\mu,\mu') + DA^0(\mu,\mu')D = 2A^0(\mu,\mu'), \tag{A.4.4a}$$

$$C^1(\mu,\mu') = 2\begin{bmatrix} P_2^1(\mu)P_2^1(\mu')\beta_2 & P_2^1(\mu)R_2^1(\mu')\gamma_2 & 0 & 0 \\ R_2^1(\mu)P_2^1(\mu')\gamma_2 & R_2^1(\mu)R_2^1(\mu')\alpha_2 & 0 & 0 \\ 0 & 0 & T_2^1(\mu)T_2^1(\mu')\alpha_2 & 0 \\ 0 & 0 & 0 & P_1^1(\mu)P_1^1(\mu')\delta_1 \end{bmatrix} = 2A_C^1(\mu,\mu'), \tag{A.4.4b}$$

$$S^1(\mu,\mu') = 2\begin{bmatrix} 0 & 0 & P_2^1(\mu)T_2^1(\mu')\gamma_2 & 0 \\ 0 & 0 & R_2^1(\mu)T_2^1(\mu')\alpha_2 & 0 \\ -T_2^1(\mu)P_2^1(\mu')\gamma_2 & -T_2^1(\mu)R_2^1(\mu')\alpha_2 & 0 & 0 \\ 0 & 0 & 0 & 0 \end{bmatrix} = 2A_S^1(\mu,\mu'), \tag{A.4.4c}$$

Now, equation (A.2.8) becomes

$$\frac{\pi}{2}\int_0^1\int_0^1 \left[2A^0(\mu,\mu')\otimes\Gamma_1(\mu,\mu')+A_C^1(\mu,\mu')\otimes\Gamma_2(\mu,\mu')+A_S^1(\mu,\mu')\otimes\Gamma_3(\mu,\mu')\right]\ d\mu' d\mu \tag{A.4.5}$$

Hence, equation (A.1.8) for Rayleigh scattering is

$$\begin{aligned}&\frac{1}{4\pi}\int_0^1\int_0^{2\pi}\Phi_j(\mu,\varphi)\int_0^1\int_0^{2\pi}\mathbb{P}(\mu,\mu',\varphi-\varphi')\Phi_k(\mu',\varphi')\ d\mu' d\varphi'\ d\mu d\varphi\\ &\quad=\frac{\pi}{2}\int_0^1\int_0^1 \left[2A^0(\mu,\mu')\otimes\Gamma_1(\mu,\mu')+A_C^1(\mu,\mu')\otimes\Gamma_2(\mu,\mu')+A_S^1(\mu,\mu')\otimes\Gamma_3(\mu,\mu')\right]\ d\mu' d\mu\end{aligned} \tag{A.4.6}$$

Bibliography

[1] S. Chandrasekhar, *Radiative Transfer* (Dover, 1960).

[2] A. Ishimaru, *Wave Propagation and Scattering in Random Media* (IEEE, 1996).

[3] G. E. Thomas and K. Stamnes, *Radiative Transfer in the Atmosphere and Ocean* (Cambridge University Press, 1999)

[4] L. V. Wang and H.-I. Wu, *Biomedical Optics* (Wiley, 2007).

[5] P. Kubelka and F. Munk, "Ein beitrag zur optik der farbanstriche," Z. Tech. Phys. **12**, 593-601 (1931).

[6] P. Kubelka, "New contributions to the optics of intensely light-scattering materials part I," J. Opt. Soc. Am. A **38**, 448-457 (1948).

[7] B. Davison, *Neutron Transport Theory* (Oxford University Press, 1958).

[8] K. M. Case, and P. F. Zweifel, *Linear Transport Theory* (Addison-Wesley, 1967).

[9] E. E. Lewis, and W. F. Miller, *Computational Methods of Neutron Transport* (American Nuclear Society, 1993).

[10] R. Aronson, "P_N vs. double-P_N approximations for highly anisotropic scattering," Transp. Theory Stat. Phys. **15**, 829-840 (1986).

[11] B. J. Brinkworth, "Interpretations of the Kubelka-Munk coefficients in reflection theory," Appl. Opt. **11**, 1434-1435 (1972).

[12] L. F. Gate, "Comparison of the photon diffusion model and Kubelka-Munk equation with exact solution of the radiative transport equation," Appl. Opt. **13**, 236-238 (1974).

[13] W. E. Vargas and G. A. Niklasson, "Applicability conditions of the Kubelka-Munk theory," Appl. Opt. **36**, 5580-5586 (1997).

[14] L. Yang and B. Kruse, "Revised Kubelka-Munk theory. I. Theory and application," **21**, 1933-1941 (2004).

[15] L. Yang, B. Kruse, and S. J. Miklavcic, "Revised Kubelka-Munk theory. II. Unified framework for homogeneous and inhomogeneous optical media," J. Opt. Soc. Am. A **21**, 1942-1952 (2004).

[16] L. Yang, and S. J. Miklavcic, "Revised Kubelka-Munk theory. III. A general theory of light propagation in scattering and absorptive media," J. Opt. Soc. Am. A **22**, 1866-1873 (2005).

[17] P. Edström, "Examination of the revised Kubelka-Munk theory: considerations of modeling strategies," J. Opt. Soc. Am. A **24**, 548-556 (2007).

[18] S. N. Thennadil, "Relationships between the Kubelka-Munk scattering and radiative transfer coefficients," J. Opt. Soc. Am. A **25**, 1480-1485 (2008).

[19] M. Neuman, and P. Edström, "Anisotropic reflectance from turbid media. I. Theory," J. Opt. Soc. Am. A **27**, 1032-1039 (2010).

[20] M. L. Myrick, M. N. Simcock, M. Baranowski, H. Brooke, S. L. Morgan, and J. N. McCutcheon, "The Kubelka-Munk diffuse reflectance formula revisited," Appl. Spectros. Rev. **46**, 140-165 (2011).

[21] M. Hébert and J. Machizaud, "Spectral reflectance and transmittance of stacks of nonscattering films printed with halftone colors," J. Opt. Soc. Am. A **29**, 2498–2508 (2012).

[22] S. Mazauric, M. Hébert, L. Simonot, and T. Fournel, "Two-flux transfer matrix model for predicting the reflectance and transmittance of duplex halftone prints," J. Opt. Soc. Am. A **31**, 2775–2788 (2014).

[23] L. Yang, "Characterization of inks and ink application for ink-jet printing: model and simulation," J. Opt. Soc. Am. A **20**, 1149–1154 (2003).

[24] L. Le Hors, et. al. "A phenomenological model of paints for multispectral polarimetric imaging," Proc. of SPIE **4370** (2001).

[25] A. Mosca Conte, et. al. "Visual degredation in Leonardo da Vinci's iconic self-portrait: A nanoscale study" Appl. Phys. Letters **104**, 224101 (2014).

[26] D. Yudovsky and A. J. Durkin, "Hybrid diffusion and two-flux approximation for multilayered tissue light propagation modeling," Appl. Opt. **50**, 4237–4245 (2011).

[27] M. Seyfried and L. Fukshansky, "Light gradients in plant tissue," Appl. Opt. **22**, 1402–1408 (1983).

[28] M. Seyfried and E. Schäffer, "Changes in the optical properties of cotyledons of *Cucurbita pepo* during the first seven days of their development," Plant Cell Environ. **6**, 633–640 (1983).

[29] M. P. Mengüç and R. K. Iyer, "Modeling of radiative transport using multiple spherical harmonics approximations," J. Quant. Spectrosc. Radiat. Transfer **39**, 445–461 (1988).

[30] J. Nobbs, "Kubelka-Munk Theory and the Prediction of Reflectance," Rev. Prog. Coloration **15**, 66-75 (1985).

[31] R. Molenaar, J. ten Bosch, and J. Zijp, "Determination of Kubelka-Munk Scattering and Absorption Coefficients by Diffuse Illumination," Appl. Opt. **38**, 2068-2077 (1999).

[32] W. M. Star, J. P. A. Marijnissen, and M. J. C. Van Gemert, "Light dosimetry in optical phantoms and in tissues: I. Multiple flux and transport theory," Phys. Med. Biol. **33**, 437-454 (1988).

[33] C. Sandoval and A. D. Kim, "Deriving Kubelka-Munk theory from radiative transport," J. Opt. Soc. Am. A **31**, 628-636 (2014).

[34] A. B. Davis and A. Marshak, "Solar radiation transport in the cloudy atmosphere: a 3D perspective on observations and climate impacts," Rep. Prog. Phys. **73**, 026801 (2010).

[35] J. T. O. Kirk, *Light and Photosynthesis in Aquatic Ecosystems* (Cambridge University Press, New York, 1994).

[36] D. Schiff and S. Ziering, "Many-fold moment method," Nucl. Sci. Eng. **7**, 172–183 (1960).

[37] M. N. Özişik, J. Menning, and W. H. Halg, J. Quant. Spectrosc. Radiat. Transfer **15**, 1101-1106 (1975).

[38] A. Ishimaru, Y. Kuga, R. L.-T. Cheung, and K. Shimizu, "Scattering and diffusion of a beam wave in randomly distributed scatterers," J. Opt. Soc. Am. A **73**, 131-136 (1983).

[39] H.-W. Chang and A. Ishimaru, "Beam wave propagation and scattering in random media based on the radiative transfer theory," J. Wave-Material Interaction **2**, 41-69 (1987).

[40] A. D. Kim and M. Moscoso, "Beam propagation in sharply peaked forward scattering media," J. Opt. Soc. Am. A **21**, 797-803 (2004).

[41] C. K. Hayakawa, J. Spanier, and V. Venugopalan, "Comparative analysis of discrete and continuous absorption weighting estimators used in Monte Carlo simulations of radiative transport in turbid media," J. Opt. Soc. Am. A **31**, 301–311 (2014).

[42] A.D. Kim, M. Moscoso, "Diffusion of polarized light," Multiscale Model. Simul. **9** No. 4, 1624-1645 (2011).

[43] M. Mishchenko, "Polarized bidirectional reflectance of optically thick sparse particulate layers: An efficient numerically exact radiative-transfer solution," J. Quant. Spectrosc. Radiat. Transfer, **156** 97–108 (2015).

[44] C. E. Siewert, "A discrete-ordinate solution for the radiative-transfer models that include polarization effects," J. Quant. Spectrosc. Radiat. Transfer, **64** 227–254 (2000).

[45] A. D. Varshalovich, A. N. Moskalev, and V. K. Khersonskii, "Quantum theory of angular momentum," World Scientific (1988).

[46] J. W. Hovenier, C. V. M. van der Mee, and Helmut Domke, "Transfer of polarized light in planetary atmospheres," Kluwer Academic Publishers, Dordrecht, The Netherlands (2004).